UNIVERSITY OF CALIFORNIA
RIVERSIDE

Synthesis-Structure Relationships of Nanostructured Materials

A Dissertation submitted in partial satisfaction
of the requirements for the degree of

Doctor of Philosophy

in

Materials Science and Engineering

by

Luz Cruz

June 2022

Dissertation Committee:
Prof. Kandis Leslie Abdul-Aziz, Chairperson
Prof. Alex Greaney
Prof. Ashok Mulchandani

The Dissertation of Luz Cruz is approved:

_____

_____

_____

Committee Chairperson

University of California, Riverside

Acknowledgments

First, I would like to gratefully thank my advisor, Kandis Leslie Abdul-Aziz, for providing me with the opportunity to to work in her lab and be a part of her research group. Thank you for your support, guidance, and valuable mentorship throughout this journey I truly appreciate everything she has done for me.

I would like to thank my committee members Professor Ashok Mulchandani, and Professor Greaney for their kind suggestions and support.

Next, I would like to thank all my current and past colleagues specifically Dr. Jesus Rivera, Steven Herrera, Zaira Alibay, Morgan Dundon, Dr. Nick Yaraghi, Dr. Ramya Mohan, Rouheng Zhao, Dr. Thomas Dugger, Joshua Edwards, Dr. Wei Huang, Dr. Wen Yang, Dr. Qiurong Shi, Dr. Parawee Pumwongpitak, Taifeng Wang, Somchate Wasanwisut, Soham Shah, Tu Nguyen, Mark Gale, Seongbin Jo, Barnali Sutradhar, Fernanda Alonso, and Andrew Sanchez. All of you have truly made this a wonderful experience and I appreciate your support and friendship over the years.

Lastly, I want to thank my family and childhood friends for always supporting me in all my endeavors. Thank you, Mom, Danny, Mateo Amaya, Felix Hernandez, Christopher Miranda, Danny Lam, and Victor Cabrera. I could not have accomplished my work without their unconditional love, encouragement, and support. It means the world to me.

ABSTRACT OF THE DISSERTATION

Synthesis-Structure Relationships of Nanostructured Materials

by

Luz Cruz

Doctor of Philosophy, Graduate Program in Materials Science and Engineering
University of California, Riverside, June 2022
Prof. Kandis Leslie Abdul-Aziz, Chairperson

There is an increasing demand for engineered materials that are low cost and efficient for a wide range of energy applications. In this study we look at three different nanostructured systems 1) Ni metal embedded in a 1D carbon nanofiber matrix 2) TiO_2 nanoparticles embedded in a 1D carbon nanofiber matrix and 3) Ni-Fe bimetallic nanostructures on a perovskite oxide support. We describe a two-step electrospinning annealing method to produce 1D carbon nanofibrous networks embedded with catalytic metal (Ni) or metal oxide (TiO_2) nanoparticles. Using a combination of microscopic and spectroscopic methods, we aim to understand the polymer effects on crystal growth and phase transformation of these metal/metal oxide nanostructures. Particle growth mechanisms of Ni nanoparticles and concurrent graphitization will be identified. Investigation of the crystal growth and phase transformation of these nanostructures within a polymer matrix will provide insight to the controlled synthesis and assembly of the nanoparticle constituents and their effect on performance. Exsolution studies of Ni and Fe metal nanoparticles in a perovskite oxide support will be studied and particle growth at

elevated temperatures will also be analyzed. These design guidelines can aid in their application of multifunctional nanocomposites that are efficiently produced for energy and environmental applications such as dry methane reforming and water purification.

Table of Contents

List of Figures

Chapter 1 Introduction

Materials have played an important role in advancing civilization throughout history [1] . Early human society circa 10,000 B.C. primarily lived as hunters and gatherers obtaining food using tools made from stone and wood. They used materials readily accessible to them such as, ivory from elephants, wood and natural rock for housing, and stone used as tools for hunting. By recognizing that these materials could be manipulated, humans were able to make new materials with improved properties. They developed heat treatment and mixing techniques that changed the material's physical properties and made them into higher quality tools and weapons. For example, ancient Sumerians produced the first alloy in history, bronze, which is composed of a mixture of copper and tin. They developed casting, a processing technique to heat treat, melt, and pour metal mixture into molds to create complex structures with improved mechanical properties. This revolutionary processing technique was adopted throughout Europe and still used today. The advancements of similar complex manufacturing processes lead Assyrians to become the first military power in history. They were the first to use iron in their weaponry and became the most technologically advanced army of their time. The development in materials and material processing techniques established societies and modernized them.

Many materials used today were only developed in the last 100 years due to technical advances and the increased understanding of structural-property relationships. As a result, we have seen an influx of new metal alloys, plastics, glasses, and fibers summarized in Figure 1.1. with over 160,000 materials available today [1], [2]. Spurring these advancements, the growth of technology occurred during the industrial revolution in

the 18th century where society shifted to machine manufacturing and technological advancements such as the steam engine, automobiles, and radio transmission. This led to the usage of lighter metals, rare earths, new alloys, and synthetic materials like plastics and composites.

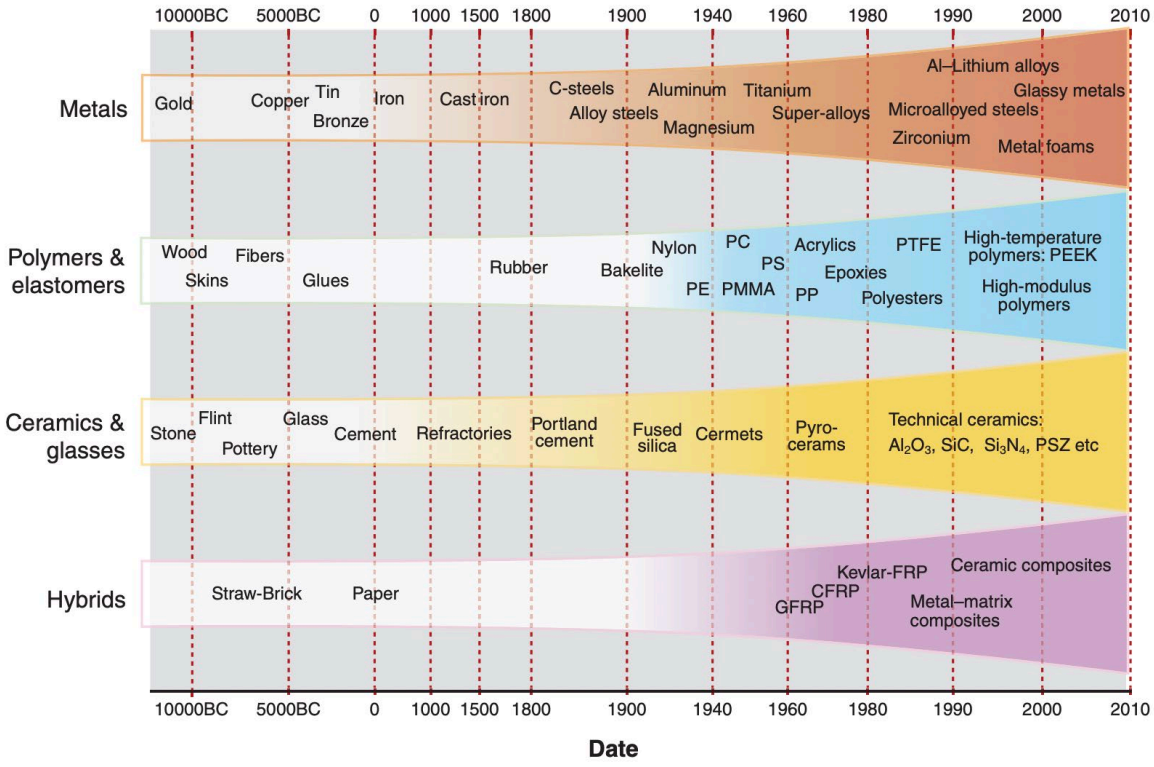

Figure 1.1 Materials development throughout history [2].

In the late 20th century as components grew smaller, the dominant material became silicon as the digital revolution emerged. This led to the development of electronic components such as the metal oxide semiconductor (MOS) transistor which is used in computer memory chips. A transistor is an electronically controlled switch that can turn on and off by applying or removing voltage from the gate (Figure 1.2), representing the ones

and zeroes used for computation. The voltage applied to the gate of the transistor determines its electrical current. This ability to manipulate and control current made it useful for a wide range of applications. The MOS transistor was the first transistor that could be miniaturized, and mass produced.

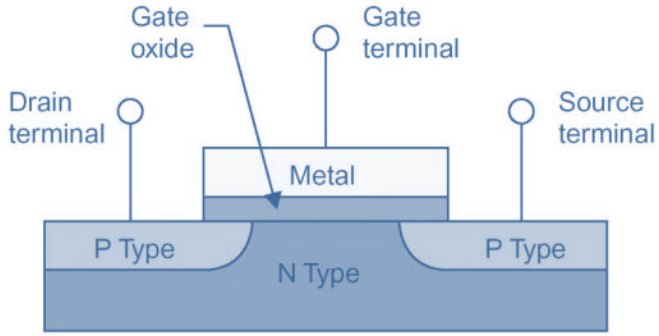

Figure 1.2 Basic MOSFET transistor structure

Transistors transformed the electronics world as it replaced vacuum tubes in electronic equipment such as televisions, radios, and computers. By replacing vacuum tubes with transistors, electronic systems were able to be made smaller, cheaper, and more durable. MOS transistors became primary elements of computer processors, memory chips and image sensors and other types of Integrated Circuits (IC) (a series of electronic components fabricated as a single unit typically on a silicon wafer). By understanding the synthesis-structure-property relationships of this pivotal component engineers were able to make devices smaller, more efficiently and cheaper.

An analogous invention that changed the way electronic components were made was the fabrication method of transistors, photolithography. Invented in the 1960's photolithography is a method in which uses a silicon wafer that is heated in a furnace to make a metal oxide film, a polymer coating known as a photoresist is applied over this

silicon dioxide film. By shining different frequencies of light, one can strip off areas one choses making a designed pattern. The etched patterns can then be deposited with metals and other electrical material components. This process is summarized in Figure 1.3. The photolithography process is what allowed transistors to consistently be made smaller and smaller up to the nanometer scale. This accessibility and fast improvement of these devices allowed people to purchase them with a higher frequency. Today people buy a new phone every 1-2 years wanting to upgrade to the newest fastest model.

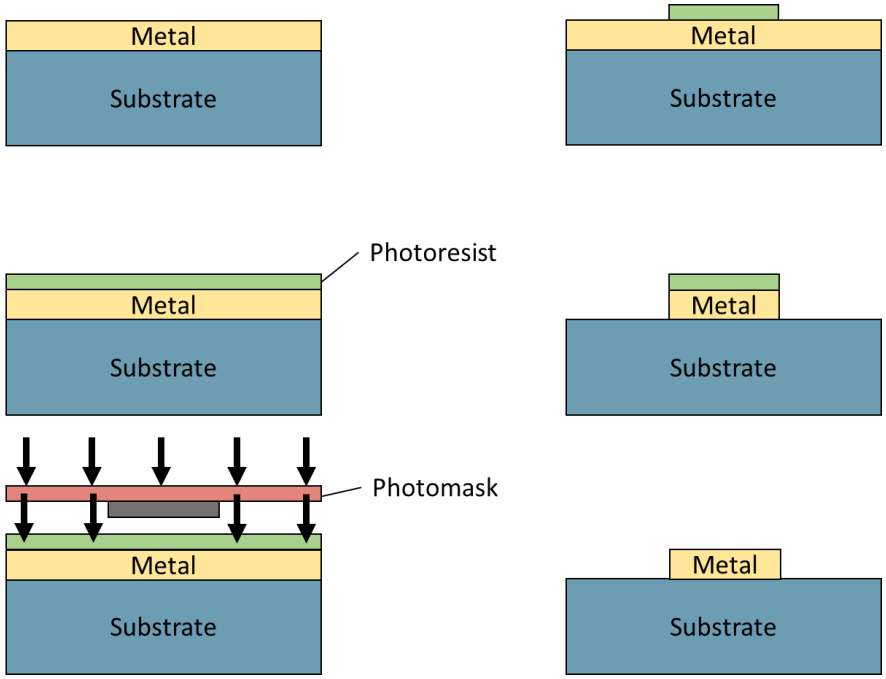

Figure 1.3 Schematic of photolithography process

This surge in technological advancements was not only seen in electronic devices, but a boom in the manufacturing of consumer products like automobiles, commercial aircraft, and modernizing of the agriculture industry. In the year 1900, 1 out of every 10,000 people owned a car [3]. In 2019, there were 1.4 billion vehicles in use throughout the world.

Technological advancements have also been seen in the medical field where medicines, vaccines, and better medical equipment has decreased the overall mortality rate of the global population. This technological boom has led to a large increase in population which has caused the acceleration of the depletion of natural resources. Currently, there are 7 billion people on the planet, which has increased consumption and demand of natural resources such as freshwater, oil, coal, and rare earth metals. According to the EPA, human activity is responsible for the increase in greenhouse gas emissions from the burning of fossil fuels for electricity, heat, and transportation [4]. Because of this, there is a need for the development of a new generation of materials with increased performance and efficiency while considering the environmental impact on processing and production in all sectors of society.

A promising solution to this problem is a new class of materials; nanomaterials which have improved properties and can potentially be made at a lost cost. Nanomaterials are classified based on having at least one dimensionality in the sub micrometer scale. Nanostructured materials such as nanopowders, nanocoatings, nanocomposites, nanoporous material, and biological nanomaterials have been researched extensively in all areas of technology. Breakthroughs have been made in medicine, electronics, energy, biotechnology, and information technology [5]. For example, as mentioned earlier the transistor was invented in the late 1940's being millimeter in size and has heavily improved since. Submicron transistors were achieved during the 1980's when the dynamic random-access memory (DRAM) was produced having megabit storage capacities [6]. By the 21st century, the transistor measured 100 nm across and achieved gigabit memory. It is currently

measured to be 5-10 nm in size. This was possible with the photolithography process and the accessibility of silicon which decreased manufacturing cost from dollars to pennies a piece. The advancement and incorporation of nanotechnology has transformed the world into a global society making it easier for people to connect to the entire world from the palm of their hands.

1.1 Nanomaterials for Environmental Applications: Dry methane reforming

CO_2 and CH_4 are the most prominent greenhouse gases which have contributed to increases in the global surface temperature of earth. A possible environmental application that uses greenhouse gas emissions as a feedstock for value-added chemical commodities is the use of dry methane reforming (DRM) where methane and CO_2 are converted into synthesis gases like H_2 and CO. This reaction is typically done on an active metal catalyst typically nanometer in size [7]. Common DRM catalysts include noble metals (Ru, Rh, Pt, Pd, Ir) and non-noble (Ni, Co, Fe) metals.

Noble metals are highly active and resistant to carbon formation but are not widely used due to their high cost and limited availability [8]. Ni, Co, and Fe have been widely used in DRM due to their high activity, low cost, and wide availability. However, they tend to have fast deactivation due to carbon and coke formation limiting their usability and reducing their overall lifetime [9].

The optimization of the DRM process depends on the material properties of the catalyst nanoparticle and the support. Catalytic activity, selectivity, and stability are important factors to consider when choosing an ideal catalyst. Research has shown that strategies to improve metal dispersion, alloying of heterogeneous catalysts, and choosing

supports with inherent resistance to sintering and low carbon formation can aid in higher activity, selectivity, and stability.

There are several strategies that have been investigated to circumvent the deactivation by carbon formation and extending the lifetime of the catalyst by using a promoter, support effects, ensuring the metal particle size remains small, structure and using bimetallic alloys [10]. A special class of supports used are perovskite metal oxides (PMOs) which have high ion conductivity, overall resistance to coking and sintering, high activity for DMR, and stability [11], [12].

A synthesis method of these metal/perovskite oxide catalysts for DRM is a sol-gel method where the catalyst metals are first constituted in the B-site of the ABO_3 perovskite structure and when heat treated, exsolves, nucleates, and grows on the surface of the perovskite [13]. Stabilizing the active metal phases by perovskite oxide precursors is an effective strategy for obtaining high metal dispersion [14]. The reversibility of the exsolution also allows for the reactivation of the catalyst through a simple redox cycling that allows for multiple uses of the same material without loss of activity and reducing overall material cost.

Metal-supported catalysts offer superior stability because the sintering and agglomeration of the metal particles are inhibited due to the strong metal-support interaction but is reversible by a simple high temperature treatment. With the manipulation of the bulk by changing the synthesis process parameters one can tailor the size, shape, and composition of the active materials to tune their activity, selectivity, and stability of Ni-based catalysts for DRM.

1.2 Carbon Fiber

Another type of nanostructure that has large potential in different sectors of technology are carbon nanofibers. Carbon fiber is a lightweight and strong material that is 5x stronger and 2x stiffer than steel [15]. It is in high demand as a lightweight and strong alternative to metal for various industries such as aeronautics, automotive, and electronics [15]. Carbon fiber has been around since the late 19th century. In 1879, Thomas Edison heated cotton threads or bamboo fibers at high temperatures, carbonizing them into a carbon filament for incandescent lamp filaments [16]. It wasn't until the late 1960's that carbon fiber amassed attention for usage as a structural material. In 1958, Roger Bacon produced high performance carbon fibers at Union Carbide Parma technical center located outside of Cleveland, Ohio [17]. In the early 1960's a process was developed by Dr. Akio Shindo at the Agency of Industrial and Technology of Japan using polyacrylonitrile (PAN) as a precursor material [18]. Around the same time, W. Watt, W. Johnson, and L.N. Phillips of the Royal Aircraft Establishment at Farborough (RAE) worked on the production of carbon fiber from a PAN precursor in 1963 [19]. Different precursors for carbon fiber were used during this decade such as rayon, pitch and polyacrylonitrile (PAN) with Polyacrylonitrile showing higher strength and higher carbon yields. Fiber from PAN fueled the exponential growth of the carbon fiber industry since the 1970's and they are now used in various industries such as space aeronautics, military and commercial aircraft, sporting goods, automotive, and civil engineering [20] [21]. In addition to carbon fiber having high mechanical properties, it also has good electrical conductivity, thermal conductivity, and low linear coefficient of thermal expansion [22].

1.3 Processing of Carbon Fiber from PAN-based fibers

Generally, carbon fiber is manufactured by a controlled pyrolysis of PAN fibers. The typical process consists of the spinning of fibers followed by a three-step heat treatment process including stabilization/oxidation, carbonization, and graphitization (Figure 1.5). The fibers are typically stabilized at temperatures ranging from 200- 400 ºC in air [23]. They are then heat treated in an inert atmosphere at elevated temperatures ranging from 800-3000 ºC in the carbonization and graphitization step to yield high performing carbon fibers.

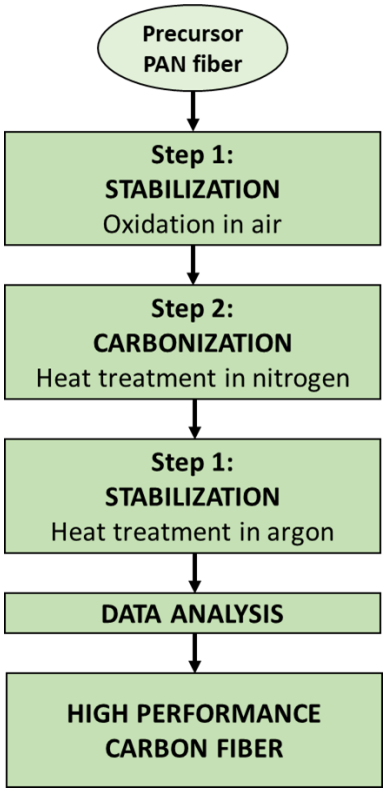

Figure 1.4 PAN precursor carbon fiber processing steps

1.3.1 Polyacrylonitrile (PAN) structure

To understand the PAN stabilization process, we must first look at the chemical structure of polyacrylonitrile and its configuration in fibers. Polyacrylonitrile is a synthetic semicrystalline organic polymer with the linear formula $(C_3H_3N)_n$. seen in Figure 1.6 [24]. The monomer consists of acrylonitrile with the formula CH_2CHCN and has a vinyl group linked to a nitrile group. The nitrile group has a lone pair in the π orbital of the triple bond, making it a highly reactive group and making the polymer soluble in highly ionizing solvents [25]. The chain conformation of PAN is dependant on the nitrile group because of its high dipole moment. Adjacent nitrile groups have intramolecular repulsions which leads to a helical conformation of the PAN [26]. The strong Van der Waals interaction between the helixes form paracrystals, which are then organized into fibrils throughout the fiber (Figure 1.7) [25]. It is important to note that the molecular configuration of a polymer influences the 3D hierarchical structure affecting its material properties. Changing these molecular constituents changes the conformation of the polymer. For example, if the nitrile groups in the polymer have high interparticle repulsion the conformation of the polymer changes from a helix structure to a zigzag affecting its overall crystallinity.

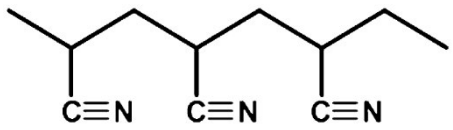

Figure 1.5 Molecular structure of polyacrylonitrile (PAN)

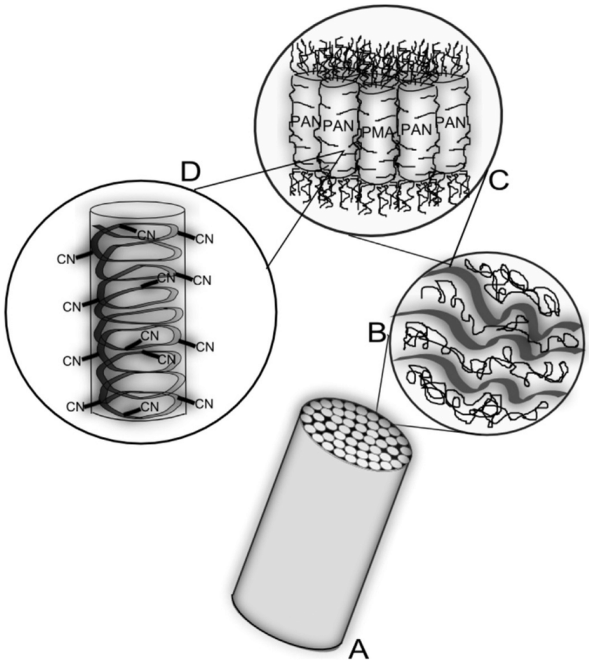

Figure 1.6 Levels of polyacrylonitrile arrangement A) fiber, B) fibril, C) paracrystal D) helix [27]

1.3.2 Stabilization/Oxidation

The stabilization temperature ranges from 200-400 ºC. Fitzer et al. suggested a stabilization temperature of 270 ºC for best performing carbon fiber [28]. The stabilization process involves different chemical reactions such as cyclization, dehydrogenation, aromatization, oxidation, and crosslinking which results in the formation of a six-membered cyclic pyridine ring and a conjugate ladder structure [29], [30]. This heat treatment process changes the chemical structure of the PAN to become thermally stable by crosslinking and cyclizing PAN chains to prevent melting or fusion during higher temperature processing to maximize the carbon yield [31]. Cyclization process occurs via the nitrile group (C≡N), changing from a triple to a double bond, the nitrogen bonding with the carbon (Figure 1.8) [31]. PAN-based fibers undergo a change of color from white to

brown, to ultimately a black color attributing to the formation of the ladder ring structure [30], [32].

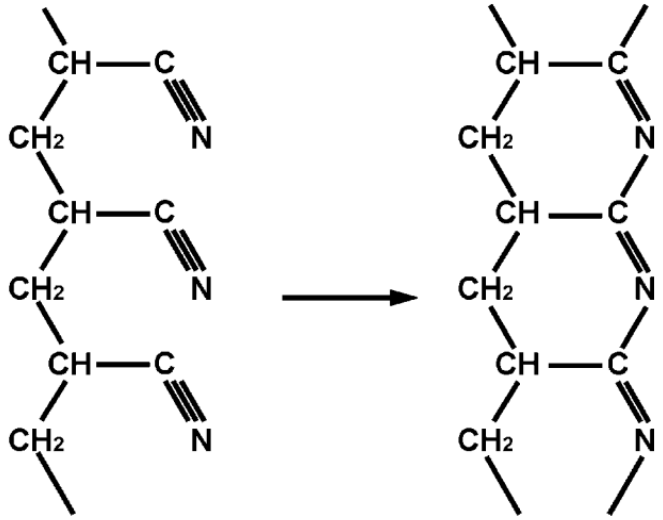

Figure 1.7 Structural change in PAN fibers from open chain polymers to ladder polymers in stabilization stage [33]

Houtz was the first to propose the reaction mechanism of the cyclization process, where he proposed a fully aromatic cyclized structure for PAN homopolymer [34]. However, this is a simplified structure as the presence of oxygen was not considered in the structure [35]. Dehydrogenation occurs when a carbon-carbon double bonds and conjugated structures are generated through the removal of a hydrogen atom by oxidation and the removal of a water molecule thereby stabilizing the structure [36]. Oxygen acts as a dehydrogenation agent during stabilization and forms oxygen containing groups such as OH, CO_2, and CO through direct oxidation [35]. The gaseous species evolved during this process are HCN, H_2O, CO_2, and NH_3. The stabilization process is summarized in (Figure 1.9).

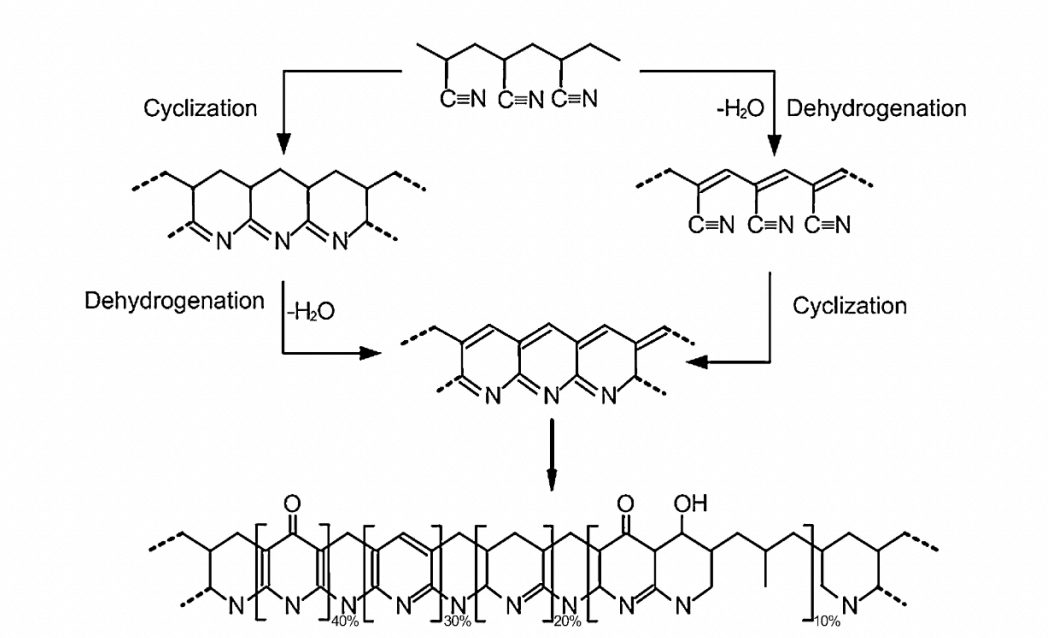

Figure 1.8 Proposed chemistry of PAN stabilization [22]

1.3.3 Carbonization

The carbonization process occurs after the stabilization step being converted into a high strength carbon fiber. It is a polymerization and aromatic growth process where the fiber is treated at high temperatures under an inert atmosphere up to 800-1000 ˚C to remove the non-carbon elements as volatile gas [31], [37]. These elements are volatized as gaseous species such as methane, hydrogen, nitrogen, hydrogen cyanide, water, carbon monoxide, carbon dioxide, ammonia, and various other gases [28]. This process yields a turbostratic carbon structure.

1.3.4 Graphitization

To improve the mechanical performance, the carbonized fibers undergo the graphitization process. Graphitization is the formation of disordered carbon into a 3D graphitic structure by heat treatment and thermal decomposition at elevated temperatures.

During graphitization, carbonized fibers are treated in Argon at temperatures up to 3000 °C. Denitrogenation occurs by the removal of the nitrogen atoms within the carbon ring and begin to link up in the lateral direction resulting in the formation of graphitic like structure (Figure 1.10) [38].

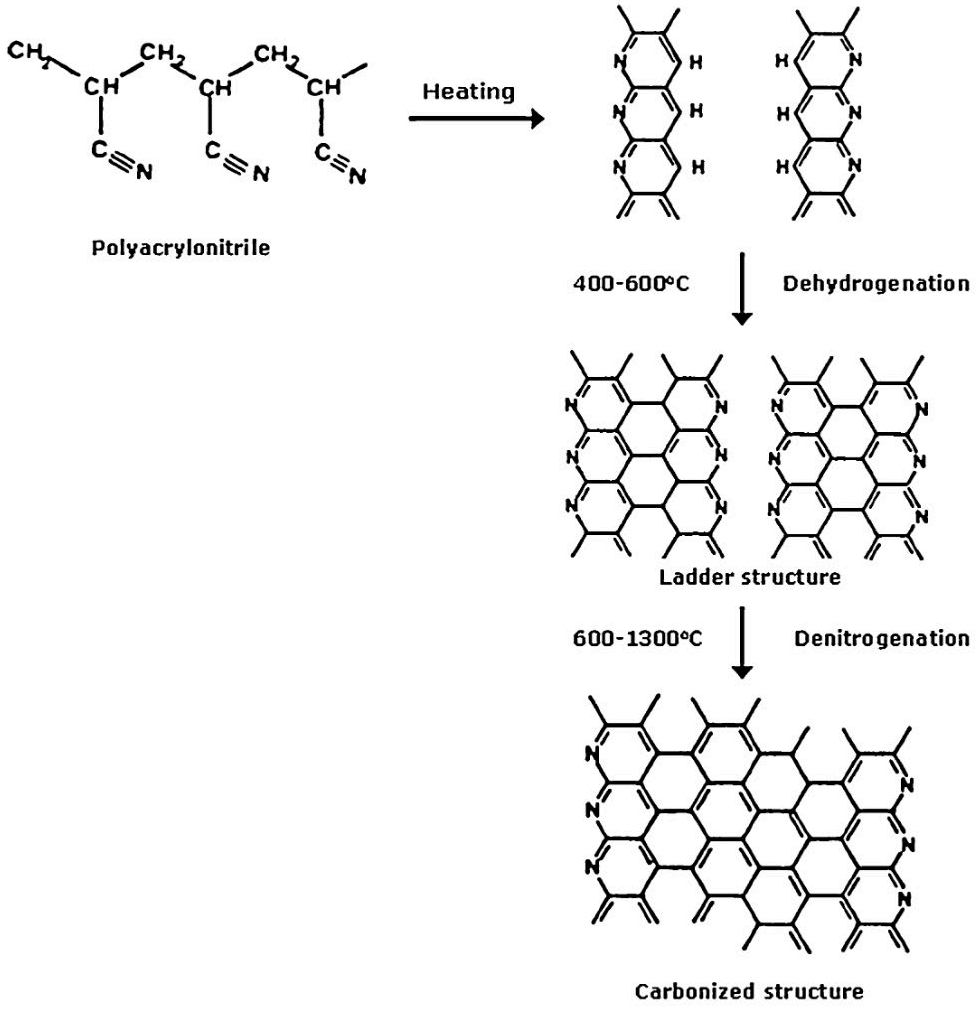

Figure 1.9 Schematic of the formation of carbonized structure from PAN nanofiber

Carbon fiber remains an important material today as it is incorporated into many industries. One prime example is the 737 Boeing airplane that uses carbon fiber as a structural material due to its high strength to weight ratio. Overall, material science and

engineering involve the study of synthesis -structure -property-function relations. To make sure that a material has superior properties in their given applications i.e., high tensile strength in carbon fiber composites for an airplane, understanding how the manufacturing processing technique affects the ultimate structure is important and should continue to be implemented in designing and making a consistent product.

Nanosized carbon fiber has shown to have higher mechanical strength than micron size nanofibers [39]. Typical mechanical failure of carbon fiber composites is due to crack propagation within the composite. Nanofibers would allow for thinner layers that could mitigate cracks. With the usage of nanofibers in reinforced composites, they can provide superior structural property such as high modulus and strength to weight ratio [40], that would allow for the manufacturing of lighter carbon composites. One dimensional (1D) nanofibers have been a strong research focus due to their unique properties and intriguing applications [41]. A promising fabrication method for these 1D structures is the electrospinning method due to its ability to use a variety of polymer and generate sub-micron diameter fibers at a large scale [42]. The first patent of the electrospinning process occurred in 1934 by Formalas who disclosed an apparatus for producing polymer filaments by using electrostatic repulsions between surface charges [41].

1.3.5 Electrospinning

The electrospinning configuration typically includes a high voltage supply, a syringe with a needle tip and a metal grounded collector (Figure 1.11). In a typical electrospinning process a polymer is dissolved and put in a syringe with a metal tip attached to it. The syringe is placed on a syringe pump to extrude the solution at a constant rate. A

high voltage is applied to the needle tip and the grounded collector. Electrostatic charging is induced on the polymer fluid at the tip of the nozzle and forms a Taylor cone which is a cone shaped droplet caused by the surface tension of the liquid. When the electrostatic force overcomes the surface tension of the polymer solution, a jet is ejected from the tip, elongating, and split into thinner filaments solidifying, and eventually landing on the grounded collector. Sometimes a rolling collector is used to create unidirectional membranous mats.

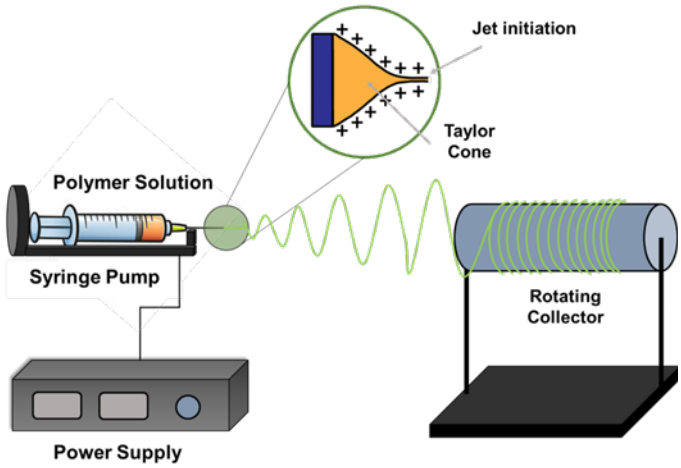

Figure 1.10 Schematic of a basic electrospinning setup with a rolling collector

There are several processing parameters that affect the nanofiber morphology and size including electric potential, distance between collector and needle tip, humidity, flow rate and viscosity of the polymer solution [41].

Applications that have used nanofibers include filtration, wound dressing, tissue templating and electrical applications because they provide high surface to volume ratio, high porosity in addition to their physico-mechanical properties [40], [42]. In addition to these enhanced mechanical properties, a multifunctionality component can be added with

the addition of materials such as ceramics, metals, and metal oxides. For example, ZnO, TiO_2, NiO and CuO have been prepared by calcination of electrospun nanofibers containing polymer and inorganic precursor [43]. Nanoparticle nanofiber composites have been researched extensively due to their functionality and unique chemical and physical properties [44]. Electronic and optical properties of nanostructured materials have been of interest because of their superior performance exploiting unique properties such as quantum confinement of charge carriers and high surface to volume ratio that allows for more active material [45]. Metal/polymer nanocomposites are expected to be applied as catalysts, in photonics, electrical sensors, filters and artificial tissues [46]. Integration of nanofibers into nano-matrices require nanofibers with controlled orientation, size, and other target characteristics as well as reproducibility. The addition of the multifunctionality component adds a complexity to this nanofiber system. The ability to control the size, phase, and morphology of these multifunctional nanomaterials remains a major challenge in the field [47]. By understanding the processing parameters that affect the structure and properties of these nanocomposite systems we can optimize the material production and tailor it to the desired application. To take full advantage of nanomaterials and their unique properties, we must first study their processing-structure-property relations.

Materials Science and Engineering involves four sections, processing, structure, properties, and performance with characterization being a tool to analyze materials (Figure 2). How a material is processed will influence its structure which will affect its properties and remains a function of its performance. An example of this is elucidated in the production of carbon fiber.

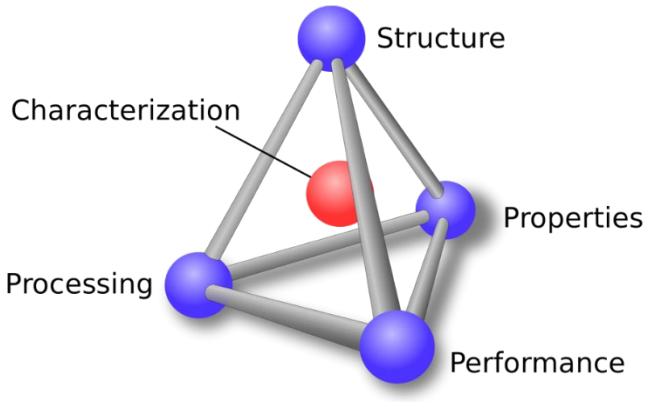

Figure 1.11 The Materials Science tetrahedron, describing the interrelationship between processing-structure-property-performance.

The aim of this dissertation is to understand the structure-property relations of nanomaterials by 1) identifying growth mechanisms of Ni nanoparticles in a carbon nanofiber matrix 2) identifying carbonization mechanisms of Ni/carbon nanofibers 3) studying the synthesis-structure relations of TiO_2/carbon nanofibers for water purification application 4) perform dynamic studies on Ni and Fe exsolution in perovskite-based materials in redox environments for dry methane reforming

References

[1] W. D. Callister and D. G. Rethwisch, *Materials science and engineering : an introduction*, 10th ed. 2018.

[2] M. F. Ashby, H. Shercliff, and D. Cebon, *Materials : engineering, science, processing and design*, 4th ed. 2007.

[3] S. C. Davis and R. G. Boundy, *Home - Transportation Energy Data Book Transportation Energy Data Book*. Oak Ridge, 2020.

[4] "Sources of Greenhouse Gas Emissions | US EPA." [Online]. Available: https://www.epa.gov/ghgemissions/sources-greenhouse-gas-emissions. [Accessed: 18-May-2022].

[5] R. K. Goyal, *Nanomaterials and Nanocomposites : synthesis, properties, characterization techniques, and... applications.* CRC PRESS, 2020.

[6] M. Riordan, "transistor | Definition & Uses | Britannica." [Online]. Available: https://www.britannica.com/technology/transistor. [Accessed: 18-May-2022].

[7] N. A. K. Aramouni, J. G. Touma, B. A. Tarboush, J. Zeaiter, and M. N. Ahmad, "Catalyst design for dry reforming of methane: Analysis review," *Renew. Sustain. Energy Rev.*, vol. 82, pp. 2570–2585, Feb. 2018.

[8] Z. Hou, P. Chen, H. Fang, X. Zheng, and T. Yashima, "Production of synthesis gas via methane reforming with CO2 on noble metals and small amount of noble-(Rh-) promoted Ni catalysts," *Int. J. Hydrogen Energy*, vol. 31, no. 5, pp. 555–561, Apr. 2006.

[9] A. E. Castro Luna and M. E. Iriarte, "Carbon dioxide reforming of methane over a metal modified Ni-Al2O3 catalyst," *Appl. Catal. A Gen.*, vol. 343, no. 1–2, pp. 10–15, Jul. 2008.

[10] K. Mette *et al.*, "High-Temperature Stable Ni Nanoparticles for the Dry Reforming of Methane," *ACS Catal.*, vol. 6, no. 10, pp. 7238–7248, Sep. 2016.

[11] J. Deng, M. Cai, W. Sun, X. Liao, W. Chu, and X. S. Zhao, "Oxidative Methane Reforming with an Intelligent Catalyst: Sintering-Tolerant Supported Nickel Nanoparticles," *ChemSusChem*, vol. 6, no. 11, pp. 2061–2065, Oct. 2013.

[12] P. Steiger *et al.*, "Structural Reversibility and Nickel Particle stability in Lanthanum Iron Nickel Perovskite-Type Catalysts," *ChemSusChem*, vol. 10, no. 11, pp. 2505–2517, Mar. 2017.

[13] J. Mizuki *et al.*, “Self-regeneration of a Pd-perovskite catalyst for automotive emissions control,” *Nature*, vol. 418, pp. 164–167, 2002.

[14] A. Cao, R. Lu, and G. Veser, “Stabilizing metal nanoparticles for heterogeneous catalysis,” *Phys. Chem. Chem. Phys.*, vol. 12, no. 41, pp. 13499–13510, 2010.

[15] P. Bajpai, *Carbon fiber*. Elsevier.

[16] T. Edison, “Electric Lamp,” 223898, 27-Jan-1880.

[17] M. M. Tang and R. Bacon, “Carbonization of cellulose fibers-I. Low temperature pyrolysis,” *Carbon N. Y.*, vol. 2, no. 3, pp. 211–220, 1964.

[18] A. Shindo, “Studies on graphite fibre,” Osaka, 1961.

[19] P. Morgan, *Carbon Fibers and Their Composites*. Boca Raton: CRC Press, 2005.

[20] D. D. L. Chung, *Carbon fiber composites*. 1994.

[21] H. Jaeger and W. Frohs, Eds., *Industrial carbon and graphite materials : raw materials, production and applications*. 2021.

[22] J.-B. Donnet, T. K. Wang, S. Rebouillat, and J. C. M. Peng, *Carbon fibers: Revised and expanded*, 3rd ed. Boca Raton: CRC Press, 1998.

[23] X. Huang, “Fabrication and Properties of Carbon Fibers,” *Mater.* , vol. 2, no. 4, pp. 2369–2403, Dec. 2009.

[24] Y. Qin, *Medical Textile Materials*, 1st ed. Elsevier Inc., 2015.

[25] O. A. Andreeva and L. A. Burkova, “Spectroscopic Manifestations of Nitrile Group Intermolecular Attraction in PAN,” *J. Macromol. Sci. Part B*, vol. 39, no. 2, pp. 225–234, 2007.

[26] W. R. Krigbaum and N. Tokita, “Melting point depression study of polyacrylonitrile,” *J. Polym. Sci.*, vol. 43, no. 142, pp. 467–488, Apr. 1960.

[27] I. Karbownik, M. Fiedot, O. Rac, P. Suchorska-Woźniak, T. Rybicki, and H. Teterycz, “Effect of doping polyacrylonitrile fibers on their structural and mechanical properties,” *Polymer (Guildf).*, vol. 75, pp. 97–108, 2015.

[28] E. Fitzer, W. Frohs, and M. Heine, “Optimization of stabilization and carbonization treatment of PAN fibres and structural characterization of the resulting carbon fibres,” *Carbon N. Y.*, vol. 24, no. 4, pp. 387–395, Jan. 1986.

[29] Z. Bashir, “A critical review of the stabilisation of polyacrylonitrile,” *Carbon N.*

Y., vol. 29, no. 8, pp. 1081–1090, Jan. 1991.

[30] M. S. A. Rahaman, A. F. Ismail, and A. Mustafa, "A review of heat treatment on polyacrylonitrile fiber," *Polym. Degrad. Stab.*, vol. 92, no. 8, pp. 1421–1432, Aug. 2007.

[31] N. Yusof and A. F. Ismail, "Post spinning and pyrolysis processes of polyacrylonitrile (PAN)-based carbon fiber and activated carbon fiber: A review," *J. Anal. Appl. Pyrolysis*, vol. 93, pp. 1–13, Jan. 2012.

[32] H. N. Friedlander, L. H. Peebles, J. Brandrup, and J. R. Kirby, "On the chromophore of polyacrylonitrile. VI. Mechanism of color formation in polyacrylonitrile," *Macromolecules*, vol. 1, no. 1, pp. 79–86, Jan. 1968.

[33] A. Shokuhfar, A. Sedghi, and R. E. Farsani, "Effect of thermal characteristics of commercial and special polyacrylonitrile fibres on the fabrication of carbon fibres," *http://dx.doi.org/10.1179/174328406X129887*, vol. 22, no. 10, pp. 1235–1239, Oct. 2013.

[34] R. C. Houtz, "'Orlon' Acrylic Fiber: Chemistry and Properties:," *http://dx.doi.org/10.1177/004051755002001107*, vol. 20, no. 11, pp. 786–801, Nov. 1950.

[35] E. Fitzer and D. J. Müller, "The influence of oxygen on the chemical reactions during stabilization of pan as carbon fiber precursor," *Carbon N. Y.*, vol. 13, no. 1, pp. 63–69, Feb. 1975.

[36] Y. Xue, J. Liu, and J. Liang, "Kinetic study of the dehydrogenation reaction in polyacrylonitrile-based carbon fiber precursors during thermal stabilization," *J. Appl. Polym. Sci.*, vol. 127, no. 1, pp. 237–245, Jan. 2013.

[37] T. -H Ko and T. -C Day, "The effect of pre-carbonization on the properties of PAN-based carbon fibers," *Polym. Compos.*, vol. 15, no. 6, pp. 401–407, Dec. 1994.

[38] S. K. Nataraj, K. S. Yang, and T. M. Aminabhavi, "Polyacrylonitrile-based nanofibers—A state-of-the-art review," *Prog. Polym. Sci.*, vol. 37, no. 3, pp. 487–513, 2012.

[39] L. Zhang, A. Aboagye, A. Kelkar, C. Lai, and H. Fong, "A review: Carbon nanofibers from electrospun polyacrylonitrile and their applications," *J. Mater. Sci.*, vol. 49, no. 2, pp. 463–480, 2014.

[40] Z. M. Huang, Y. Z. Zhang, M. Kotaki, and S. Ramakrishna, "A review on polymer nanofibers by electrospinning and their applications in nanocomposites," *Compos.*

Sci. Technol., vol. 63, no. 15, pp. 2223–2253, 2003.

[41] D. Li and Y. Xia, "Electrospinning of nanofibers: Reinventing the wheel?," *Adv. Mater.*, vol. 16, no. 14, pp. 1151–1170, 2004.

[42] N. Bhardwaj and S. C. Kundu, "Electrospinning: A fascinating fiber fabrication technique," *Biotechnol. Adv.*, vol. 28, no. 3, pp. 325–347, May 2010.

[43] N. A. M. Barakat, K. A. Khalil, I. H. Mahmoud, M. A. Kanjwal, F. A. Sheikh, and H. Y. Kim, "CoNi bimetallic nanofibers by electrospinning: Nickel-based soft magnetic material with improved magnetic properties," *J. Phys. Chem. C*, vol. 114, no. 37, pp. 15589–15593, Sep. 2010.

[44] L. Burke *et al.*, "In-situ synthesis of magnetic iron-oxide nanoparticle-nanofibre composites using electrospinning," *Mater. Sci. Eng. C*, vol. 70, no. 1, pp. 512–519, Jan. 2017.

[45] X. Yang, C. Shao, H. Guan, X. Li, and J. Gong, "Preparation and characterization of ZnO nanofibers by using electrospun PVA/zinc acetate composite fiber as precursor," *Inorg. Chem. Commun.*, vol. 7, no. 2, pp. 176–178, Feb. 2004.

[46] Y. Wang *et al.*, "Preparation of silver nanoparticles dispersed in polyacrylonitrile nanofiber film spun by electrospinning," *Mater. Lett.*, 2005.

[47] I. S. Chronakis, "Novel nanocomposites and nanoceramics based on polymer nanofibers using electrospinning process—A review," *J. Mater. Process. Technol.*, vol. 167, no. 2–3, pp. 283–293, Aug. 2005.

Chapter 2 Synthesis-Structure relations of Ni nanoparticles within a nanofiber carbon matrix

2.1 Background

Size, morphology, and high conductivity are critical factors for sustainable technologies. Precious metals like platinum are most used in energy technologies such as fuel cells [1]. However, its high cost and scarcity has hampered automotive and renewable energy technologies driving research to more affordable materials [2]. As a result, nonprecious materials like carbon and metal catalysts have been explored as alternative materials [3]. Carbon materials have been playing a significant role in the development of alternative clean and sustainable technologies. This includes structures like carbon nanotubes, fullerenes, graphene, and other porous carbon structures which are of particular interest as low-cost materials for a variety of energy applications [4] [5]. Metal nanomaterials have received significant attention to their unique properties and their potential applications in optical, electronic, catalytic, and biological applications [6]. Forming heterostructures with transition metal/metal oxide (e.g., Fe, Co, Ni, Mn) could modify their chemical activities. Metal nanoparticles have also been seen to have catalytic effect on graphitization and have been extensively used for synthesis of carbon nanotubes [7].

Researchers have also focused on making hierarchical nanostructures for increase in surface area [8] [9]. 1D graphitic structures provide the necessary charged conductivity and 3D conductive networks have been considered as a promising solution due to their large aspect ratio, high surface area, short diffusion path for electrons which are favorable for

energy applications such as batteries and fuel cells [10]. One of these structures are electrospun nanofiber mats. Although there has been research done on this system, the mechanism of metal nanoparticle growth within this system has yet to be determined. This work focuses on temperatures studies and finding the mechanism of crystal growth and transformation of Ni metal nanoparticles within this carbon matrix.

2.2 Objectives and hypotheses

The objectives of this work are to synthesize Ni/carbon nanofibers from an electrospun polymer-metal precursor. Upon annealing, metal species diffuse through the carbon matrix, nucleating as metal nanoparticles and subsequently catalyzing the formation of graphitic structures. In this study, we investigate the role of the polymer matrix and annealing conditions on metal diffusion, clustering, and growth of these metal nanoparticles. We utilize these parameters to control the size, number density, surface area of metal nanostructures that ultimately allow us to tune our material for use in sensing elements and water purification membranes.

2.3 Materials and Methods

2.3.1 Materials

All chemicals and reagents were used as received. Nickel (II) acetate tetrahydrate (98%), polyacrylonitrile (PAN) (molecular weight (MW) ≈130 000), and N,N-dimethylformamide (DMF) (anhydrous, 99%) were all purchased from Sigma-Aldrich. Compressed air, ultrapure Argon, and 5% H_2/95% N_2, were supplied by Airgas.

2.3.2 Material synthesis:

Solution Prep and electrospinning

To synthesize Ni-PAN nanofibers, 1.2 g of PAN and 0.25 g of $Ni(OAc)_2 \cdot 4\ H_2O$ were dispersed into 8.8 g of DMF solution in a 20 mL vial followed by stirring at 500 rpm for 6 h at 80 °C with subsequent stirring for 12 h at room temperature (Figure 1.1 A). The solution was then transferred into a 10 mL plastic syringe with a stainless-steel needle tip and electrospun using an eS-robot electrospinning/spray system (NanoNC, Seoul, Korea). A flow rate of 1.0 mL min^{-1} was used and a voltage of 15kV (10, -5kV) was generated by a power supply (Hi-2000, Korea Electric Testing Institute) was applied between the needle and a rolling aluminum foil collector (~1500 rpm) at 20 cm distance from needle tip to collector (summarized in Figure 1.1 B). The electrospinning process was performed at room temperature for 2 h. As-spun nanofibers were dried in air for 24 h at room temperature before further processing and characterization.

Heat treatment of nanofibers

The dried nanofiber mats were placed in an alumina crucible and put into a tube furnace (Thermo Scientific Lindberg Blue M Mini Mite Tube Furnace, ThermoFisher Scientific, USA) for a two-step heating process. The fibers were first heated in air at 250 °C for 4 h with a heating rate of 2 °C/min to stabilize and cyclize the PAN . The gas was immediately switched to $5\%H_2;95\%N_2$ and heated from 300 °C to 800 °C in 1-hour increments.

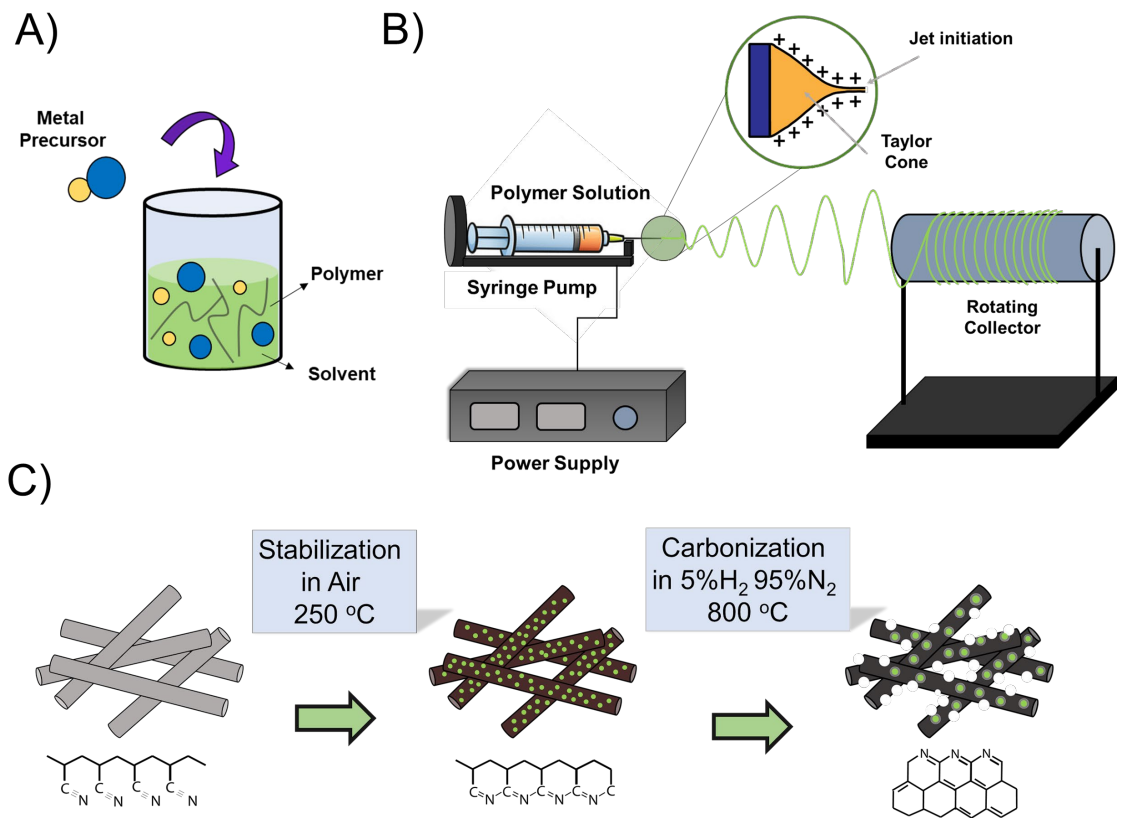

Figure 2.1 A) Metal precursor and polymer mixture in solvent for electrospinning B) electrospinning setup using rotating collector C) heat treatment process for carbonization of nanofibers and metal nanoparticle growth

2.3.3 Material Characterization

Scanning Electron Microscopy (SEM): Samples were mounted on aluminum mounts using carbon tape and sputter coated with platinum and palladium for 30 seconds (Cressington 108 Auto, CFAMM UCR). Particle size, distribution, and morphology were observed using a Scanning Electron Microscope (Mira3, Tescan, CFAMM UCR) at 10 kV.

Transmission Electron Microscopy (TEM) Morphological features and crystallinity of samples were observed using TEM (Titan Thermi-300kC, FEI) bright field imaging. TEM samples were prepared by dispersing fibrous samples in DI water, sonicating for 10 minutes, and depositing them onto ultrathin carbon films on holy carbon supports with a

400-mesh copper grid (Ted Pella, Redding CA) using a 1 mL pipette. To get cross sectional TEM micrographs of nanofibers, samples were embedded in epoxy resin (Max 1618, Polymer Composites, USA) and placed in silicone molds at room temperature overnight. 70 nm cross-sections were obtained using an ultramicrotome (RMC MT-X, Boeckeler Instruments, CFAMM UCR) and a diamond knife (PELCO, Ted Pella). The acquired cross-sections were then placed onto a carbon-coated copper TEM grid for further imaging.

(XRD) Phase Identification was determined by XRD (PANalytical Empyrean Series 2) using Cu Kα radiation. The sample was ground up using a mortar and pestle and placed on a zero background Silicon wafer and onto the sample holder. Crystallite size was calculated from calculating the full width half maximum (FWHM) of the X-ray diffraction profiles and using the Scherrer equation where K is the Scherrer constant, λ is the wavelength of light used for the diffraction, β is the FWHM and θ is the angle measured.

$$D = \frac{K\lambda}{\beta \cos \theta}$$

(TGA) Thermogravimetric analysis (TGA) was performed on a Mettler-Toledo TGA/DSC 3+ following the same oxidation and annealing procedures at a heating rate of 10 ^{o}C/min but using 50 mL/min of 4% H_2/ Argon to decrease risk of damage to platinum elements in the instrument.

(TGA-MS) Thermogravimetric analysis with a mass spectrometer attachment was performed on a TA Discovery TGA-MS from 25 °C to 800 °C in 5%H_2; 95%N_2.

2.4 Results and discussion

2.4.1 Characterization of nanofibers

The metal-polymer nanofibers were turned into carbon fiber using the two-step heat treatment process used in carbon fiber manufacturing (Figure 2.1 C). As-spun Ni-containing fibers exhibit a rough fibrous morphology with an average diameter of 1.2 µm ± 170 nm (Figure 2.2 A). The roughness is caused by high humidity during electrospinning. After annealing at 800 °C for 3 h, the Ni-PAN nanofibers become highly porous with a reduced average diameter of 794 nm ± 36 nm, a 33% reduction indicating the decomposition and carbonization of the fiber. Nanoparticles with average size of 70 nm ± 22 nm can be seen on the surface of the nanofiber.

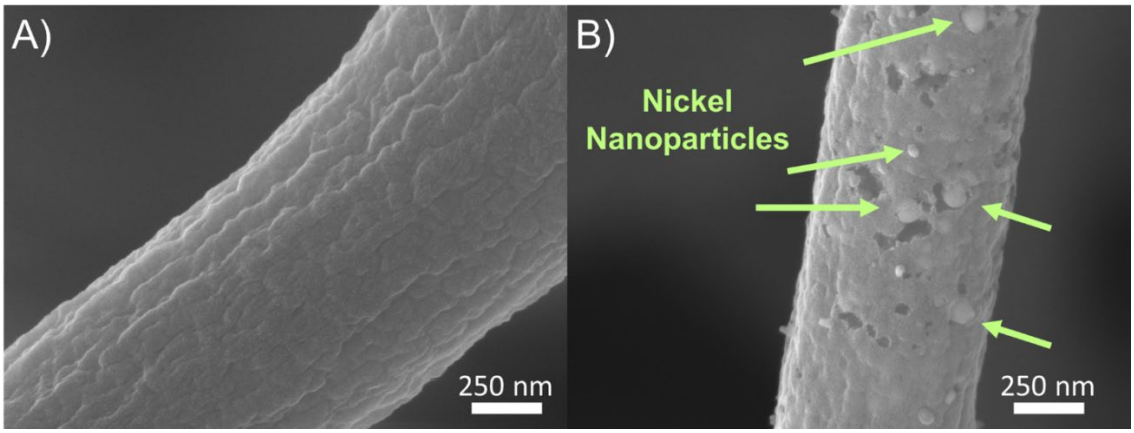

Figure 2.2 A) SEM of as-spun Ni-PAN nanofiber B) SEM of carbonized Ni-PAN nanofiber annealed @800 °C for 3 h.

TEM micrographs of the carbonized Ni-PAN at 800 °C for 3 h shows metal nanoparticles evenly distributed throughout the fiber (Figure 2.3 A). The Ni nanoparticle size ranges from 23 nm to 134 nm. The histogram in Figure 2.2 A inset shows the distribution of particle size throughout the nanofiber. The average particle size is 66 ± 29 nm. There is a wide range of particle size distribution. TEM provides more insight on the porosity of the

fiber. Figure 2.3 B shows the highly porous structure made up of layered carbon throughout the entire nanofiber. HRTEM of a single Ni particle (Figure 2.3 C &D) shows an average 20 layers of ordered carbon surrounding the particle. The layers are ordered carbon that was assumed to have been catalyzed by the Ni as it is a known catalyst for graphitization. FFT in Figure 2.3 C shows that the ordered rings have a d-spacing of 0.35 nm corresponding to the (002) graphite. However, the d-spacing is larger than that of pure graphite and typically corresponds to turbostratic carbon which has the hexagonal carbon structure of graphite, but the basal planes have slipped out of alignment. The nanoparticle d-spacing is 0.2 nm corresponding to the typical fcc Ni metal structure.

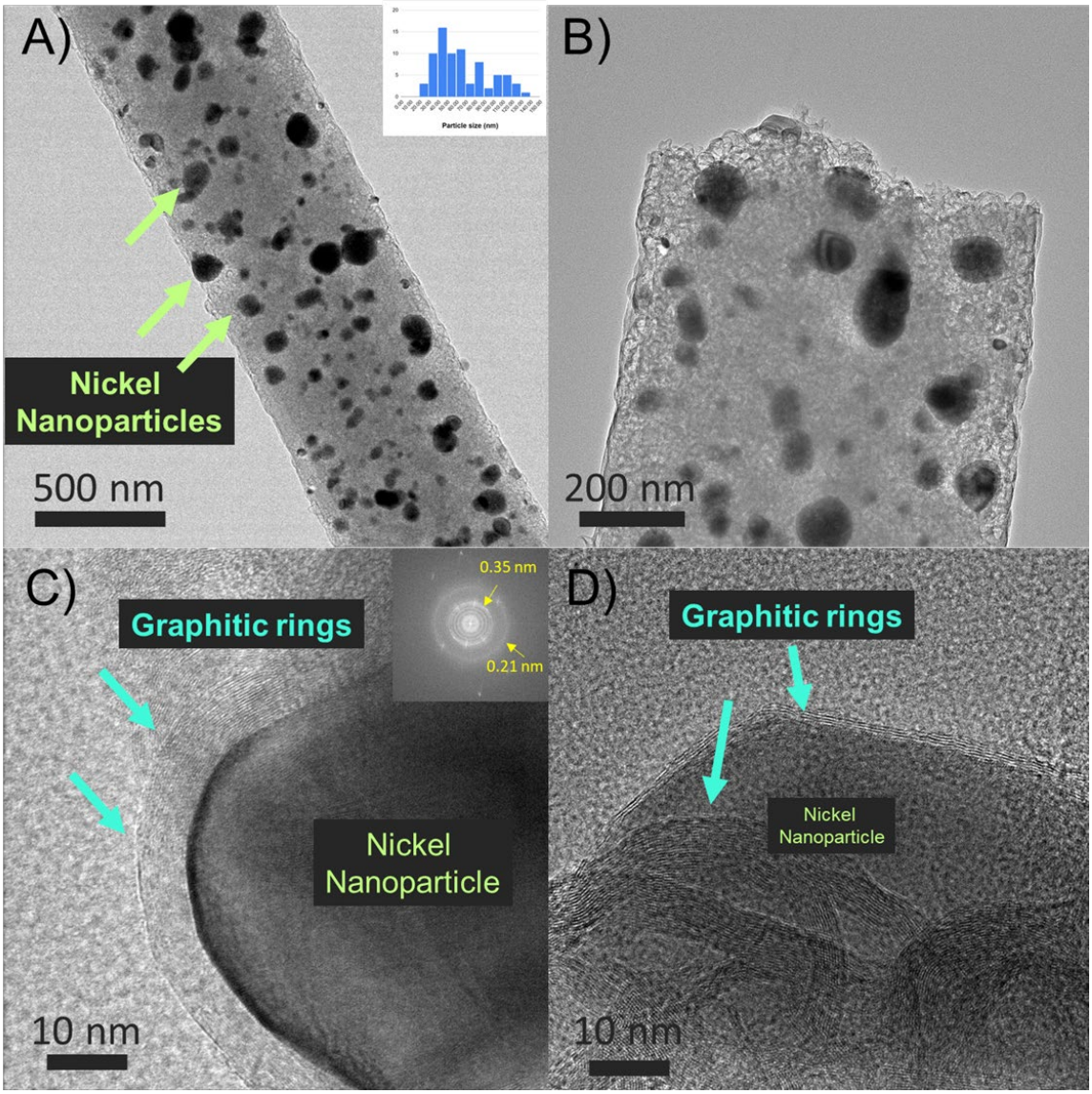

Figure 2.3 A) TEM micrograph of Ni-PAN nanofiber annealed @800 ºC for 3 h in 5%H_2;95%N_2 B) TEM micrograph of Ni-PAN nanofiber tip annealed @800 ºC for 3 h in 5%H_2;95%N_2 C) & D) HRTEM of a Nickel nanoparticle encapsulated with graphitic rings.

XRD of the 800 °C 3 h Ni-PAN sample (Figure 2.4) confirms that the metal precursor has been reduced to Ni metal and has a crystallite size of 40 nm ± 2 nm. The (002) graphitic peak is also seen at 25.9 degrees 2θ with a crystallite size of 4.3 ± 0.4 nm. Typical graphite (002) 2θ is at 26.4 degrees. The shift towards lower 2θ indicates a larger d-spacing. When compared to an annealed PAN fiber with no metal, the graphitic domains are only 1.2 nm,

and the d-spacing is 0.36 nm representing ordered carbon that has not been graphitized. The annealing of Ni-PAN nanofiber in the two-step heating process used for carbon fiber synthesis results in large Ni nanoparticles distributed throughout the carbonized fiber and is indicative that the Ni facilitates graphitization and ordering of the surrounding carbon resulting in a highly porous nanofiber.

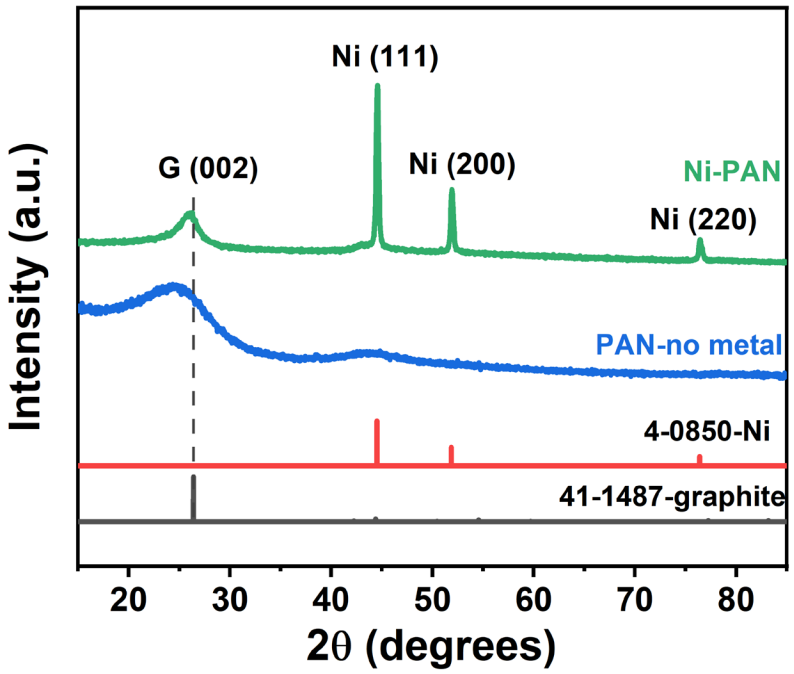

Figure 2.4 XRD of PAN with no metal and Ni-PAN nanofibers annealed @800 °C for 3 h in 5%H_2;95%N_2.

2.4.2 Phase transformation

To observe the crystal and particle growth of the Ni within the polymer matrix as it transforms into carbon fiber, the fibers were heat treated at temperatures from 300 °C - 800 °C for 3 h. Figure 2.4 shows XRD of annealed Ni-PAN nanofibers at varying temperatures.

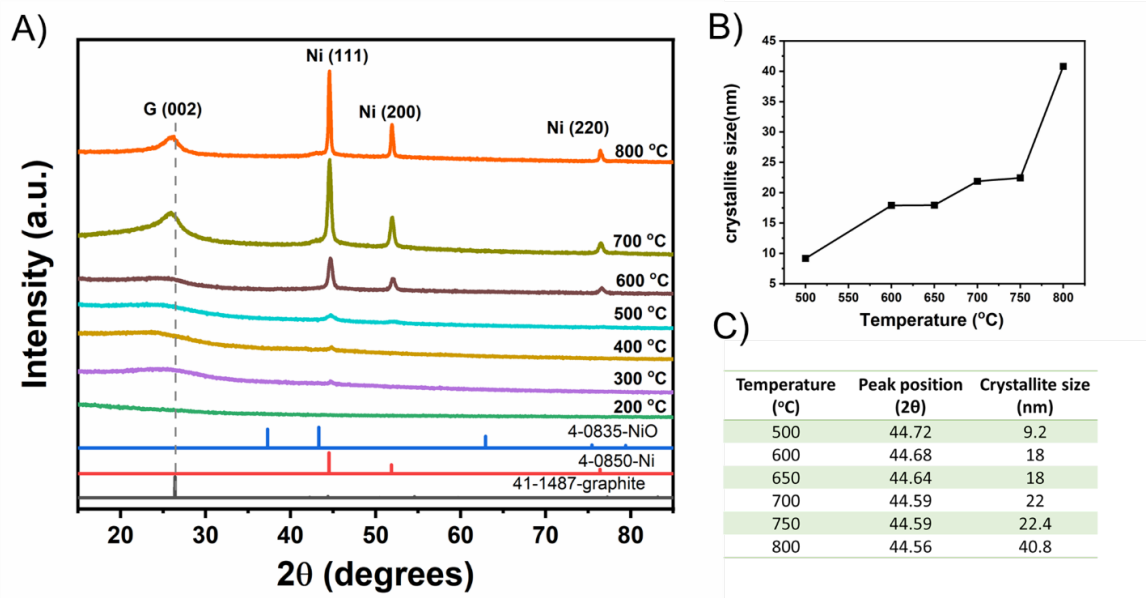

Temperature (°C)	Peak position (2θ)	Crystallite size (nm)
500	44.72	9.2
600	44.68	18
650	44.64	18
700	44.59	22
750	44.59	22.4
800	44.56	40.8

Figure 2.5 A) XRD of Ni-PAN nanofibers annealed at varying temperatures 300 °C- 800 °C for 3 h B) crystallite size plot of Ni metal in Ni-PAN nanofibers vs. temperature annealed C) Table of crystallite size and 2θ peak positions at varying annealing temperatures.

Nickel crystal peaks are observed at 300 °C indicating that crystal growth is already initiated at this temperature. The metal peak progressively increases in intensity as temperature increases indicating the frequency in which the nickel periodicity is scattered. The peak intensity from 300 °C- 500 °C is relatively low indicating small amounts of Ni crystals present at these temperatures. The peak intensity continues to grow and reaches a maximum at 700 °C. The narrowing of the XRD peaks is an indication of the increase in crystallite size which is shown in the table and plot of Figure 2.4 B & C. The crystallite size at 500 °C is 9.2 nm. At 600 °C and 650 °C the crystallite size is very similar in size being 18 nm, showing a slower rate of nickel crystal growth. At 700 °C and 750 °C the crystal size is ~22 nm. At 800 °C the crystal size jumps to 40.8 nm in size. The rate of crystal growth is the fastest between 700 °C and 800 °C with the difference in average

crystal size being 20 nm. It appears the rate of crystal growth is the slowest between the 600 °C and 700 °C.

To compare polymer effects with Ni crystal growth, $Ni(OAc)_2 \cdot 4\ H_2O$ was prepared the same way as the Ni-PAN samples were to electrospin and carbonize the nanofibers. $Ni(OAc)_2 \cdot 4\ H_2O$ was dissolved in DMF, dried, and heat treated using the two-step heating process as mentioned earlier in this chapter. The sample was annealed at varying temperatures of 400 °C, 600 °C, and 800 °C for 3 h. XRD was done to observe the metal crystallization at each temperature including the stabilization step (Figure 2.6 A). During the stabilization in air at 250 °C for 4h, NiO peaks are observed. Using the Scherrer equation, the crystallite size is 1-2 nm. No visible NiO peaks are observed in the Ni-PAN sample. The stabilization temperature is high enough to induce nucleation and crystallization of the dissolved $Ni(OAc)_2 \cdot 4\ H_2O$ to NiO. At 400 °C, the NiO is reduced to nickel metal and the peak intensity is similar at 600 °C and 800 °C. The crystallite size is graphed and summarized in Figure 2.4 B & C. When no polymer is present, nickel crystal size grows to >30nm in size at a low temperature of 400 °C suggesting that polyacrylonitrile slows down the crystal growth rate of the Ni when confined in a polymer matrix.

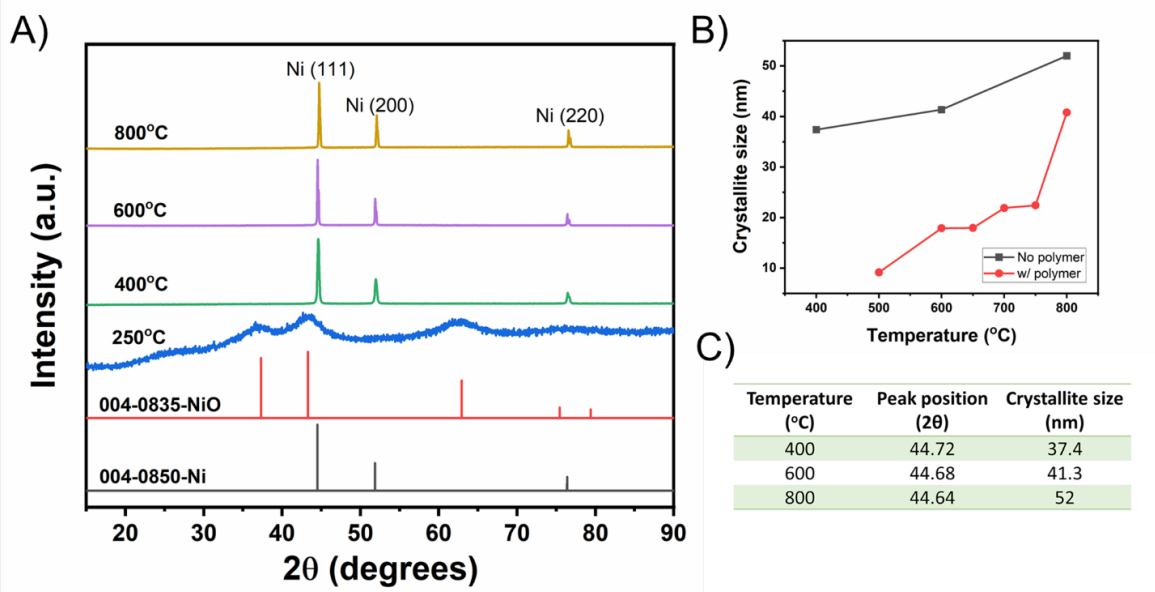

Temperature (°C)	Peak position (2θ)	Crystallite size (nm)
400	44.72	37.4
600	44.68	41.3
800	44.64	52

Figure 2.6 XRD of Ni precursor dissolved in DMF with no polymer stabilized in air at 250 °C for 4h, heat treated in 5%H_2;95%N_2 with no polymer at varying temperatures of 400 °C, 600 °C and 800 °C for 3 h.

Nickel particles grow within the carbon matrix with increasing temperature. Figure 1.7A-F shows TEM micrographs of Ni/Carbon nanofibers annealed at 300 °C- 800 °C for 3 h. At 300 °C (Figure 2.7 A) no visible particles can be seen throughout the fiber. At 400 °C small 6.7 ± 1.2 nm particles can be seen throughout the fiber with regions having concentrated areas of small particles. At 500 °C (Figure 2.7 C) the particles are evenly distributed with an average particle size of 11.4 ± 2.5 nm. At 600 °C (Figure 2.7 D) porosity is observed, and particles have grown to an average size of 23.5 ± 7 nm. At 700 °C (Figure 2.7 E) particles are 31.5 ± 9.7 nm average size. At 800 °C (Figure 2.7 F) the particles have increased significantly to an average size of 66 ± 28.7 nm.

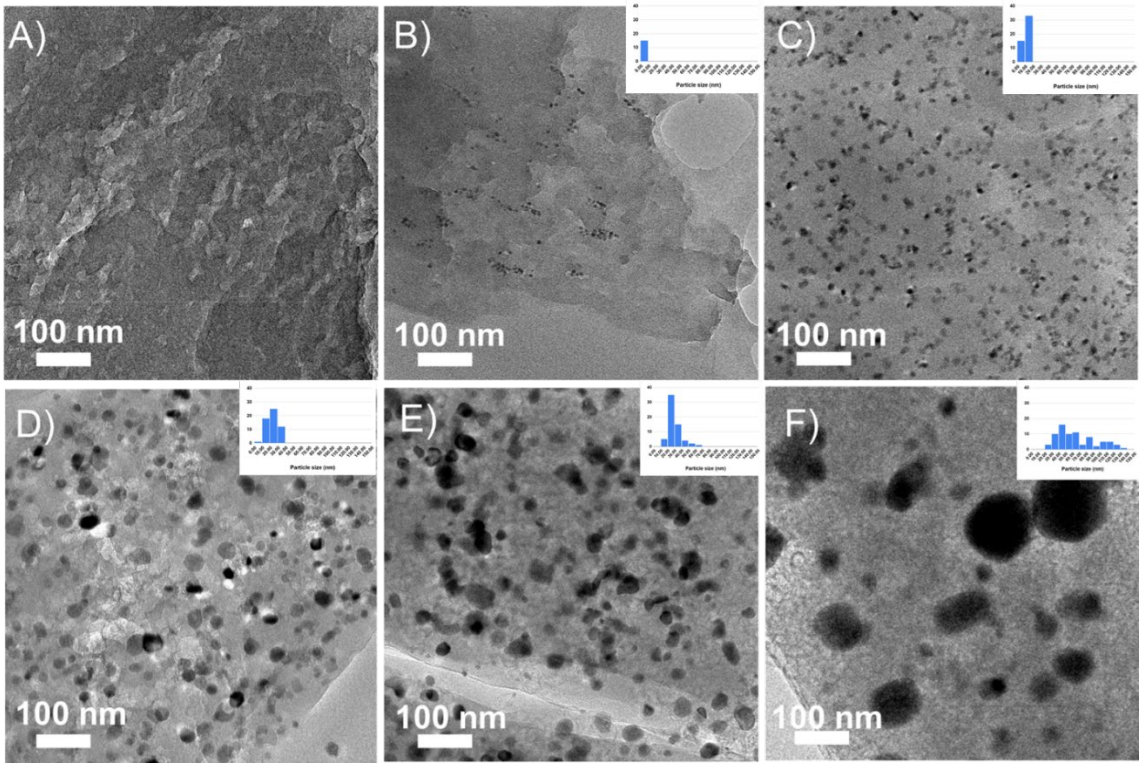

Figure 2.7 TEM of Ni-PAN nanofiber annealed at A) 300 °C B) 400 °C C) 500 °C D) 600 °C E) 700 °C F) 800 °C for 3 h in 5%H_2; 95%N_2.

Particle size vs. temperature is summarized in Figure 2.8. The plot has three distinct regions where the slope of the plot changes from 400 °C- 600 °C, 600 °C- 750 °C and 750 °C- 800 °C. There is a steady growth of particle size from 400 °C to 600 °C with particle size doubling in size every 100 °C. However, from 600 °C to 750 °C particle growth slows down. It is not until 800 °C where the particle growth accelerates to average particle size of 66 ± 28.7 nm. It is important to note that the distribution of particle size begins to increase at 600 °C. At 800 °C particle size varies significantly from 23 nm to 134 nm.

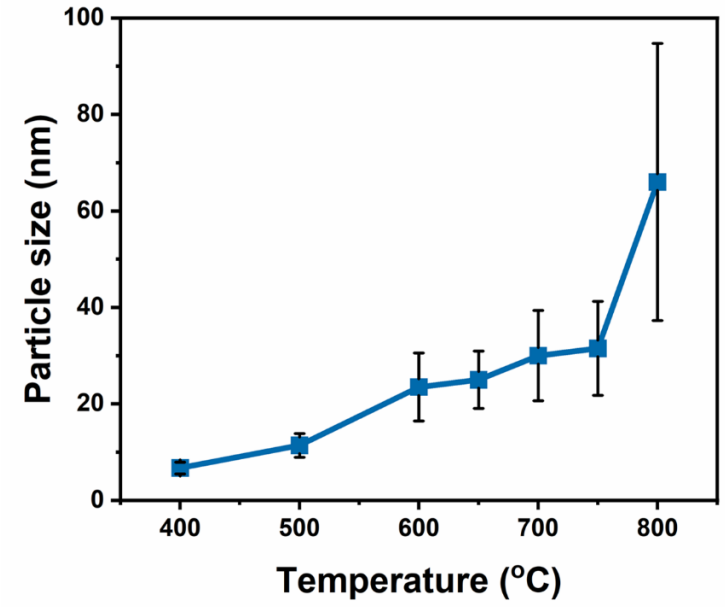

Temperature (°C)	Particle size (nm)
400	6.7 ± 1.2
500	11.4 ± 2.5
600	23.5 ± 7
650	25 ± 6
700	30 ± 9.4
750	31.5 ± 9.7
800	66 ± 28.7

Figure 2.8 Particle size vs temperature plot of Ni-PAN fibers annealed in 5%H_2; 95%N_2.

2.4.3 Microstructural analysis

To observe the microstructural features of the Ni at each temperature step, TEM and HRTEM was conducted on each sample. TEM of annealed Ni-PAN nanofibers at 300 °C (Figure 2.9 A) shows no visible particles throughout the fiber. However, upon closer observation, SAED reveals a diffused ring of Ni (111) and Ni (220) indicating amorphous or nanocrystalline domains. Bright field HRTEM again does not show any visible nanoparticles (Figure 2.9 B). However, darkfield (Figure 2.9 C) exposes sub-nanometer of <1 nm in size particles showing nucleation has occurred at this temperature and particles are distributed evenly throughout the fiber.

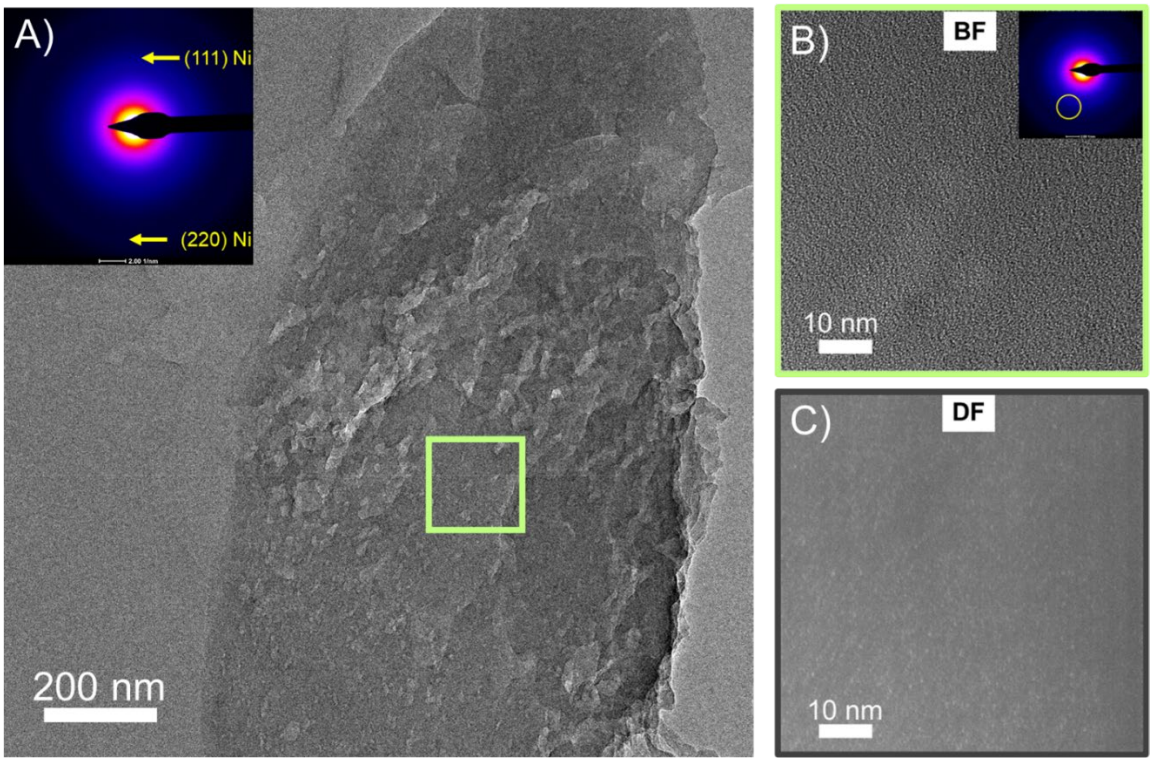

Figure 2.9 TEM of Ni-PAN nanofibers annealed at 300 °C 3 h in 5%H_2; 95%N_2 A) TEM of longitudinal section of Ni-PAN with SAED inset B) HRTEM of annealed Ni-PAN at 300 °C 3 h in 5%H_2; 95%N_2 C) Darkfield of the BF micrograph in B.

TEM of the 400 ºC annealed sample is shown in Figure 2.10. Black spots are observed in a microtomed cross-section shown in Figure 2.10 A. SAED shows diffused rings suggesting nanocrystalline domains (Figure 2.10 B). Darkfield confirms that these spots are nickel nanoparticles (Figure 2.10 C). When the annealing temperature is increased to 400 °C, the nucleated particles have grown from a sub-nanometer size to average 6.7 ± 1.2 nm. The growth from sub-nanometer to 6.7 nm suggests that there are diffusion pathways within the PAN for the metal to diffuse and the nickel metal to grow.

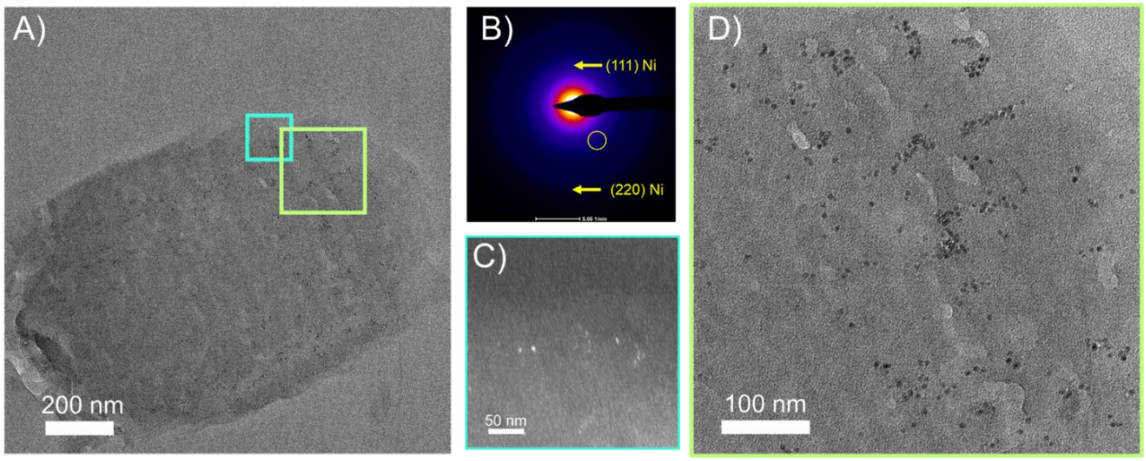

Figure 2.10 TEM of Ni-PAN nanofiber annealed at 400 °C in 5%H_2; 95%N_2 for 3 h A) overview BF B) SAED of overview C) darkfield of blue boxed region D) Higher magnification TEM of green boxed region.

Figure 2.11 A shows an overview a microtomed cross-section of a Ni-PAN nanofiber. The particles look evenly distributed, but the density of particles has increased. SAED shows bright spots appearing in the diffraction pattern indicating nano-crystalline domains with larger grains. HRTEM of a single nickel particle with a size of 10 nm at this temperature is seen to be single crystalline with a d-spacing of 0.2 nm corresponding to (111) nickel metal.

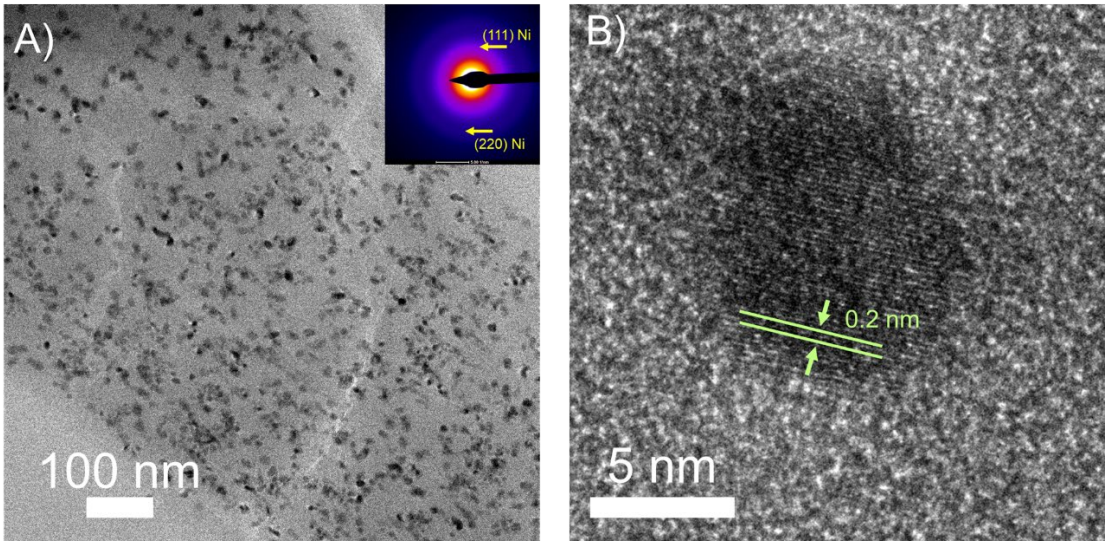

Figure 2.11 A) TEM of Ni-PAN nanofiber annealed at 500 °C in 5%H_2;95% N_2 for 3 h B) HRTEM of a single nickel nanoparticle.

When Ni-PAN is annealed at 600 °C in 5%H_2; 95%N_2 for 3 h, the average particle size of the nickel nanoparticles is 23.5 ± 7 nm. TEM of this sample shows evenly distributed nanoparticles throughout the fiber (Figure 2.12 A). Upon closer observation, porous structures are observed (Figure 2.12 B). SAED shows brighter diffractions spots including diffused Ni (111) rings. What is also seen is a diffused at ~0.34 nm d-spacing corresponding to the (002) graphite.

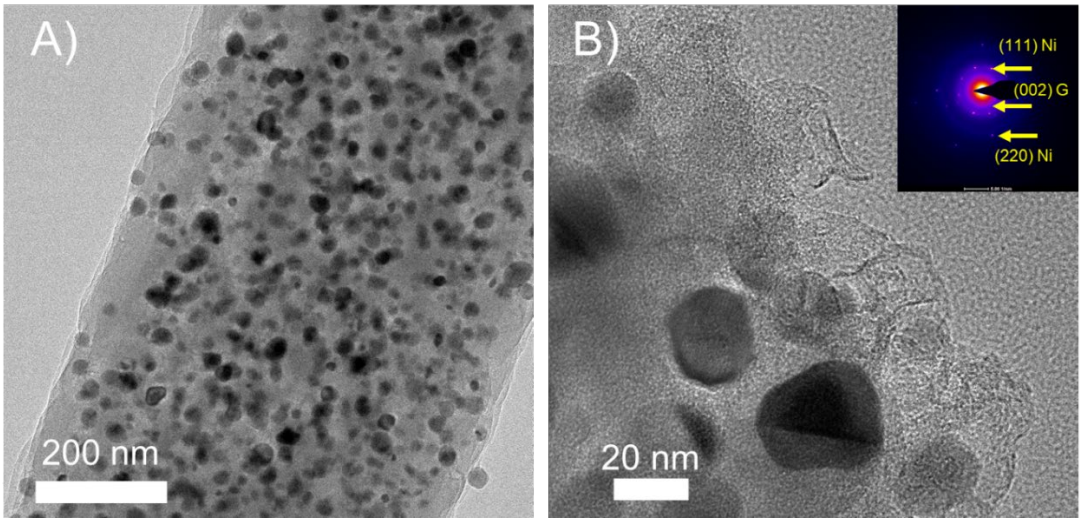

Figure 2.12 A) TEM of Ni-PAN nanofiber annealed at 600 °C in 5%H_2; N_2 for 3 h B) TEM of Ni-PAN nanofiber annealed at 600 °C in 5%H_2; N_2 for 3 h.

HRTEM shows two different nickel nanoparticles on the surface of the nanofiber ~30 nm in size (Figure 2.13 A &C). At the surface of these nickel nanoparticles, layers of ordered carbon are observed to be surrounding the particles. The d-spacing for the layered carbon is 0.36 nm. Graphite (002) peaks are typically 0.34 nm, indicating that the ordered carbon is not graphitic but a tubostratic carbon. It is at 600 °C where ordered carbon is seen under TEM.

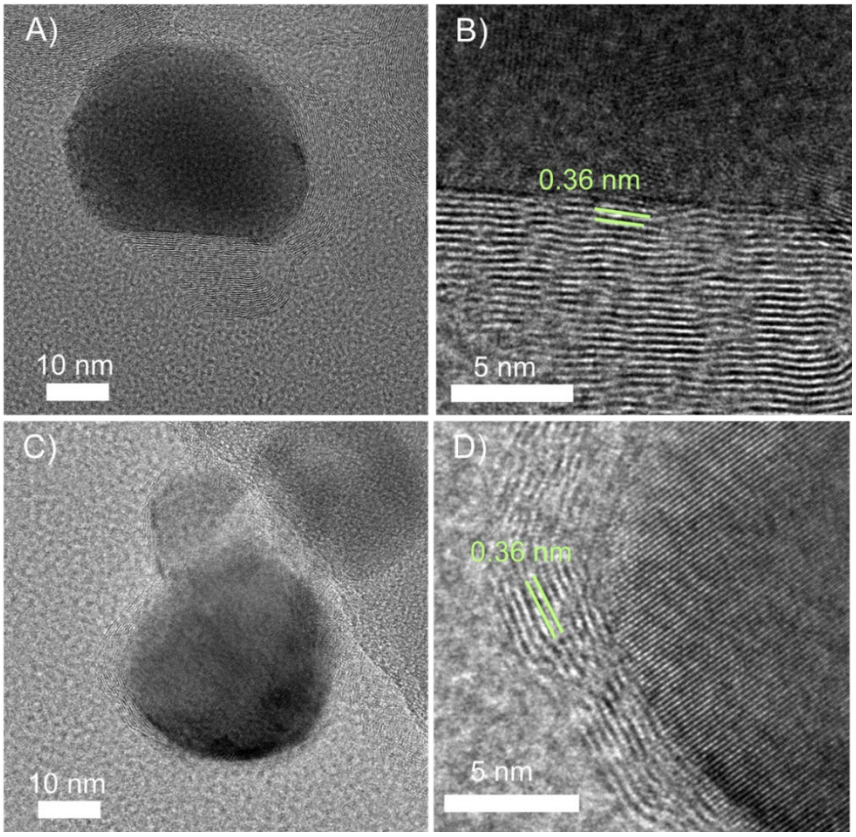

Figure 2.13 A) & C) TEM of single nickel nanoparticle in Ni-PAN nanofiber annealed at 600 °C in 5%H2; N2 for 3 h B) & D) HRTEM of nickel nanoparticle interface with crystalline carbon.

2.4.4.Growth mechanisms

During the carbonization process polyacrylonitrile nanofibers evolve gases such as H_2O, CO_2, NH_3, HCN, H_2, CO and CH_4 as cyclization, cross-linking and carbonization occurs [11]. Bromley et al. determined the gases evolved during carbonization [11]. They observed that HCN and O_2 evolves beginning at 220 °C due to the ladder formation and oxidation of the polymer. At 300 °C CO_2, H_2O, CO, and HCN is evolved. The main gas evolved at this temperature is CO_2 corresponding to the removal of -COOH in the oxidized PAN. At 400 °C higher amounts of CO_2, H_2O, CO, HCN and NH_3 are evolved due to the cross-linking of PAN. TGA was conducted on a pre-oxidized Ni-PAN sample to observe the mass loss during the carbonization when nickel is added to PAN fibers. The fibers were

put in a 150 µL alumina crucible and heated from room temperature to 800 °C at 10 °C/min in 4%H_2 ;96%Ar (Figure 2.14 A). The TGA plot shows a 5% initial mass loss at 100 °C corresponding to water loss. Because this sample was pre-oxidized no mass loss was expected below 300 °C. However, a second mass loss event initiates at 285 °C. This was correlated with the decomposition and cross-linking event of the PAN. Having nickel in the PAN fibers lowered the decomposition temperature and initiated the carbonization to 285 ºC. HCN evolution was detected for the Ni-PAN system (Figure 2.14 B). HCN starts evolving from the Ni-PAN at 285 °C indicating that HCN evolves due to the decomposition of polyacrylonitrile and confirms the start of the carbonization process of the polymer. It is important to note that sub-nanometer nickel particles are observed at 300 °C suggesting that nickel begins to nucleate and grow around the same temperature that the carbonization process is initiated. The reduction in the carbonization temperature when nickel is present suggests that the nickel is interacting with the polymer via its nitrile group. A metal-nitrile bond can occur and create a metal-nitrogen resonance structure where the metal can weaken the C≡N with a π-back donation [12].

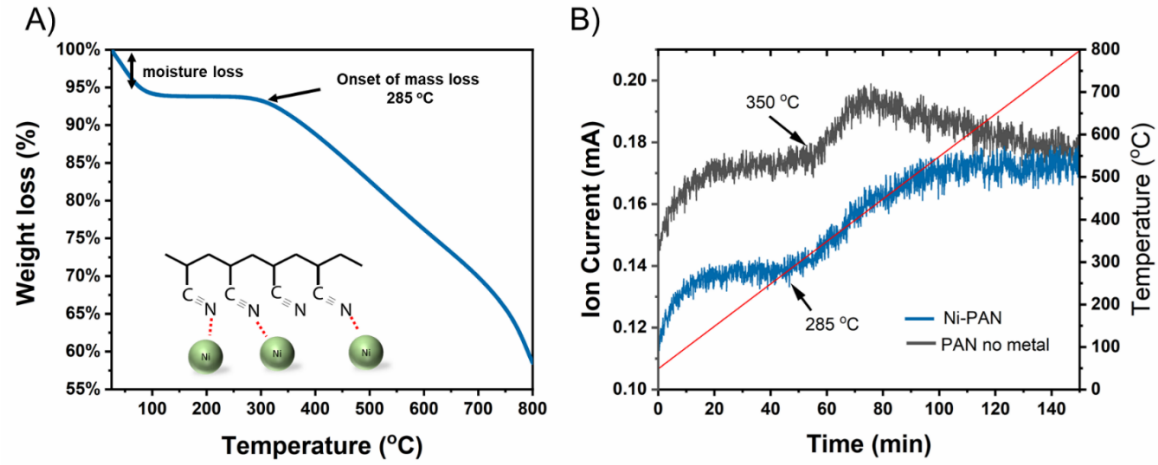

Figure 2.14 A) TGA of pre-stabilized Ni-PAN nanofibers heat treated from 25 °C to 800 °C in 4%H_2;96%Ar B) TG-MS of pre-stabilized Ni-PAN vs PAN no metal nanofibers heat treated from 25 °C to 800 °C.

The activation energy for particle size growth can be calculated by using the Arrhenius equation [13] [14] shown below where D is the particle size, R is the universal gas constant, T is the reaction temperature E_a is the activation energy and A is the pre-exponential factor.

$$D = Ae^{-\frac{E_a}{RT}}$$

Plotting the ln (D) vs 1/T, the activation energy E_a can be calculated by the slope of the plot (Figure 2.15). Two activation energies were calculated from two slopes, 46.7 kJ/mol and 103.8 kJ/mol. The lower activation energy corresponds to a classical crystallization mechanism of surface diffusion occurring at 300 °C – 600 °C. There is a slowdown of particle growth between 600 °C and 700 °C. From 700 °C – 800 °C the activation energy of 103.81 kJ/mol is attributed to coalescence.

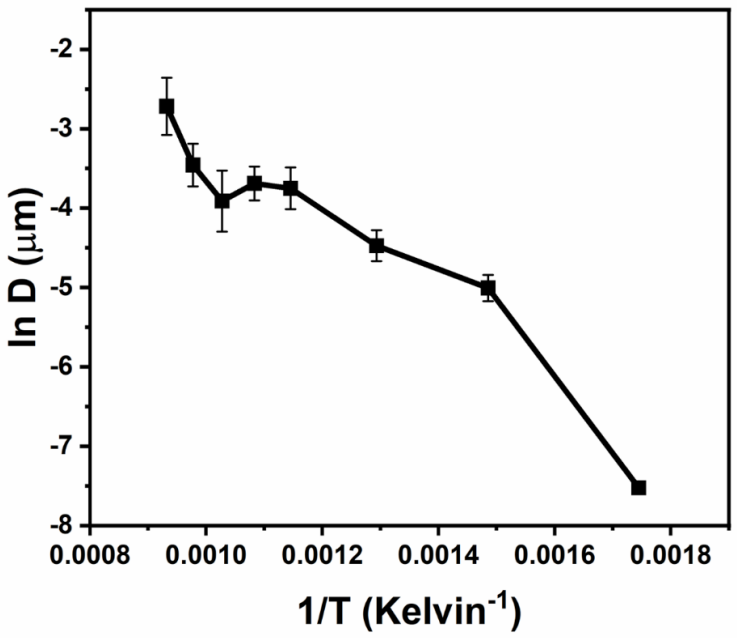

Figure 2.15 ln D vs 1/T plot of annealed Ni-PAN nanofibers at 300 °C to 800 °C for 3 h in 5%H_2; 95% N_2.

When Ni-PAN nanofibers are annealed at temperatures above 600 °C, peanut shaped nanoparticles are observed (Figure 2.16). This strongly suggests that the peanut-shaped particles are two nanoparticles merging via a process called coalescence. Coalescence occurs when two particles interact and to reduce surface energy, atoms diffuse to the points of contact permitting the particles to be bonded together and eventually causing the two particles to become one. The large increase in particle size can be evidence of coalescence as particles merge together into a much larger particle [15].

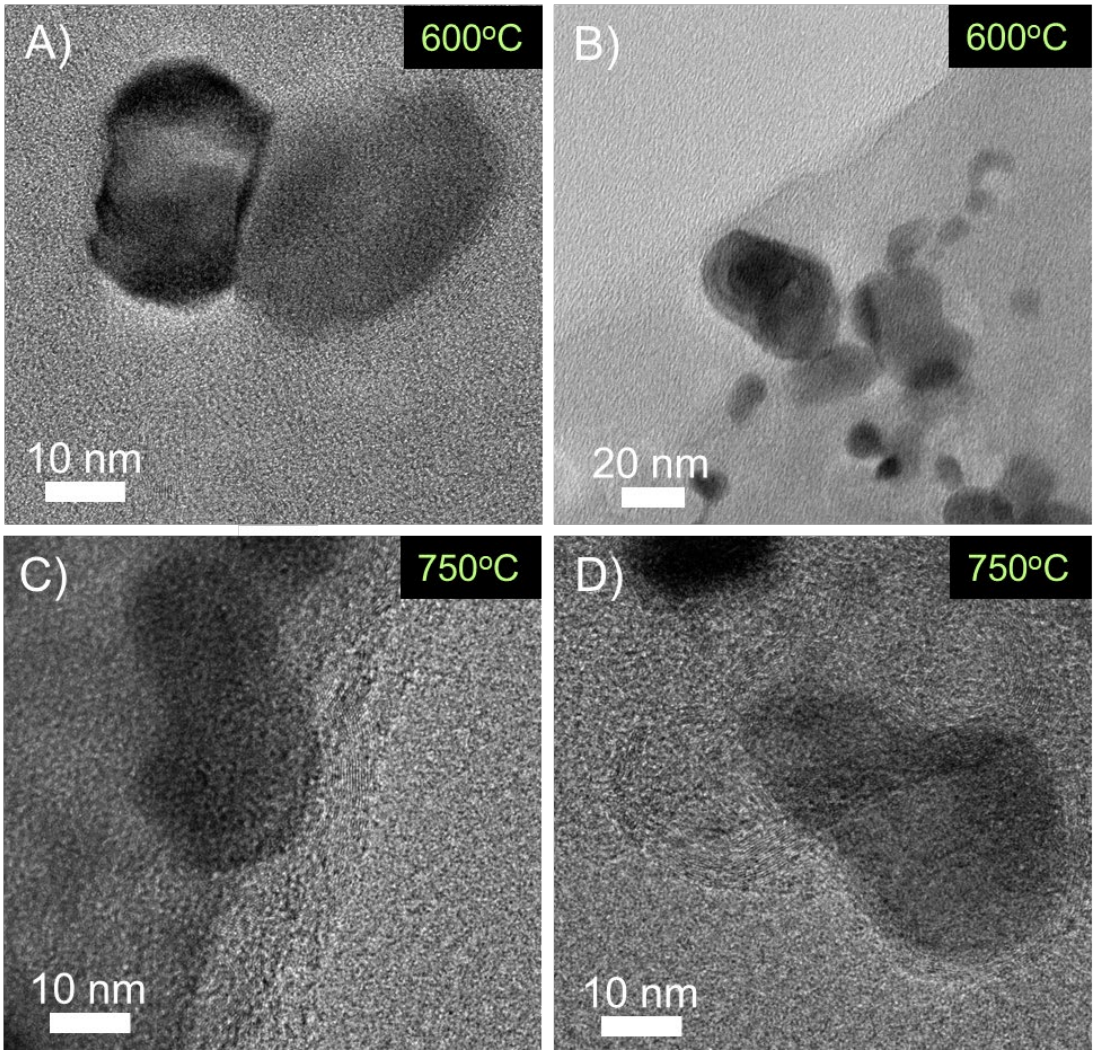

Figure 2.16 TEM of nickel nanoparticles coalescing at 600 °C and 750 °C.

2.5 Conclusions

Our studies reveal several particle growth mechanisms of nickel metal when embedded in a polymer matrix. The physical confinement of the nickel metal within a polymer matrix limits their diffusion and slows down its crystal and particle growth when compared to sample that have no polymer. Sub-nanometer nanoparticles were observed at 300 °C. TGA coupled with TG-MS revealed that the initial nucleation and crystal growth of nickel metal is closely related to the decomposition of and onset temperature of carbonization of the

polymer whereby HCN evolves suggesting a metal-polymer interaction via its nitrile group. Nickel particles continue to steadily grow until 600 °C where crystalline carbon encapsulating the surface of the metal nanoparticles are observed. Using the Arrhenius equation allowed for the calculation of the activation energy. It was revealed that two particle growth mechanisms are occurring in this study, starting with surface diffusion and then coalescence of the particles at temperature above 600 °C. Understanding the growth mechanisms of this polymer-carbon-metal nanofiber system can provide insight on how to control the size of these particles for a tailored synthesis for the desired application.

References

[1] H. Zhang and P. K. Shen, "Recent Development of Polymer Electrolyte Membranes for Fuel Cells," *Chemical Reviews,* vol. 112, no. 5, pp. 2780-2832, 2012.

[2] E. Alonso, F. R. Field and R. E. Kirchain, "Platinum Availability for Future Automotive Technologies," *Environmental Science and Technology,* vol. 46, no. 23, pp. 12986-12993, 2012.

[3] Z. Chen, D. Higgins, A. Yu, L. Zhang and J. Zhang, "A review on non-precious metal electrocatalysts for PEM fuel cells," *Energy and Environmental,* vol. 4, pp. 3167-3192, 2011.

[4] P. Trogadas, T. F. Fuller and P. Strasser, "Carbon as catalyst and support for electrochemical energy conversion," *Carbon,* vol. 75, pp. 5-42, 2014.

[5] S. L. Candelaria, Y. Shao, W. Zhou, X. Li, J. Xiao, J.-G. Zhang, Y. Wang, J. Liu, J. Li and G. Cao, "Nanostructured carbon for energy storage and conversion," *Nano Energy,* vol. 1, no. 2, pp. 195-220, 2012.

[6] C. J. Murphy, T. K. Sau, A. M. Gole, C. J. Orendoff, J. Gao, L. Gou, S. E. Hunyadi and T. Li, "Anisotropic Metal Nanoparticles: Synthesis, Assembly, and Optical Applications," *Journal of Physcial Chemistry B,* vol. 109, no. 29, pp. 13857-13870, 2005.

[7] H. Cui, G. Eres, J. Howe, A. Puretkzy, M. Varela, D. Geohegan and D. Lowndes, "Growth behavior of carbon nanotubes on multilayered metal catalyst film in chemical vapor deposition," *Chemical Physics Letters,* vol. 374, no. 3-4, pp. 222-228, 2003.

[8] H. Wu, L. Hu, M. W. Rowell, D. Kong and J. J. Cha, "Electrospun Metal Nanofiber Webs as High-Performance Transparent Electrode," *Nano Letters,* vol. 10, no. 10, pp. 4242-4248, 2010.

[9] R. Ostermann, J. Cravillon, C. Weidmann, M. Wiebcke and B. M. Smarsly, "Metal–organic framework nanofibers via electrospinning," *Chemical Communications,* vol. 47, pp. 442-444, 2010.

[10] M. Tahir, N. Mahmood, J. Zhu, A. Mahmood, F. K. Butt, S. Rizwan, I. Aslam, M. Tanveer, F. Idrees, I. Shakir, C. Cao and Y. Hou, "One Dimensional Graphitic

Carbon Nitrides as Effective Metal-Free Oxygen Reduction Catalysts," *Scientific Reports,* vol. 5, p. 12389, 2015.

[11] P. Morgan, Carbon Fibers and Their Composites, Boca Raton: CRC Press, 2005.

[12] G. Bresciani, L. Biancalana, G. Pampaloni, S. Zacchini, G. Ciancaleoni and F. Marchetti, "A Comprehensive Analysis of the Metal-Nitrile Bonding in an Organo-Diiron System," *Molecules,* vol. 26, p. 7088, 2021.

[13] S. Chen and Y. Wu, "Influence of temperature on the spark plasma sintering of calcium fluoride ceramics," *Journal of Materials Research,* vol. 29, no. 19, pp. 2297-2302, 2014.

[14] R. Hassan, J. Hassan, M. Hashim, S. Paiman and R. S. Azis, "Morphology and dielectric properties of single sample Ni0.5Zn0.5Fe2O4 nanoparticles prepared via mechanical alloying," *Journal of Advanced Ceramics,* vol. 3, pp. 306-316, 2014.

[15] A. Kocjan, M. Logar and Z. Shen, "The agglomeration, coalescence and sliding of nanoparticles, leading to the rapid sintering of zirconia nanoceramics," *Scientific Reports,* vol. 7, p. 2541, 2017.

Chapter 3 Mechanisms of graphitization in a Ni-polymer/carbon matrix

3.1 Background

Carbon nanofibers (CNF) have been used in applications such as sports equipment, and the aerospace industry [1].Carbon fiber (CF) has high tensile strength, large length to diameter ratio, high specific surface area, and high thermal and electrical conductivity [1]. The electrospinning method provides a method to produce homogenous fibers at the nanoscale [1]. CF is made from polyacrylonitrile (PAN) polymer precursor due to its high carbon content. The typical heat treatment process involves stabilization, carbonization, and graphitization. The stabilization process occurs in air at temperatures ranging from 250 °C- 275 °C which promotes the cyclization process and prevents the polymer to degrade when heated at elevated temperature. The carbonization and subsequent graphitization process occurs in an inert atmosphere from temperatures of 500 °C to 3000 °C. The graphitization process occurs at elevated temperatures of 2000 °C-3000 °C. Transition metals such as Ni, Co, and Fe are known catalysts for graphitization at lower temperatures to produce carbon nanotubes (CNTs). They are synthesized via chemical vapor deposition by the catalytic decomposition of hydrocarbons on the surface of these transition metals catalysts [2]. This synthesis usually occurs at temperatures ranging from 550 °C and 1000 °C [2].

In the case for 1D nanofibers, metal salts are mixed with a polymer, electrospun, and heat treated at elevated temperatures to form graphitic carbon. When metals are incorporated in PAN-nanofibers, carbon onion-rings are observed. To make graphitic carbon nanofibers at lower temperatures, metals need to be incorporated into the nanofiber

structure. The mechanisms for CNT synthesis have been studied extensively however, the mechanism of carbonization and graphitization when metal is incorporated in PAN-nanofibers has yet to be studied.

3.2 Objectives and hypotheses

Our objective for this work is to understand the mechanism for carbonization and graphitization in this system. By conducting temperature and time studies we can understand when carbonization and graphitization occurs and how the nickel metal is catalyzing this process. If we can identify the mechanism of graphitization, we can control the processing parameters that control this process for a more efficient synthesis of this material. Based on the information we acquire on this mechanism we can tailor our material to fit the application needs.

3.3 Materials and Methods

3.3.1 Materials

All chemicals and reagents were used as received. Nickel (II) acetate tetrahydrate (98%), anhydrous acetic acid, PAN (molecular weight (MW) ≈130 000), and DMF (99%) were all purchased from Sigma-Aldrich. Compressed air, ultrapure Argon, and 5% H_2/95% N_2, were supplied by Airgas.

3.3.2 Material synthesis

Solution prep and electrospinning

To synthesize Ni-PAN nanofibers, 1.2 g of Polyacrylonitrile and 0.25 g of $Ni(OAc)_2 \cdot 4 H_2O$ were dispersed into 8.8.g of DMF solution in a 20 mL vial followed by stirring at 500rpm for 6h at 80°C with subsequent stirring for 12h at room temperature. The solution

was then transferred into a 10 mL plastic syringe with a stainless-steel needle tip and electrospun using an eS-robot electrospinning/spray system (NanoNC, Seoul South Korea). Flow rate of 1.0 mL min^{-1} was used, and a voltage of 15 kV (10, -5 kV) was generated by a power supply (Hi-2000, Korea Electric Testing Institute) and was applied between the needle tip and a rolling aluminum foil collector (~1500 rpm) at 20 cm distance. The electrospinning process was performed at room temperature for 2h. As-spun nanofibers were dried in air for 24 h at room temperature before further processing and characterization.

Heat treatment of nanofibers for Carbon Fiber synthesis

The dried fibers were placed in an alumina crucible and put into a tube furnace (Thermo-fisher) for a two-step heating process. The fibers were first stabilized in air at 250 °C for 4h with a heating rate of 2 °C/min. The gas was immediately switched to 5%H_2; 95%N_2 and heated up to 800 °C for varying temperatures and times at a rate of 5 °C/min.

3.3.3 Material Characterization

Transmission Electron Microscopy (TEM) Morphological features and crystallinity of samples were observed using TEM (Titan Thermi-300kC, FEI) bright field imaging. TEM samples were prepared by dispersing fibrous samples in DI water, sonicating for 10 minutes, and depositing them onto ultrathin carbon films on holy carbon supports with a 400-mesh copper grid (Ted Pella, Redding CA) using a 1 mL pipette. To get cross sectional TEM micrographs of nanofibers, samples were embedded in epoxy resin (Max 1618, Polymer Composites, USA) and placed in silicone molds at room temperature overnight. 70 nm cross-sections were obtained using an ultramicrotome (RMC MT-X, Boeckeler

Instruments, CFAMM UCR) and a diamond knife (PELCO, Ted Pella). The acquired cross-sections were then placed onto a carbon-coated copper TEM grid for further imaging.

(XRD) Phase Identification was determined by XRD (PANalytical Empyrean Series 2) using Cu Kα radiation. The sample was ground up using a mortar and pestle and placed on a zero background Silicon wafer and onto the sample holder. Crystallite size was calculated from calculating the full width half maximum (FWHM) of the X-ray diffraction profiles and using the Scherrer equation where K is the Scherrer constant, λ is the wavelength of light used for the diffraction, β is the FWHM and θ is the angle measured.

(TGA) Thermogravimetric analysis (TGA) was performed on a Mettler-Toledo TGA/DSC 3+ following the same oxidation and annealing procedures at a heating rate of 10 ^{o}C/min but using 50 mL/min of 4% H_2/ Argon to decrease risk of damage to platinum elements in the instrument.

(TGA-MS) Thermogravimetric analysis with a mass spectrometer attachment was performed on a TA Discovery TGA-MS from 25 °C to 800 °C in 5%H_2; 95%N_2.

(Raman) Raman spectra was recorded with Horiba LabRam/AIST-NT with a research grade Leica DMLM microscope (532 nm laser with power of 60mW).

(FTIR) Fourier-transform infrared spectroscopy (FTIR spectroscopy) was performed using an Agilent Cary 620 FTIR Microscope. Samples were scanned from 500 – 4000 cm^{-1} with 128 scans. Spectra were processed using Resolutions Pro FTIR Software and OribginLab.

3.4 Results and discussion

3.4.1 Characterization of nanofibers

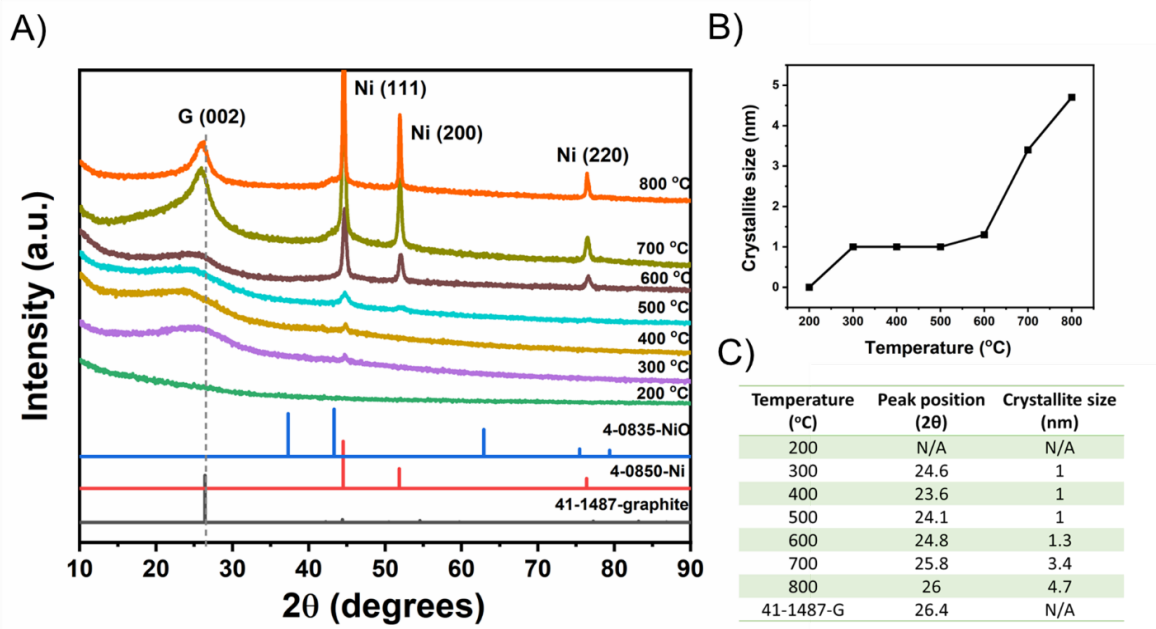

Temperature (°C)	Peak position (2θ)	Crystallite size (nm)
200	N/A	N/A
300	24.6	1
400	23.6	1
500	24.1	1
600	24.8	1.3
700	25.8	3.4
800	26	4.7
41-1487-G	26.4	N/A

Figure 3.1 A) XRD plot of annealed Ni-PAN nanofibers from 200 °C –800 °C 5%H_2;95%N_2 B) crystallite size vs temperature plot C) table of crystallite size and 2θ peak position.

As mentioned in chapter 2, when PAN mixed with nickel metal precursor is annealed at 800 °C using the carbon fiber processing technique, nickel metal nucleates and grows within the nanofiber. In addition, a carbon peak is observed at a 2θ at 26 degrees and a crystallite size of 4.7 nm (Figure 3.1). To observe the growth of the crystalline carbon, Ni-PAN samples were annealed at varying temperatures from 200 °C to 800 °C for 3 h in 5%H_2;95%N_2. Figure 3.1 A shows XRD plot of these annealed temperatures. At 200 °C, no nickel metal is detected, and no carbon peak is observed. At 300 °C a small nickel peak is observed and was confirmed that nickel metal sub-nanometer particles are present (see chapter 2). A peak at 24.6 degrees is identified with a crystallite size of ~1 nm. The crystallite size of this peak continues to be 1 nm until 600 °C where the crystallite grows

slightly to 1.3 nm. At 700 °C the 2θ peak shifts to a higher value of 25.8 degrees indicating a smaller d-spacing and the crystallite size more than doubles to 3.4 nm. At 800 °C the crystallite size continues to grow to 4.7 nm. These peaks were identified to be a crystalline carbon emerging with the carbonization of the polyacrylonitrile.

A)

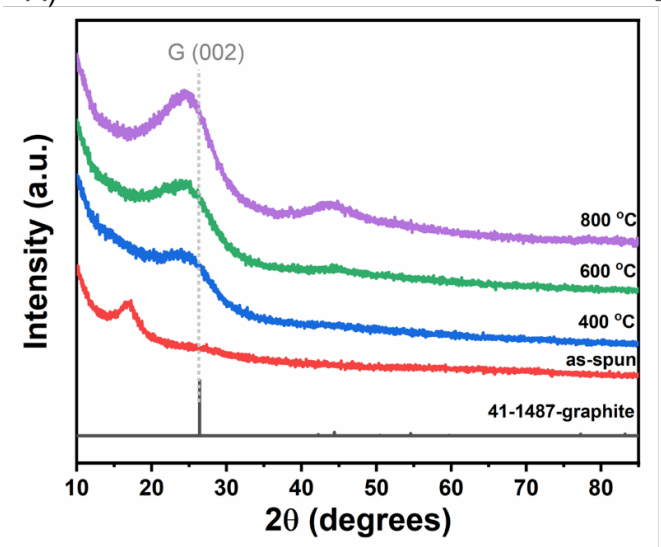

B)

Temperature (°C)	Peak position (2θ)	Crystallite size (nm)
As-spun	16.9	3.5
400	24.4	1
600	24.6	1.2
800	24.5	1.2
41-1487-G	26.4	N/A

Figure 3.2 A) XRD of electrospun PAN nanofibers with no metal annealed at varying temperatures B) Table of crystallite size and 2θ peak position.

When no metal is present, polyacrylonitrile goes through a carbonization process from 300 °C- 800 °C. This includes the removal of no carbon constituents as evolved gas while the carbonization is taking place. Some crystallinity is observed with XRD when PAN is annealed from 400 °C to 800 °C (Figure 3.2 A). As-spun PAN nanofibers have an inherent crystallinity before any heat treatment due to the chemical structure of the polymer. A peak at 16.9 degrees 2θ with a crystallite size of 3.5 nm is observed. As the PAN nanofibers are annealed at elevating temperatures a peak appears at 24.6 degrees 2θ corresponding to an amorphous nanocrystalline carbon. Comparing it to graphite reference,

this ordered carbon is not graphitized. The crystallite sizes are summarized in Figure 3.2 B. This indicates that the presence of the metal within the PAN fiber catalyzes the graphitization process as graphitic peaks are observed at 800 ºC.

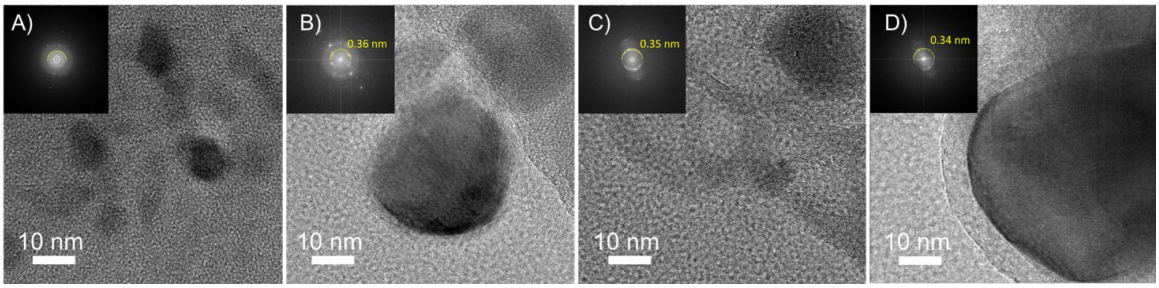

Figure 3.3 HRTEM of Ni-PAN nanofiber surface annealed for 3 h in 5%H_2; 95%N_2 at A) 500 °C B) 600 °C C) 700 °C D) 800 °C.

Figure 3.3 shows the carbonization progression of Ni-PAN samples annealed at 500 °C to 800 °C for 3 hours. At 500 °C no visual confirmation of ordered carbon is observed. FFT shows a very diffused ring at ~0.36 nm indicating an amorphous structure. At 600 °C 10 layers of ordered carbon is seen surrounding a nickel nanoparticle (Figure 3.3 B). The d-spacing of this layered carbon is 0.36 nm. As the annealing temperature is increased to 700 °C, (Figure 3.3 C) the layers range from 10-20 layers of ordered carbon with a d-spacing of 0.35. However, the layered carbon is not surrounding the nickel nanoparticle. At 800 °C (Figure 3.3 D) ~20 layers of ordered carbon are observed surrounding a large 95 nm particle, indicating that the carbon layers cap at 20 layers. The d-spacing is 0.34 nm, corresponding to (002) graphitic structure indicating that at 800 °C the carbon has transformed into graphitic carbon.

3.4.2 Microstructural analysis

The structural characteristics of the crystalline carbon was acquired using TEM at each annealed temperature. HRTEM of Ni-PAN nanofibers annealed at 600 °C shows layers of

ordering surrounding a nickel nanoparticle. As mentioned earlier, the d-spacing at this temperature is 0.36 nm, corresponding to turbostratic carbon or a “graphite-like” structure that is not fully graphitized. Upon close observation, the layered structure shows gaps in between the layers structure which is indicative of edge dislocations. Figure 3.4 C shows crystalline carbon without any nickel particle surrounding it, but an equivalent size nanoparticle on the right side suggesting the nickel nanoparticle moved or dislodged itself from the surrounding carbon. At 700 °C 3 h (Figure 3.4 D), the edge dislocations are observed as well. At 800 °C the crystalline carbon d-spacing decreases to 0.34 nm corresponding to a more graphitic structure. As the annealing temperature increases, the d-spacing decreases from 0.36 nm to 0.34 nm showing the graphitization with increasing temperature.

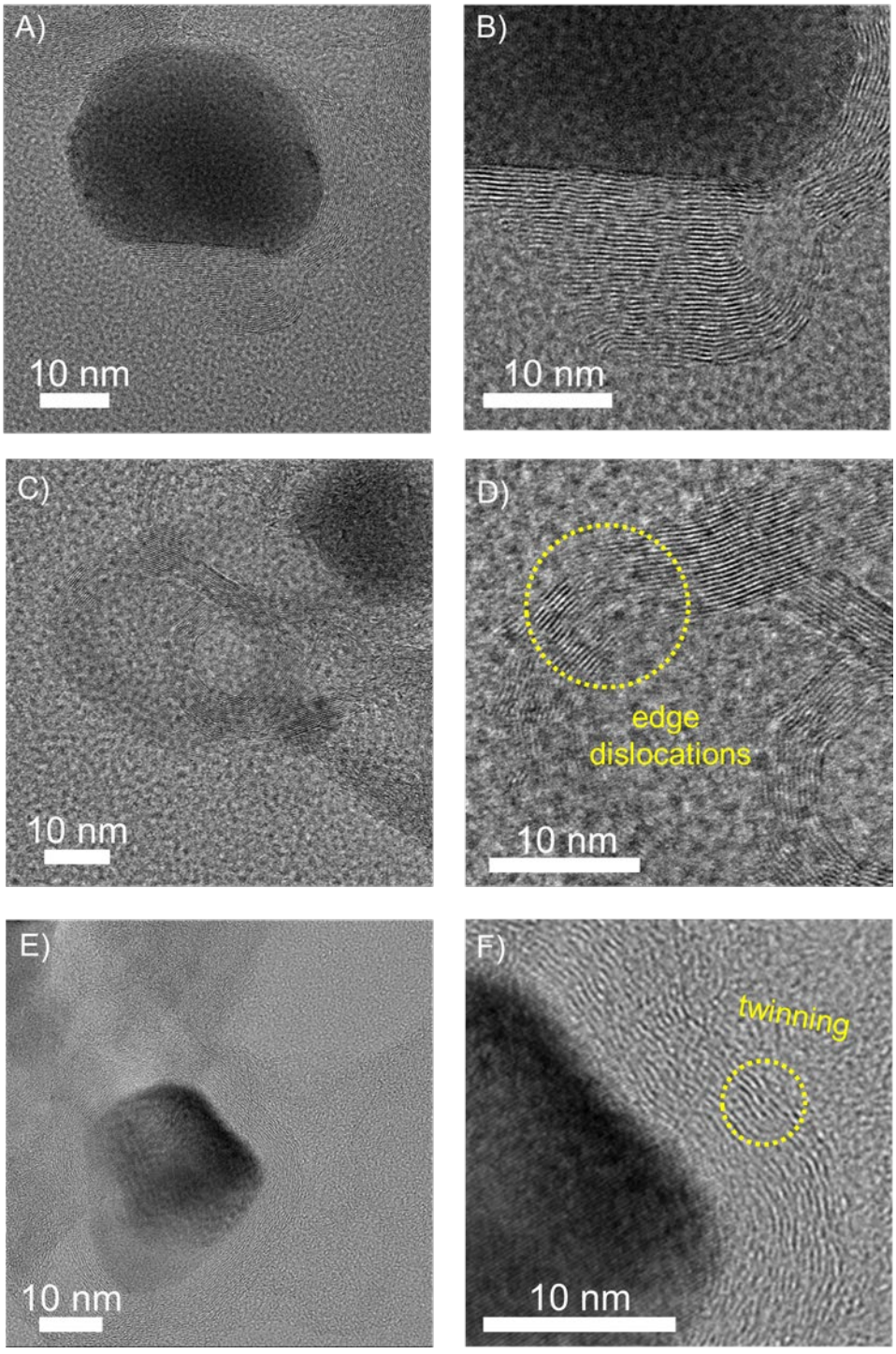

Figure 3.4 TEM of a nickel nanoparticle in Ni-PAN nanofiber annealed at A) & B) 600 °C 3 h C) & D) 700 °C 3 h E) & F) 800 °C 3 h.

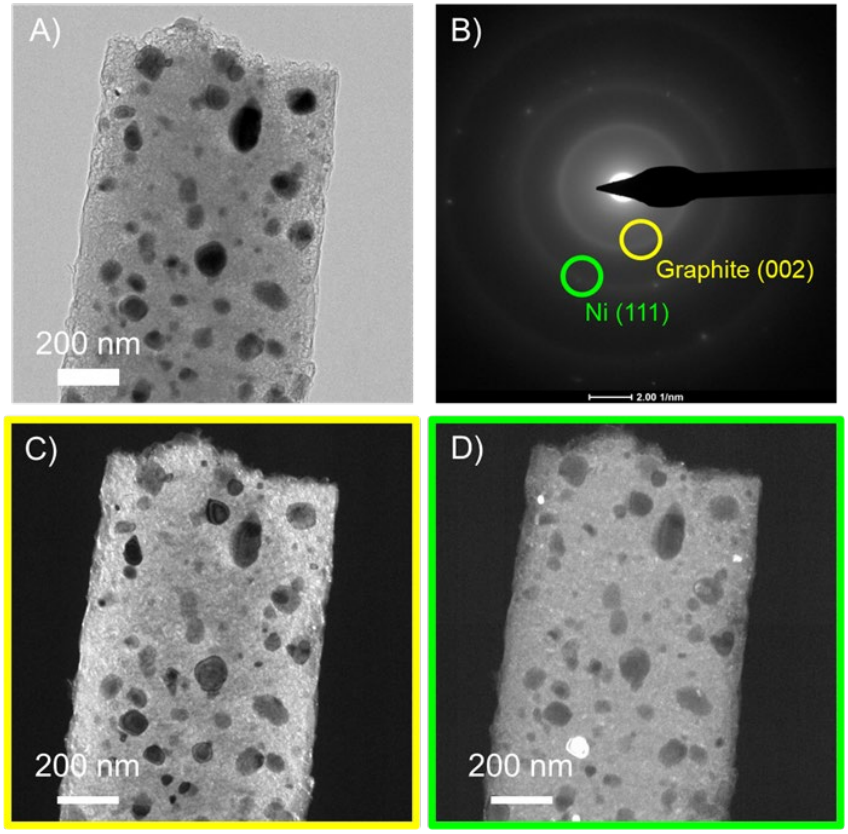

Figure 3.5 TEM of Ni-PAN nanofibers annealed at 800 °C 3h A) TEM of single nanofiber B) SAED of nanofiber C) & D) Darkfield of overview nanofiber.

Figure 3.5 shows an overview of a Ni-PAN nanofiber annealed at 800 °C and an SAED of that same area. Figure 3.5 C) &D) are dark-field micrographs of nickel and crystalline carbon areas. Dark-field exposes that crystalline carbon domains are evenly distributed throughout the fiber, not just in the regions surrounding the nickel particles.

A)

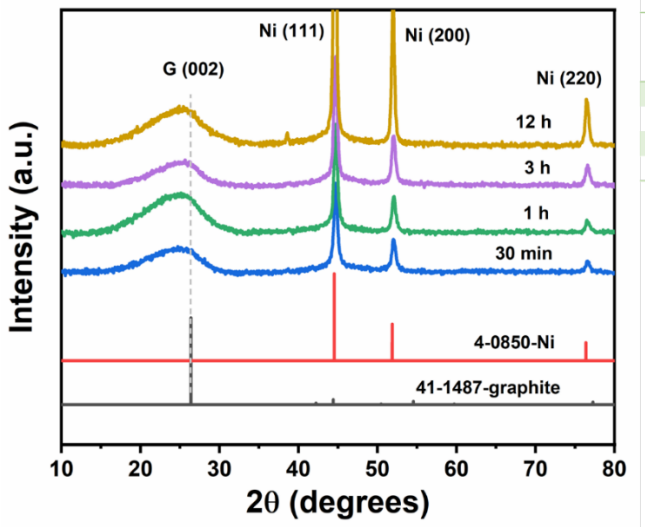

B)

Time (hours)	Peak position (2θ)	Crystallite size (nm)	Peak position (2θ)	Crystallite size (nm)
0.5	24.7	1.8	44.7	16.5
1	25	1.4	44.7	16.4
3	25	1.2	44.7	15
12	25	1.3	44.6	23

Figure 3.6 A) XRD plot of annealed Ni-PAN nanofibers at 600 °C at varying times B) table of crystallite size and peak position.

When Ni-PAN nanofibers are annealed in a reducing environment it inherently goes through a carbonization process. Without any metal PAN nanofibers have an XRD carbon peak indicating amorphous or nanocrystalline ordering. The carbon peak does not shift as annealing temperature increases even at 800 °C. However, in the presence of nickel metal, the 2θ of the carbon peak shifts to a higher degree indicating higher degree of ordering. This ordering surrounds the metal nanoparticle at 600 °C. suggesting the nickel is playing a role in the carbonization and graphitization process and lowering the graphitization temperature. Time studies were done at 600 °C to observe the progression of this carbon ordering and XRD was acquired (Figure 3.6). The carbon peak is at 24.7 degrees after 30 min of annealing at 600 °C and shifts to a higher 2θ after 1 hour of annealing to 25 degrees. After 1 hour of annealing, the carbon peak remains at the same position. The crystallite size remains in the 1 nm range throughout this time study. The nickel peaks were identified in the XRD plot. The peak position of the Ni (111) with 30 minutes to 3 hours annealing

time is 44.7 degrees, a slight shift from the reference nickel peak of 44.5 degrees. At 12 hours annealing time, the Ni (111) peak shifts to 44.6 degrees. The presence of a crystalline carbon peak at 600 °C in XRD as well as the visual confirmation seen with TEM suggested that the nickel may initiate the graphitization process. It also suggested that the low graphitic content was a kinetic limitation and so a longer annealing time would produce more crystalline carbon. It was hypothesized that because carbon ordering was observed at 600 °C on the surface of the nickel, that a longer annealing time would increase the amount of crystalline carbon. However, XRD does not show a significant change to the crystallite size of the carbon peak as well as minimal change to peak intensity.

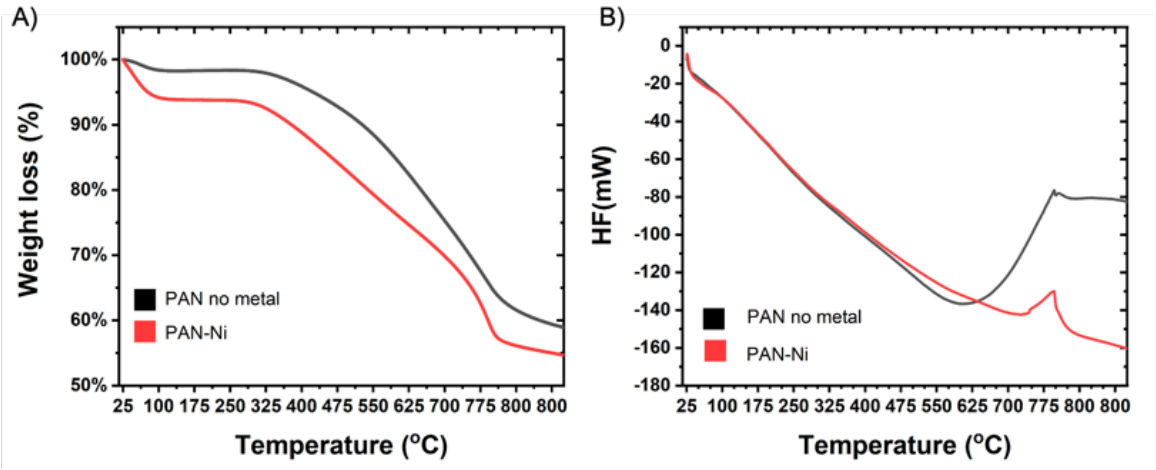

Figure 3.7 A) TGA and B) DSC of PAN and Ni-PAN nanofibers annealed in 4%H_2; 96%Ar from 25 °C – 800 °C.

We wanted to observe the mass loss events during the carbonization process. The nanofibers were oxidized in a tube furnace at 250 °C for 4 hours in air prior to the TGA studies. They were placed in a 150 µL alumina crucible. The nanofibers were heated to 800 °C in 4%H_2; 96%Ar. Figure 3.7 shows TGA/DSC plots of PAN with no metal and Ni-PAN samples. There is an initial mass loss for both the PAN no metal and PAN-Ni samples at

100 °C indicating water mass loss. The Ni-PAN samples has significantly more water loss which due to the water in the nickel acetate tetrahydrate precursor. A second mass loss event occurs at 300 °C for both samples. However, the rate of mass loss is higher in the PAN-Ni. This suggests that the presence of nickel in the system increases the rate of the polymer decomposition during the carbonization process. The graphitization process is an endothermic reaction. Comparing PAN no metal and PAN-nickel nanofibers annealed in 4%H_2;96%Ar with DSC (Figure 3.7 B) at 600 °C the endothermic peak turns exothermic for the PAN with no metal which corresponds to the decomposition of the PAN and the carbonization process. However, the PAN-nickel sample remains endothermic. This indicates a different mechanism is introduced in the system that corresponds to an endothermic process.

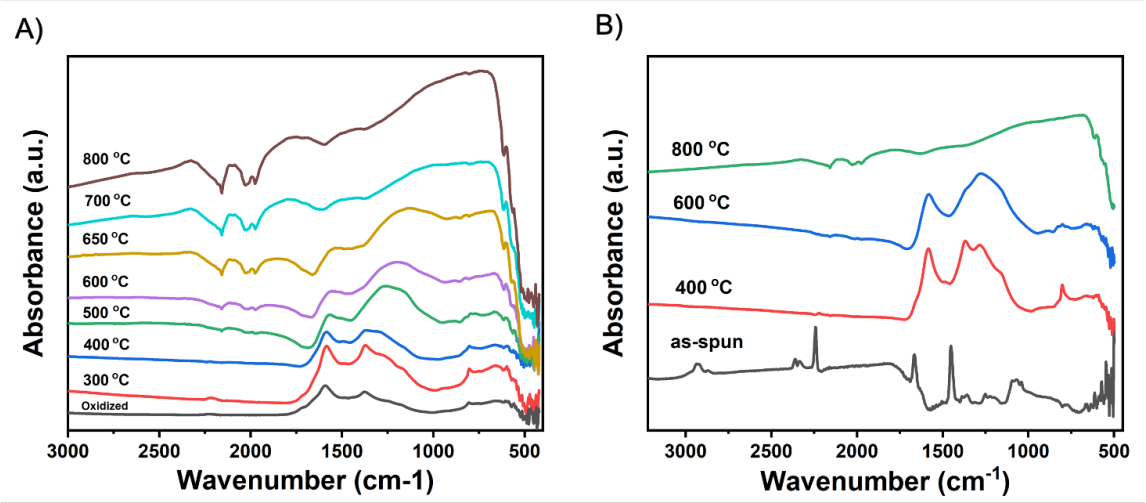

Figure 3.8 A) FTIR of annealed Ni-PAN fibers B) FTIR of annealed PAN with no metal at varying temperatures for 3 h in 5%H_2; 95%N_2.

To identify the chemical bonds during the carbonization process, FTIR was done on the nanofibers at each temperature step. As-spun nanofibers shows a distinct peak at 2242 corresponding to the C≡N bond. Other peaks at 2929 cm^{-1} and 1454 cm^{-1} correspond

to the vibration of the aliphatic CH groups (CH, CH_2, CH_3) [3]. The peak at 1667 cm^{-1} is associated with the C=O bond. After oxidation at 250 °C in air, the peak associated with the nitrile group has significantly decreased in intensity, New FTIR peaks appear located at 1591 cm^{-1}, 1376 cm^{-1}, and 804 cm^{-1}, corresponding to C=N, C=C, and C=C-H. This drastic change in FTIR peaks implies that the chemical structure of the PAN significantly changes after stabilization, which is indicative that the polymer has undergone cyclization, crosslinking, dehydrogenation, and oxidation. In the PAN no metal sample, a broad peak at ~2100 cm^{-1} is seen at 800 °C annealing temperature. A small signal is also seen at 600 °C. This broad peak is indicative of a C=C=C [4] corresponding to carbon ordering. This correlates with what we see in XRD. In the Ni-PAN system, this peak appears as low as 500 °C which suggests in the presence of Ni, the PAN begins to become a more ordered structure at lower temperature.

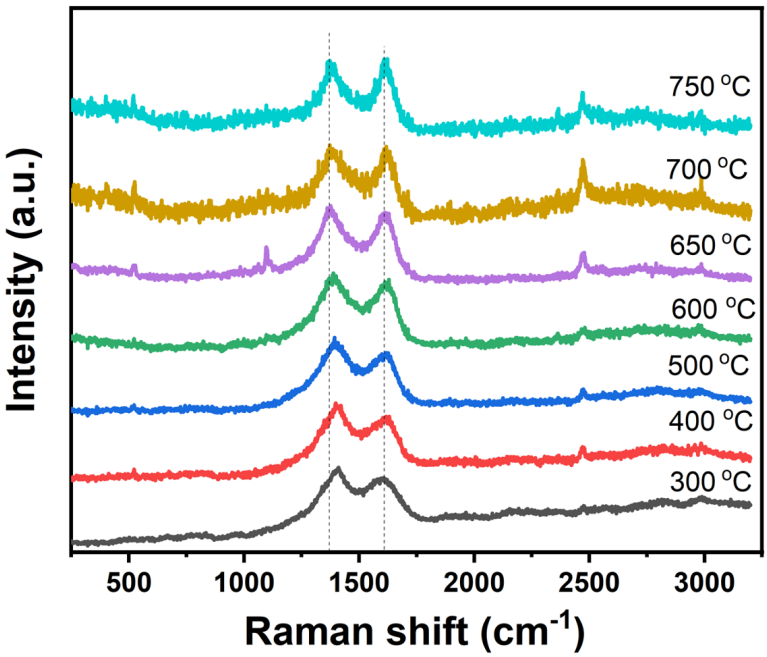

Figure 3.9 Raman of Ni-PAN nanofibers annealed at varying temperatures for 3 h in 5%H_2; 95%N_2.

To analyze the carbonaceous structural properties of this Ni-PAN system, Raman spectroscopy was done on samples heat treated at 300 °C, 400 °C, 500 °C, 600 °C, 650 °C, 700 °C, and 750 °C. There are two main bands observed at 1369 cm^{-1} and 1611 cm^{-1} corresponding to the D band and G band, respectively. The D band corresponds to the disordered turbostratic structure whereas the G band is attributed to the graphitic ordered structure. At lower temperatures, the D band is at a higher wavenumber. As temperature increases, the D band blue shifts to a lower wavenumber.

3.4.3 Growth mechanisms

The source of the carbon comes from the decomposition of the polymer during the carbonization process and believe that the nickel is acting as a catalyst for graphitization.

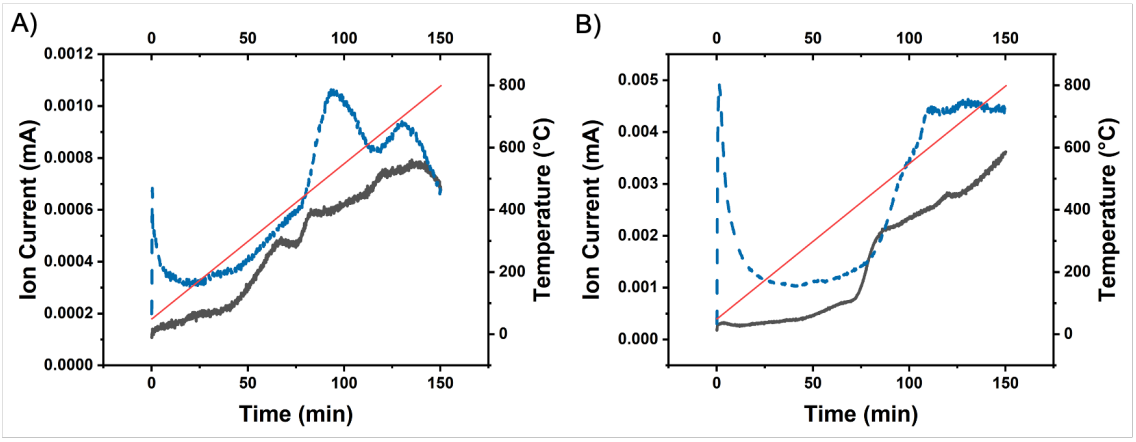

Figure 3.10 TGA-MS of annealed PAN and PAN-Nickel nanofibers in 5%H_2; 95%N_2 to 800 °C A) CH_4 ion trace for PAN vs Ni-PAN B) NH_3 ion trace for PAN vs Ni-PAN.

To analyze the gas evolution of Ni-PAN nanofibers during the carbonization process, TGA-MS was done. Looking at the TGA-MS plot (Figure 3.10 A), methane is being produced throughout the annealing process for both the PAN-no metal and PAN w/ nickel. However, at 430 °C the rate of methane production increases and peaks at 520 °C. It is hypothesized that more methane is produced in the PAN-nickel because of the metal nanoparticle de-stabilizing the PAN structure and speeding up the decomposition of PAN. This is confirmed with TGA showing a faster rate of decomposition (Figure 3.7). The decrease in methane after the 520 °C corresponds to the adsorption and dissociation on the surface of the nickel nanoparticles beginning the process of graphitization catalyzed by the metal nanoparticles. In Figure 3.10 B, the TG-MS plot of NH_3 is observed. At 500 °C the Ni-PAN sample has a higher evolution of NH_3 when compared to no metal-PAN. It is suggested that the higher evolution of NH_3 means the removal of nitrogen in the system.

Based on the evidence provided, there seems to be a different mechanism for the carbonization of polyacrylonitrile when nickel metal is present. Nickel is a known catalyst for catalytic graphitization but has not been studied in a nanofiber system.

3.5 Conclusion:

This study reveals the mechanism for graphitization at low temperatures in a Ni-PAN nanofiber system carbonized using the typical two heating step of a carbon fiber processing technique. It was shown that when nickel metal is present and is annealed along with the PAN fiber, the decomposition of the polymer evolves carbonaceous species that is used as a carbon source for a catalytic graphitization process. We believe that the carbon species adsorbs onto the surface of the metal nanoparticle, dissociates, and saturates with carbon until it spits out a turbostratic structure encapsulating the metal nanoparticle as early as 600 °C. This ordering is initiated by the decomposition of the polyacrylonitrile. However, at 600 °C the crystalline carbon is not yet graphitized but rather a turbostratic structure. As annealing temperature increases, the ordered carbon slowly graphitizes into graphitic carbon. This is important to understand to control to know at what temperature graphitization occurs so the material can be prepared at the optimized temperature and time, overall reducing time and cost of the synthesis process.

References

[1] Z. Kurban, A. Lovell, D. Jenkins, S. Bennington, I. Loader, A. Schober and N. Skipper, "Turbostratic graphite nanofibres from electrospun solutions of PAN in dimethylsulphoxide," *European Polymer Journal,* vol. 46, no. 6, pp. 1194-1202, 2010.

[2] Ç. Öncel and Y. Yürüm, "Carbon Nanotube Synthesis via the Catalytic CVD Method: A Review on the Effect of Reaction Parameters," *Fullerenes, Nanotubes and Carbon Nanostructures,* vol. 14, no. 1, pp. 17-37, 2006.

[3] S. N.Arshad, M. Naraghi and IoannisChasiotis, "Strong carbon nanofibers from electrospun polyacrylonitrile," *Carbon,* vol. 49, no. 5, pp. 1710-1719, 2011.

[4] "Millipore Sigma," 2022. [Online]. Available: https://www.sigmaaldrich.com/US/en/technical-documents/technical-article/analytical-chemistry/photometry-and-reflectometry/ir-spectrum-table. [Accessed 17 May 2022].

Chapter 4 Synthesis-structure relationships of TiO_2 nanoparticles in a polymer/carbon matrix

4.1 Background

Due to the increasing accumulation of toxic pesticides and organic dyes in water systems, there is an increasing demand for an effective water treatment process to completely degrade these pollutants. Semiconducting photocatalytic materials is a promising solution that can use adsorbed light in the presence of water and generate active radical species on the surface of the active material to oxidize organic pollutants and break them down into harmless molecules like H_2O and CO_2 (Figure 4.1).

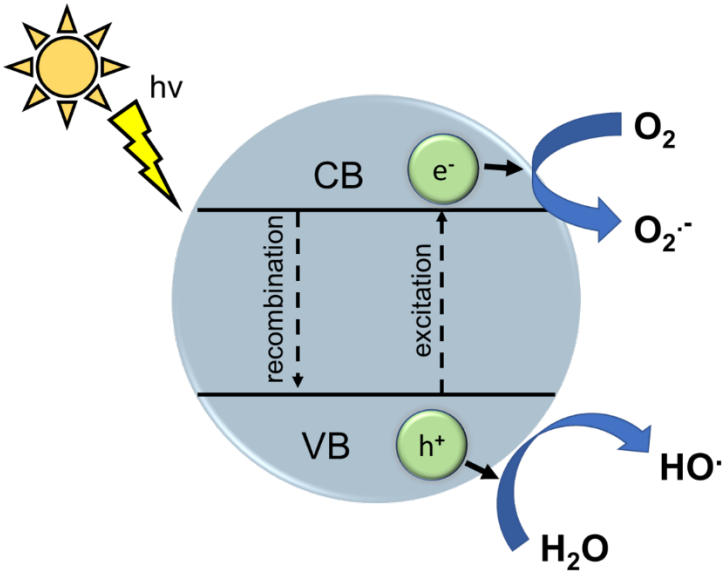

Figure 4.1 Schematic of photocatalysis mechanism where an electron-hole pair is generated, charge separation and migration are at the surface and a chemical reaction occurs on active sites.

Titanium dioxide (TiO_2), a photocatalytic material has shown to have a very strong oxidation potential that can degrade a variety of harmful pollutants found in water systems [1]. There are many factors that influence photocatalytic performance including, the size, high surface area to volume ratio, pore volume, pore structure, and crystalline phase. Thus,

development of controlled nanostructures and adjustments of these factors remains a strong focus of photocatalysis research [2]. TiO_2 has three polymorphs (Figure 4.2), two of significant engineering interest for photocatalysis are anatase and rutile [3]. Anatase exhibits higher photocatalytic activity when compared to rutile [4]. However, the phase mixture of anatase and rutile is known to have synergistic effects and an increased photocatalytic activity when compared to either pure phase [5]. This occurs when anatase and rutile are in direct interfacial contact, resulting in band alignment which leads to a favorable electron transfer from rutile to anatase that stabilizes charge separation and prevents rapid recombination [6]. Out of the two polymorphs, rutile is the thermodynamically stable phase. However, typically at lower processing temperatures, anatase forms first, then converts to rutile at temperatures between 400 °C - 1200 °C [7]. Anatase forms first due to the greater ease of formation of short-range ordered TiO_6 octahedra. Thermodynamically, the more rapid ordering of anatase could be due to lower surface energy compared to rutile and could favor anatase growth [3]. However, it should be noted that it is possible to form rutile at room temperature conditions using hydrothermal synthesis methods [8].

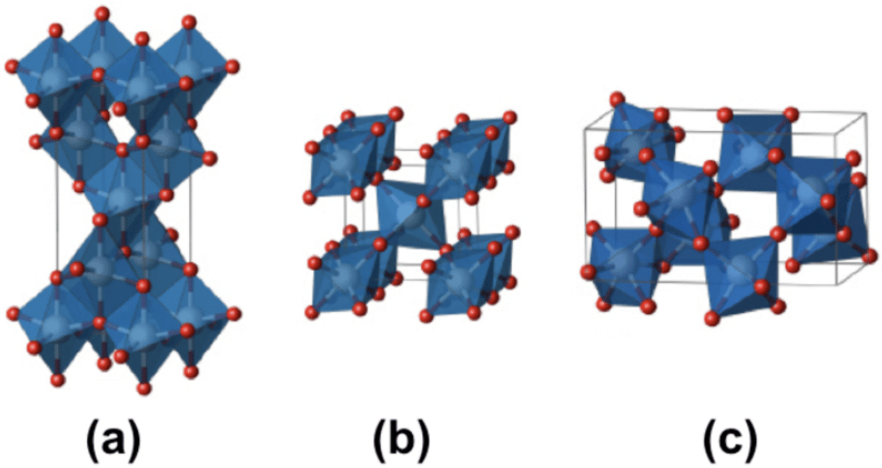

Figure 4.2 Three polymorphs of TiO_2 a) anatase b) rutile c) brookite. The small red spheres represent oxygen atoms, and the gray represent titanium atoms. The blue polyhedral structure shows the TiO_6 octahedra. Figure was taken from [9].

TiO_2 is very stable, inexpensive, and has high surface photochemical reactivity with water and oxygen but has inherent drawbacks as well [10]. When light absorbs onto the surface of the TiO_2 it causes a charge separation where it excites an electron to its conduction band leaving behind a hole in the valence band. This results in a generation of hydroxyl and oxygenated radical species [11]. These highly reactive molecules interact with organic molecules and degrade them to harmless constituents of H_2O and CO_2.

$$TiO_2 + h\nu \rightarrow e^-_{cb} + h^+_{vb}$$

$$e^-_{cb} + O_2 \rightarrow O_2^-$$

$$h^+_{vb} + H_2O \rightarrow OH^\bullet + H^+$$

However, the rate of electron-hole recombination is high in TiO_2 particles [12]. Yu [12] and Du [13] have shown that addition of electron scavenging moieties like carbon enable the reduction in electron-hole recombination. Due to its wide band gap, it requires UV light, which is only 5% of the solar spectrum. In addition, many TiO_2 photocatalytic

systems are particulate in nature, which necessitates a recollection process that hinders their efficiency, drives up cost, and limits widespread application. Researchers have investigated ways to anchor nanoparticles in a three-dimensional interconnected nanocomposite structure. Among those are TiO_2/carbon nanofiber composites fabricated by electrospinning polyvinyl-pyrrolidone (PVP) and polyacrylonitrile (PAN) precursors [14]. These nanofibers are more efficient at photodegradation than nanoparticles due to increased surface area, affording larger adsorption capacity, reduction in electron-hole recombination, and an increased amount of light available for degradation. Most studies have focused on the synthesis of these nanofibers using varied electrospinning parameters and their photodegradation efficiencies. However, the effect on particle growth and phase transformation within these nanofibers and the role of the polymer matrix towards this end have yet to be investigated. Understanding the mechanism of phase transformation within this polymer nanofiber matrix is critical to controlling the phase ratio of this system to fabricate efficient target-selective materials.

4.2 Objectives and hypotheses

The objectives of this work are to reveal mechanisms of polymer-based phase control of TiO_2 via investigation of the synthesis-structure relationships of TiO_2 nanoparticles in a polymer/carbon matrix, for developing water purifying membranes.

4.3 Materials and methods

4.3.1 Materials

All chemicals and reagents were used as received. Titanium (IV) butoxide, anhydrous acetic acid, PAN (molecular weight (MW) ≈130 000), and DMF (99%) were all purchased

from Sigma-Aldrich. Compressed air, ultrapure Argon, and 5% H2/95% N2, were supplied by Airgas.

4.3.2 Material synthesis

To synthesize TiO_2-PAN nanofibers, 0.6 g of Polyacrylonitrile was dissolved in 4.4 g of Dimethylformamide in a 20 mL vial. 100 µL of anhydrous acetic acid was added to the vial and stirred at 100 rpm at 80 °C for 12 hours. 0.34 g of Titanium (IV) butoxide was added to the vial and stirred at room temperature for 1 h at 200 rpm. The solution was then transferred into a 10 mL plastic syringe with a stainless-steel needle tip and electrospun using an eS-robot electrospinning/spray system (NanoNC, Seoul South Korea). Flow rate of 1.0 mL min-1 was used, and a voltage of 15 kV (10, -5 kV) was generated by a power supply (Hi-2000, Korea Electric Testing Institute) and was applied between the needle tip and a rolling aluminum foil collector (~1500 rpm) at 20 cm distance. The electrospinning process was performed at room temperature for 2 h. As-spun nanofibers were dried in air for 24 h at room temperature before further processing and characterization.

Heat treatment of nanofibers for Carbon Fiber synthesis

The dried fibers were placed in an alumina crucible and put into a tube furnace (Thermo-fisher) for a two-step heating process. The fibers were first stabilized in air at 275 °C for 1 h with a heating rate of 5 °C/min. The nanofibers were left to cool to room temperature and a small sample was removed for characterization. The remaining sample was placed back into the tube furnace and heat treated to 800 °C for 3 h in Argon.

Material Characterization

Scanning Electron Microscopy (SEM): Samples were mounted on aluminum mounts using carbon tape and sputter coated with Platinum/ Palladium for 30 seconds (Cressington 108 Auto, CFAMM UCR). Particle size, distribution, and morphology were observed using a Scanning Electron Microscope (Mira3, Tescan, CFAMM UCR) at 10 kV.

Transmission Electron Microscopy (TEM Morphological features and crystallinity of samples were observed using TEM (Titan Thermi-300kC, FEI) bright field imaging. TEM samples were prepared by dispersing fibrous samples in DI water, sonicating for 10 minutes, and depositing them onto ultrathin carbon films on holy carbon supports with a 400-mesh copper grid (Ted Pella, Redding CA) using a 1 mL pipette. To get cross sectional TEM micrographs of nanofibers, samples were embedded in epoxy resin (Max 1618, Polymer Composites, USA) and placed in silicone molds at room temperature overnight. 70 nm cross-sections were obtained using an ultramicrotome (RMC MT-X, Boeckeler Instruments, CFAMM UCR) and a diamond knife (PELCO, Ted Pella). The acquired cross-sections were then placed onto a carbon-coated copper TEM grid for further imaging.

(XRD) Phase Identification was determined by XRD (PANalytical Empyrean Series 2) using Cu Kα radiation. The sample was ground up using a mortar and pestle and placed on a zero background Silicon wafer and onto the sample holder. Crystallite size was calculated from calculating the full width half maximum (FWHM) of the X-ray diffraction profiles and using the Scherrer equation where K is the Scherrer constant, λ is the wavelength of light used for the diffraction, β is the FWHM and θ is the angle measured.

(TGA) Thermogravimetric analysis (TGA) was performed on a Mettler-Toledo TGA/DSC 3+ following the same oxidation and annealing procedures at a heating rate of 10 °C/min but using 50 mL/min of 4% H_2/ Argon to decrease risk of damage to platinum elements in the instrument.

(FTIR) Fourier-transform infrared spectroscopy (FTIR spectroscopy) was performed using an Agilent Cary 620 FTIR Microscope. Samples were scanned from 500 – 4000 cm^{-1} with 128 scans. Spectra were processed using Resolutions Pro FTIR Software and OriginLab.

4.4 Results and discussion

4.4.1 Characterization of PAN/TiO_2 nanofibers

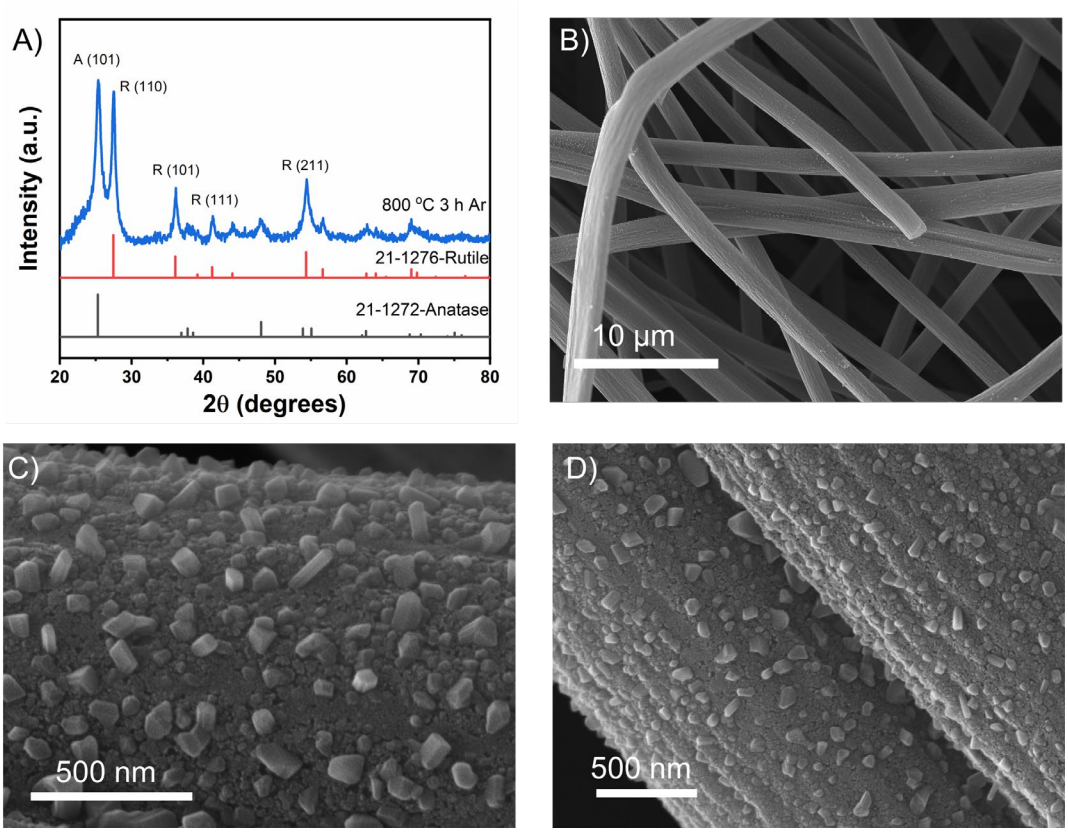

Figure 4.3 A) XRD of TiO2-PAN nanofibers annealed at 800 °C 3 h in Argon B) SEM of TiO_2-PAN nanofiber mat annealed at 800 °C 3 h in Argon C) & D) SEM of surface of TiO_2-PAN nanofibers annealed at 800 °C 3 h in Argon.

When TiO_2-PAN nanofibers get heat treated in a two-step process of stabilization at 275 °C in air and then at elevated temperatures at 800 °C for 3 h in Argon, TiO_2 crystallizes into two phases, anatase and rutile as seen in Figure 4.1 A. The nanofibers are 1.5 microns in diameter and have a rough surface. Upon closer observation (Figure 4.3 C &D), particles are seen on the surface of the nanofibers. They are randomly oriented with size ranging from 38 nm to 136 nm. Figure 4.4 A & B shows an SEM closeup of these particles. The morphology ranges from 136 nm length nanorods, to flat platelets.

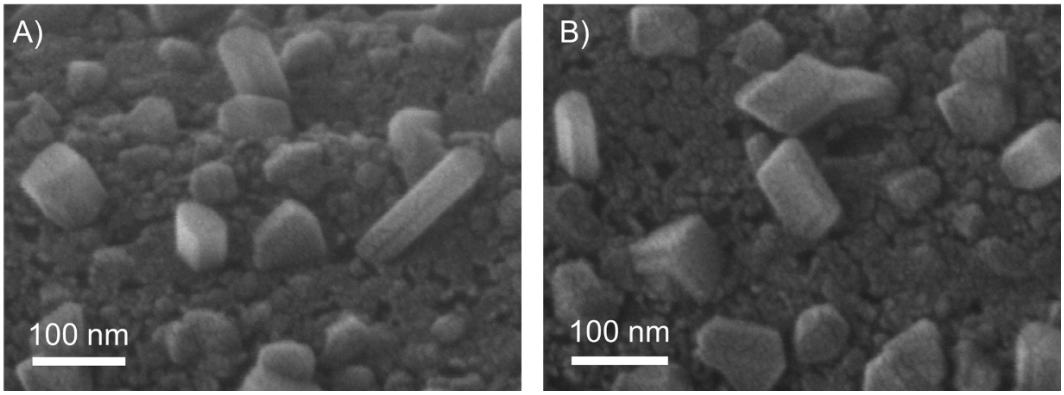

Figure 4.4 SEM of nanoparticles on surface of TiO2-PAN nanofibers annealed at 800 °C 3 h in Argon.

FTIR was performed on As-spun nanofibers with and without TiO_2 added (Figure 4.5). A 2242 cm^{-1} peak is seen in both the TiO_2-PAN and PAN samples that correspond to the C≡N bond stretch. However, the intensity of the nitrile peak decreases when TiO_2 is incorporated in the sample suggesting an interaction between the nitrile and TiO_2. The peak at 1667 cm^{-1} corresponds to the C=O and C=N stretch again reduced when TiO_2 is present.

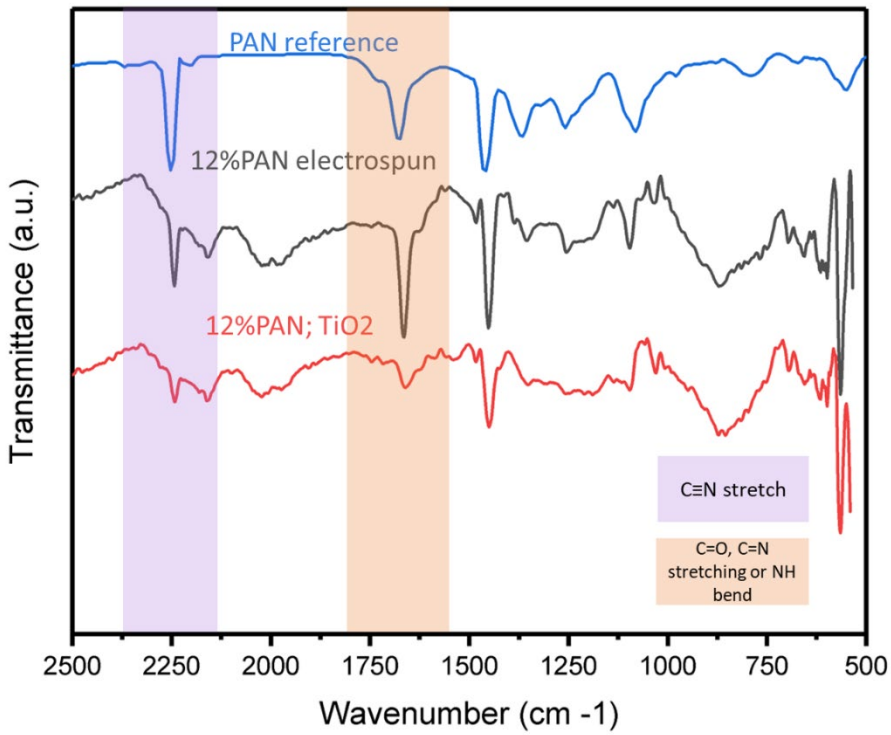

Figure 4.5 FTIR of PAN nanofiber vs PAN-TiO_2 nanofiber as-spun.

4.4.2 Varying Temperature

To observe the phase transformation, crystal and particle growth TiO_2-PAN nanofibers were annealed in Argon at varying temperatures of (400 °C, 600 °C, and 800 °C). XRD was conducted on these samples and shown in Figure 4.5 A. At 400 °C, a broad peak is observed at 24.9 degrees with a crystallite size of 1 nm. The 24.9 degrees corresponds to the amorphous carbon peak that is observed when PAN is carbonized at 400 °C. No TiO_2 peak is observed. Figure 4.6 B also shows no visible particles observed with TiO_2-PAN nanofibers annealed at 400 °C. However, a cross-section of this sample shows particles within the nanofiber. The particles are evenly distributed throughout the nanofiber but there is an 85 nm area near the outer edge of the nanofiber where particles are not present.

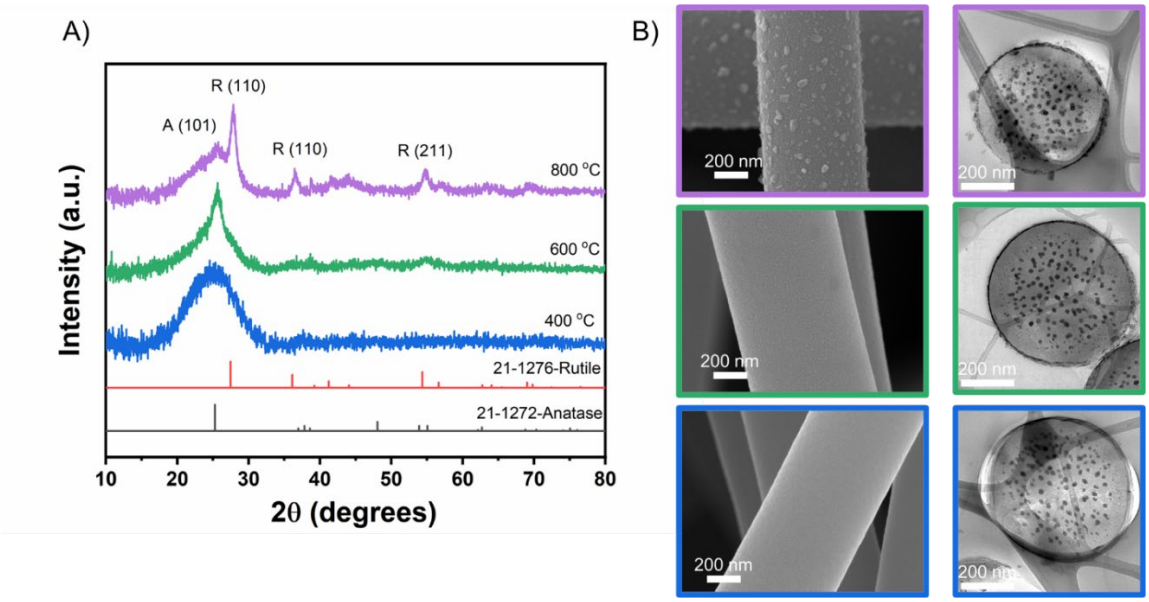

Figure 4.6 A) XRD, B) SEM, and cross-sectional TEM of TiO_2-PAN nanofibers annealed at 400 °C, 600 °C, and 800 °C for 3 h in Argon.

At 600 °C, there is a peak at 25.6 degrees. After doing a Gaussian peak fit, three peaks were identified at 24.7, 25.6 and 27.5 degrees corresponding to a carbon, anatase phase (TiO_2), and the rutile phase (TiO_2) respectively. The carbon crystallite size was calculated to be 1 nm, the anatase to be 1.6 nm and the rutile to be 7.2 nm. The anatase: rutile ratio is 2.56 with the anatase peak being the dominant phase at this temperature. SEM (Figure 4.6 B) again shows no visible particles on the surface of the nanofiber. The cross-sectional TEM shows not change in the size of the nanoparticles inside the nanofiber. At 800 °C, the carbon peak shifts from 24.9 degrees with 1 nm crystallite size. The anatase peak decreases in intensity and shifts slightly to 25.9 degrees. The crystallite size also decreases to 4 nm. The anatase: rutile ratio is .34 with the rutile peak being three times more intense than the anatase peak. SEM micrograph shows visible nanoparticles throughout the surface of the nanofiber ranging from 33 to 80 nm in size.

4.4.3 Varying annealing time

TiO_2-PAN samples were annealed at 1 h, 2 h, and 3 h at 800 °C in Argon. XRD was conducted to observe the crystallization, phase change, and phase ratio of TiO_2 (Figure 4.7). After 1 h of anatase two main peaks are identified at 25.4 and 27.5 degrees corresponding to anatase (101) and rutile (110) respectively. The crystallite size for anatase was calculated to be 11.2 nm and 15.8 nm for rutile. The anatase: rutile ratio was 1.89 making anatase the dominant phase. After 2 hours of annealing, the crystallite size for anatase was 11.5 nm and 19.8 nm for rutile. The anatase crystallite size did not change while the crystallite size for rutile increased by 4 nm. The anatase: rutile ratio decreased to 1.62 still making the anatase phase dominant but showing an increase in the rutile phase. After 3 hours of annealing the anatase crystallite size slightly increased to 12 nm, and the rutile crystallite size decreased to 17.4 nm. The ratio significantly decreased to 1.06 again showing an increase in the rutile phase.

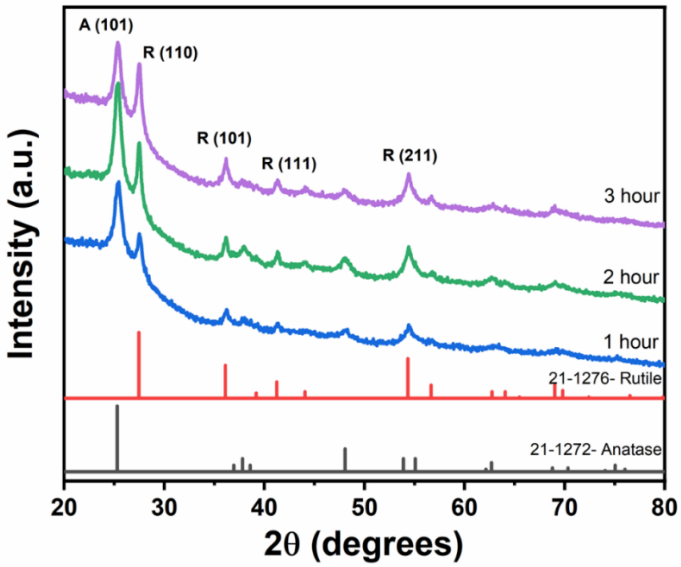

Figure 4.7 XRD of TiO_2-PAN annealed in Argon at 800 °C at 1 h, 2 h, 3 h.

4.4.4 Effects of Atmospheric conditions on crystal growth and phase transformation of TiO_2

TiO_2-PAN nanofibers were annealed in two different atmospheres, Argon and 5%H_2;95%N_2. XRD was performed on these two annealed samples to observe the TiO_2 crystal phase (Figure 4.8 A). Annealing in Argon yields seemingly equal amounts of anatase and rutile with seemingly equal amounts of anatase and rutile the ratio being 1.06. The crystal size for the 25.4 degrees (anatase) peak is 11.2 nm and 17.4 nm for the 27.5 degrees (rutile) peak. The particles on the surface of the nanofibers have a platelet morphology (Figure 4.8 B).

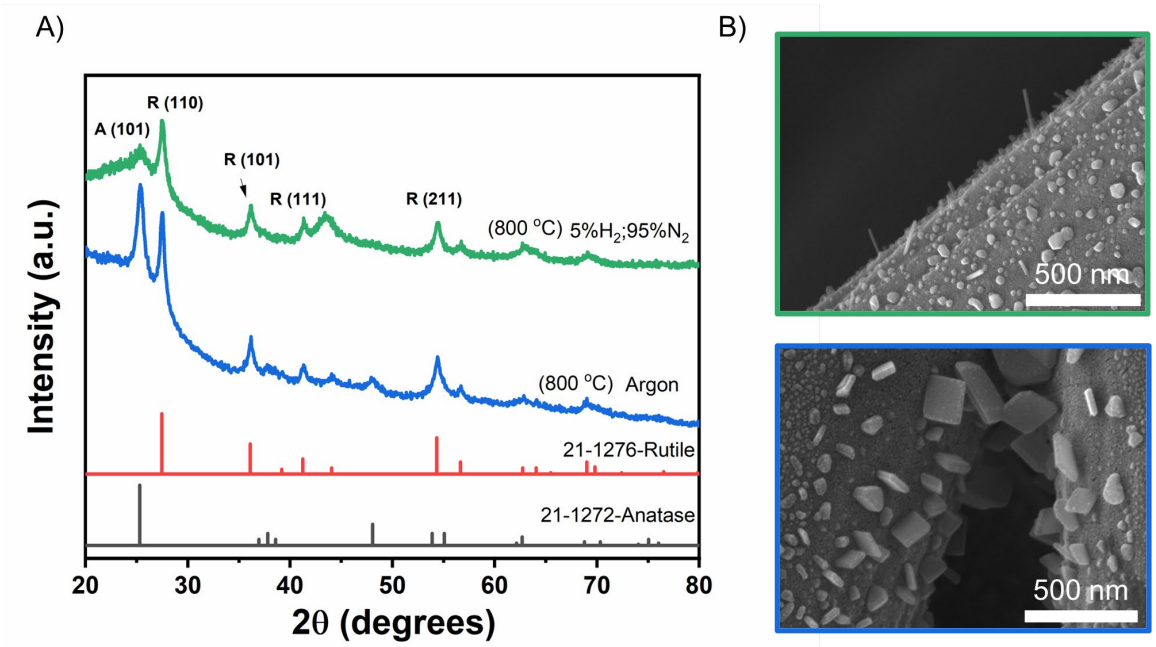

Figure 4.8 A) XRD of 12 wt.% PAN-TiO_2 annealed at 800 °C 3 h in 5%H_2;95%N_2 vs Argon B) SEM of PAN/TiO_2 nanofibers annealed in 5%H_2; 95%N_2 vs Argon.

When annealed in a reducing environment using 5%H_2:95%N_2, significantly more rutile is formed when compared to anatase. The anatase: rutile ratio is 0.65. The anatase crystallite size is 5.3 nm while the rutile is 11.8 nm. Furthermore, nanorods are seen

growing from the nanofiber surface (Figure 4.8 B). It is likely that the polymer/carbon matrix plays a significant role in controlling Ti-O_x species diffusion by presenting pendant groups with an affinity to bind to the metal. However, the annealing atmosphere also plays a role by modifying the polymer structure and its transition to carbon, which changes the interaction between the matrix and metal oxide species and will therefore affect growth rates of TiO_2, as observed between Argon and forming gases. Furthermore, the surfaces of these metal oxides will have different surface energies in these atmospheres and thus grow at different rates as well.

4.4.5 TiO_2 interaction with PAN and Acetic Acid during carbon fiber synthesis

To understand the effects of the solvents and the polymer has on the crystal growth and phase transformation of TiO_2, three different solutions, 1) CH_3COOH + $Ti(C_4H_9O)_4$ + PAN, 2) CH_3COOH + $Ti(C_4H_9O)_4$, and 3) PAN + $Ti(C_4H_9O)_4$ were made. Following the carbon fiber process procedure, they were stabilized at 275 °C for 1 hour in air and annealed at 800 °C for 3 hours in a reducing atmosphere of 5%H_2; 95%N_2. Figure 4.9 A shows SEM of sample 3 (PAN +$Ti(C_4H_9O)_4$ before heat treatment. A fibrous structure is observed along with micron size round particles. When acetic acid is added, these micron size particles are not present (Figure 4.9 B).

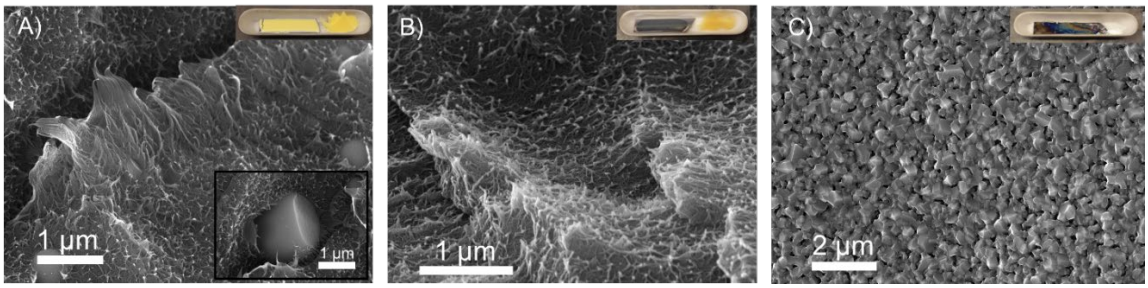

Figure 4.9 SEM of drop cast samples A) TiO_2 precursor + PAN B) TiO_2 precursor +PAN +CH_3COOH C) TiO_2 precursor +CH_3COOH.

XRD was done on these annealed drops cast samples to determine crystal phase and crystal size (Figure 4.10 A). When no polymer is added to the system, TiO_2 is free to diffuse, crystallize and grow into large crystals. The anatase (25.4°) and rutile (27.5°) peaks are present with the anatase having a crystal size of 1.7 nm and rutile having a 50 nm crystal size. These large crystals are seen in SEM (Figure 4.10 B).

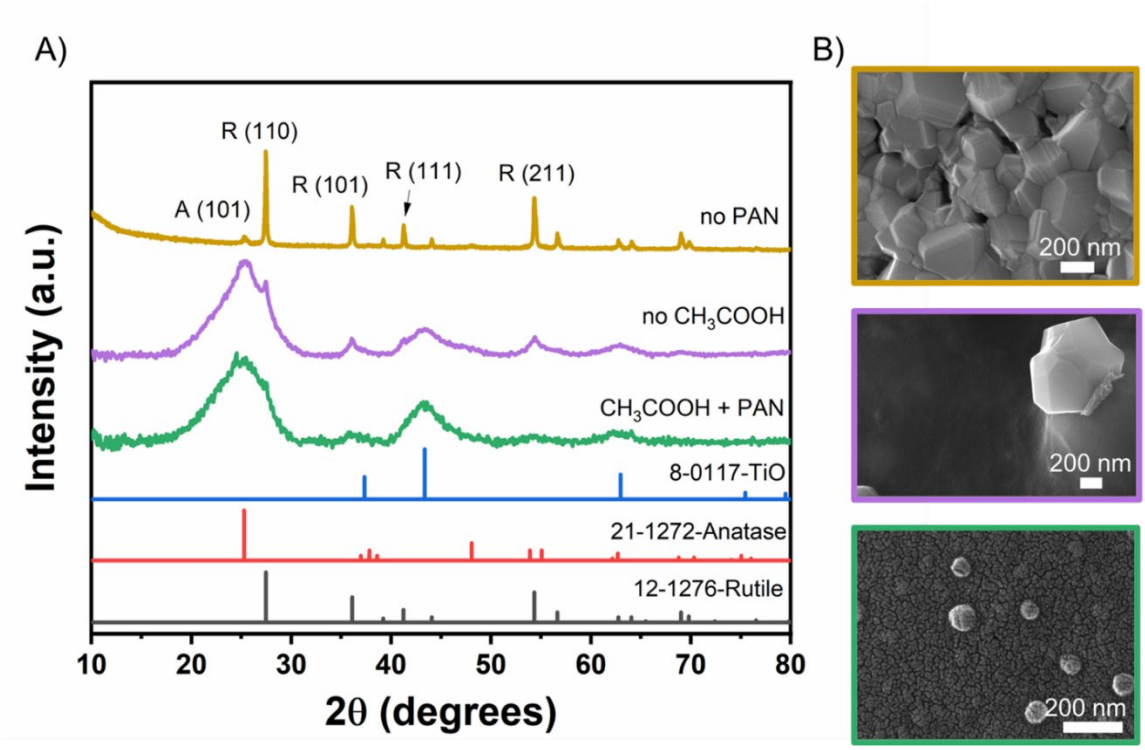

Figure 4.10 A) XRD of annealed drop cast samples at 800 °C 3 h in 5%H_2; 95%N_2 B) SEM of particles on surface of annealed drop cast samples.

When just PAN and Titanium precursor are annealed large micron size particles are seen before heat treatment, after heat treatment a broad anatase peak is observed along with a rutile shoulder peak. The crystal size for anatase is 3.4 nm and 24 nm for rutile. The micron size particles have formed faceted particles. It is suggested that these large agglomerates seen before annealing are the large particles seen after annealing. When all components are present, (CH_3COOH, PAN, and $Ti(C_4H_9O)_4$) a broad peak is observed in

XRD. After gaussian peak fitting, anatase and rutile peaks were identified and measured to have a crystal size of 5 nm and 12 nm, respectively. SEM shows ~90 nm particles on the surface of the drop cast film and no large micron sized particles are observed. This suggests that the addition of the acetic acid is preventing the hydrolysis and condensation of these large TiO_2 particles. Although acetic acid slows down the hydrolysis and condensation it does not completely stop this reaction. In the film where all components are present, the surface particles are significantly smaller when compared to the other two samples. This shows that both the polymer and the acetic acid play a role in the slowing down of anatase to rutile transformation in this system. The steric hindrance of the polymer slows down the diffusion of the TiO_2, and the acetic acid significantly reduced the hydrolysis and condensation reactions that initially nucleate prior to heat treatment.

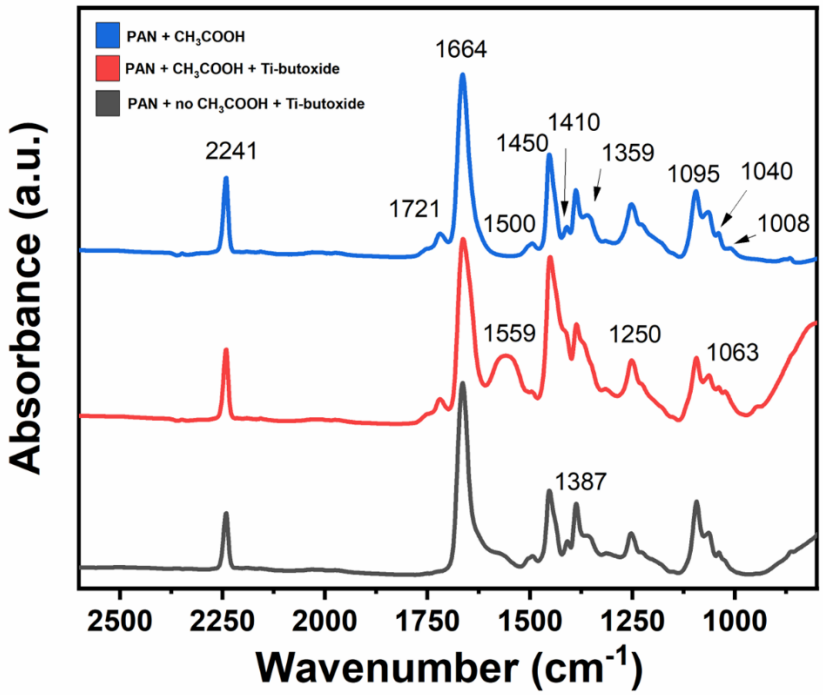

Figure 4.11 FTIR of drop cast samples with PAN, CH_3COOH, and $Ti(C_4H_9O)_4$.

FTIR was conducted to identify the chemical bonds of drop cast samples. Figure 4.11 shows three FTIR plots of the drop cast samples before heat treatment. All three plots have the 2241 cm^{-1} peak corresponding to the nitrile stretch as well as the 1664 cm^{-1} peak indicating the C=O, and C=N stretching. When PAN, $Ti(C_4H_9O)_4$, and CH_3COOH are added a distinct 1559 peak is observed. Ferrin et al. performed FTIR on $Ti(C_4H_9O)_4$ and CH_3COOH mixtures and identified a 1570 cm^{-1} corresponding to a COO^- stretch [15]. This spectral feature is consistent with the formation of $Ti_aO_b(OBu)_c(OA_C)_d$ complexed where oxo-bridges are formed from intramolecular and/or intermolecular esterification process [15]. FTIR spectroscopy can be used to determine the coordination mode of the carboxylate ligands in metal carboxylates [16]. The 1550 cm^{-1} peak in this system suggests that the carboxylate ligand is a chelating bidentate complex.

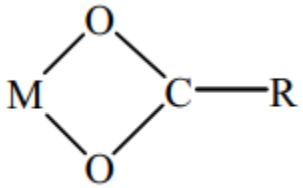

4.4.6 Polymer effects on crystal structure and phase transformation of TiO2

To understand the effects of different polymer matrices on the crystallization of TiO_2 nanoparticles, polymer blends mixed with titanium alkoxides were prepared and nanofibers were electrospun from these solutions. Nanofibers were then heat-treated using a two-step process of oxidation in air and annealing in an inert atmosphere at 800 °C for 3 hours. Figure 4.12 shows XRD on the three polymer-TiO_2 samples. As previously shown, TiO_2-PAN samples annealed at 800 °C for 3 hours in Argon show two phases of TiO_2,

anatase and rutile. Large rod-like and faceted particles are observed on the surface of the nanofibers. Observation of this TiO_2-PAN sample by SEM reveals platelet structures on the nanofibers, which are not observed in the other two samples, which have a more isotropic morphology. With the TiO_2-PVP samples, anatase and rutile are also observed, but the crystal size for both anatase and rutile are smaller when compared to the PAN nanofibers being 4 nm and 10 nm respectively. The ratios for anatase: rutile in PVP and PAN samples are 1.12 and 1.06. When PAN and PVP are mixed, anatase is the dominant phase with a ratio of 3.48 almost 3.5x the intensity as rutile. The crystal size for anatase is 6 nm and the rutile crystal size is also 6 nm. This suggests that the polymer plays a role in the phase transformation and crystal growth of TiO_2.

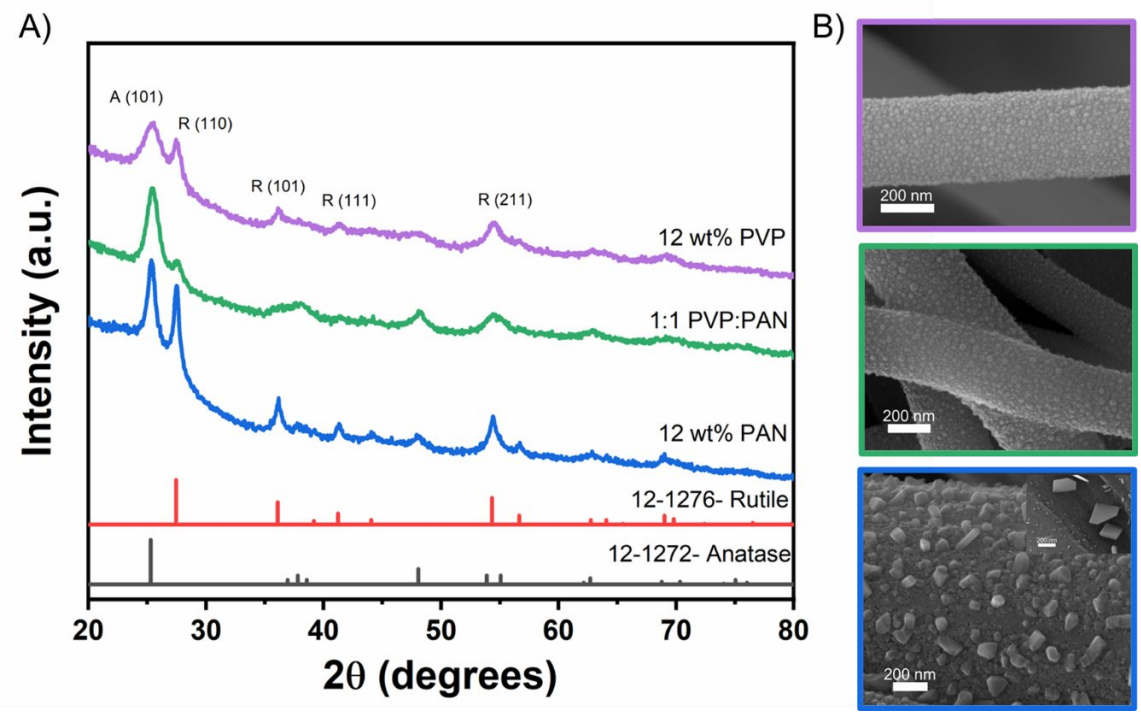

Figure 4.12 A) XRD plot of PVP, PAN, and 1:1 PVP: PAN TiO_2 nanofibers annealed at 800 °C for 3 h in Argon B) SEM micrographs of 12 wt.% PVP (purple), 1:1 PVP: PAN (green) and 12 wt. % PAN TiO_2 (blue) nanofibers.

Gao et. al. studied thermal stability of nanofibers loading with cobalt nanoparticles. They used a PVP/PAN mixture and compared it to pure PAN. They found that the onset temperature of degradation was lower in the PVP/PAN-metal composite, but the overall thermal stability was enhanced in the metal-polymer composite. They attributed this to the highly porous structure of the PVP/PAN which formed a protective barrier from the decomposition of PVP, retarding the volatilization of the pyrolysis products [17]. We hypothesize that the inhibition of phase transformation in the PVP/PAN sample is attributed to the increase in thermal stability of PVP/PAN/TiO2 structure.

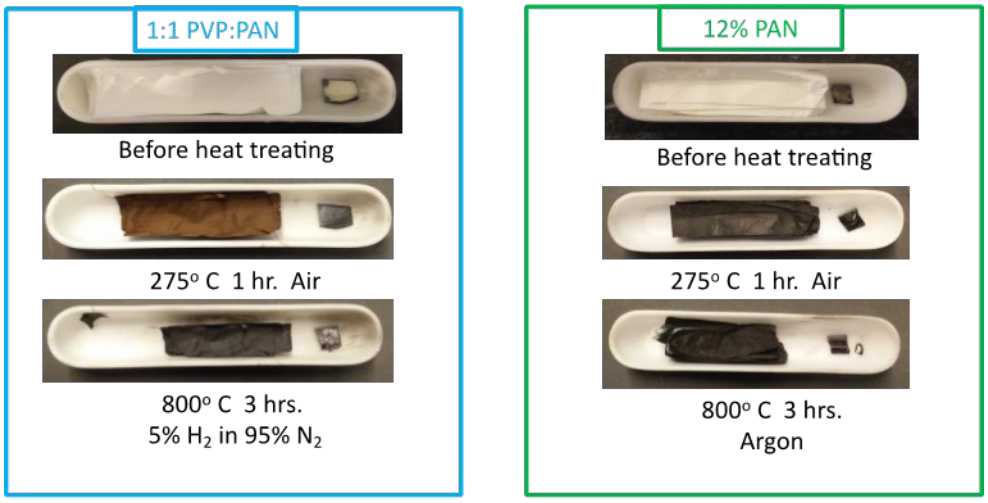

Figure 4.13 Image of PVP: PAN sample vs PAN as spun, after stabilization, and after annealing.

The PVP: PAN sample after oxidation (Figure 4.13) appears to be a light brown color compared to the PAN sample which appears to be black. The color change of PAN after the stabilization step is attributed to the cyclization reaction occurring during this step. The brown color on the PVP: PAN sample indicates that the cyclization reaction did not occur completely, due the mixture of the PAN and PVP where the PVP does not cyclize during the stabilization step, as well as interacting with the PAN and disrupting the cyclization process.

4.5 Conclusion:

This study revealed that when Titanium butoxide, acetic acid, is mixed in a polymer matrix, electrospun and heat treated to carbon fiber, two polymorphs of TiO2 grow within this matrix. Temperature studies reveal that anatase is the dominant peak at 400 °C and 600 °C annealing temperatures. As temperature increases, particles diffuse and grow on the surface of the nanofiber. The morphology of these particles is dependent on the atmospheric environments in which they are annealed. When annealed in a reducing atmosphere, nanowires morphology is observed as well as rutile being the dominant phase.

When annealed in Argon, both anatase and rutile are observed with a near 1:1 ratio. The surface particles have a platelet morphology. Drop-cast studies showed that the effect of acetic acid slows down the hydrolysis and condensation reactions within the polymer matrix forming a chelating bidentate complex slowing down the phase transformation of anatase to rutile. Different mixtures of PVP and PAN polymers were made into TiO_2-carbon nanofibers. It was observed that the anatase: rutile ratio increases when PVP and PAN are present due to the disruption of the crystalline structure of the polymer that pure PAN and PVP have. We believe this PVP:PAN mixture slows down the diffusion of TiO_2 species due to steric hindrance preventing the growth and thus phase transformation of anatase to rutile. This study reveals how processing parameters affects the crystal growth and phase transformation of TiO_2 in a polymer-carbon nanofiber matrix. The insights obtained in this study can help in controlling the phase ratio of this system to fabricate efficient target-selective materials for photodegradation membrane.

References

[1] S.-Y. Lee and S.-J. Park, "TiO2 photocatalyst for water treatment applications," *Journal of Industrial and Engineering Chemistry,* vol. 19, no. 6, pp. 1761-1769, 2013.

[2] K. Nakata and A. Fujishima, "TiO2 photocatalysis: Design and applications," *Journal of Photochemistry and Photobiology C: Photochemistry Reviews,* vol. 13, no. 3, pp. 169-189, 2012.

[3] D. A. H. Hanaor and C. C. Sorrell, "Review of the anatase to rutile phase transformation," *Journal of Materials Science,* vol. 46, pp. 855-874, 2011.

[4] J. Zhang, P. Zhou, J. Liu and J. Yu, "New understanding of the difference of photocatalytic activity among anatase, rutile and brookite TiO2," *Physical Chemistry Chemical Physics,* vol. 16, pp. 20382-20386, 2014.

[5] T. Luttrell, S. Halpegamage, J. Tao, A. Kramer, E. Sutter and M. Batzill, "Why is anatase a better photocatalyst than rutile? - Model studies on epitaxial TiO2 films," *Scientific Reports,* vol. 4, p. 4043, 2014.

[6] D. O. Scanlon, "Band alignment of rutile and anatase TiO2," *Nature Materials,* vol. 12, pp. 798-801, 2013.

[7] P. I. Gouma and M. J. Mills, "Anatase-to-Rutile Transformation in Titania Powders," *Journal of American Ceramic Society,* vol. 84, no. 3, pp. 619-622, 2004.

[8] H. Shin, H. S. Jung, K. S. Hong and J.-K. Lee, "Crystal phase evolution of TiO2 nanoparticles with reaction time in acidic solutions studied via freeze-drying method," *Journal of Solid State Chemistry,* vol. 178, no. 1, pp. 15-21, 2005.

[9] E. Berardo, *Modelling the Excited State Properties of TiO2 Nanoparticles,* London, 2015.

[10] J. Schneider, M. Matsuoka, M. Takeuchi, J. Zhang, Y. Horiuchi, M. Anpo and D. W. Bahnemann, "Understanding TiO2 Photocatalysis: Mechanisms and Materials," *Chemical Reviews,* vol. 114, no. 19, pp. 9919-9986, 2014.

[11] G. Muthukumar, B. .Arjunkumar, R. Vignesh and G. Ramalingam, "A Study of Photocatalytic Degradation of Betalain Pigment from Kitchen Waste,

Semiconductive Nanostructured TiO2 Used as a Photocatalyst," *Materials Science Research India,* 2018.

[12] J. Yu, T. Maa and S. Liu, "Enhanced photocatalytic activity of mesoporous TiO2 aggregates by embedding carbon nanotubes as electron-transfer channel," *Physical Chemistry Chemical Physics,* vol. 13, pp. 3491-3501, 2010.

[13] S. J. Doh, C. Kim, S. G. Lee, S. J. Lee and H. Kim, "Development of photocatalytic TiO2 nanofibers by electrospinning and its application to degradation of dye pollutants," *Journal of Hazardous Materials,* vol. 154, no. 1-3, pp. 118-127, 2008.

[14] B. A. Marinho, S. M. A. G. U. d. Souza, A. A. U. d. Souza and D. Hotza, "Electrospun TiO2 nanofibers for water and wastewater treatment: a review," *Journal of Materials Science ,* vol. 56, pp. 5428-5448, 2021.

[15] F. Perrin, V. Nguyen and J. Vernet, "FT-IR Spectroscopy of Acid-Modified Titanium Alkoxides: Investigations," *Journal of Sol-Gel Science and Technology,* vol. 28, pp. 205-215, 2003.

[16] R. Mehrotra and R. Bohra, Metal Carboxylates, London; New York: Academic Press, 1983.

[17] D. Gao, H. Qiao, Q. Wang, Y. Cai and Q. Wei, "Structure, Morphology and Thermal Stability of Porous Carbon Nanofibers Loaded with Cobalt Nanoparticles," *Journal of Engineered Fibers and Fabrics,* vol. 6, no. 4, 2011.

Chapter 5 Dynamic Studies on in-situ exsolved nanoparticles on perovskite-based materials in redox environments

5.1. Introduction

There is an increasing need to find a cost-effective, earth abundant and high performing materials for carbon and utilization. Precious metal-based catalysts have shown to be an effective catalytic material however, they are expensive to make. Nickel catalysts are extensively used due to their low cost and high reactivity for methane reforming [1].However, nickel is prone quick deactivation due to coking and sintering so there remains a motivation to make a highly active sinter-tolerant catalyst and remains a considerable challenge [2].

There have been steps to extend the lifetime of the metal catalyst by alloying the active catalyst and creating bimetallic systems. In addition, using supporting materials shows to be a promising solution to making better catalysts. A class of supports used are perovskite metal oxides (PMOs) which have high ion conductivity, overall resistance to coking and sintering, high activity, and stability [3] [4].

The phenomenon of exsolution in perovskite type oxides has been studied as a method to synthesize nanoparticles that strongly adhere to their supports. Reducible metals that constitute the B site of ABO_3 type oxides egress from the perovskite matrix and form nanoparticles on the surface of the parent oxide [5] [6]. $LaFeO_3$ has shown a high thermal stability at elevated temperatures above 800 °C which makes it an appropriate candidate for use as a catalyst support [3]. Stabilizing the active metal phases by perovskite oxide precursors is an effective strategy for obtaining high metal dispersion [7]. The reversibility

of exsolution also allows for the reactivation of catalysts through simple redox cycling without loss in activity due to sintering. The influence of factors such as defects [8] [9] composition [4] [10] and reducing temperature[48] have also been explored which allow for rationally designing catalysts through exsolution. Exsolution offers a facile pathway for the synthesis of bimetallic or multi-metallic catalysts which are another solution to enhance catalyst activity and stability [1] [11] [12]. The combination of Ni with Fe as catalysts has been studied for their stability towards coking and sintering [13] [14] [15] [16] [17] [18]. In reaction conditions of dry reforming, steam reforming or partial oxidation of methane, Fe^0/FeO_x redox couple which oxidizes surface carbon species, and this prevents or minimizes deactivation due to coking [19] [20].

Perovskite-based materials as well as the Ni-Fe bimetallic catalyst systems are dynamic in nature, responding to changing redox conditions. This warrants research that capture the dynamics of the system with appropriate techniques. In this research, we capture the transition of Ni and Fe as they migrate in and out of metallic and perovskite phases in reductive, oxidative and reaction environments. In-situ X-ray Absorption Spectroscopy captures the changing electronic and coordination environments surrounding Ni and Fe as exsolution gradually occurs during reduction and reverses during oxidation. Similarly, we also use XAS as tool to observe the interaction between metallic Ni, Fe, and the parent perovskite during reaction of dry methane reforming. This is supported with ex-situ High-Angle Annular Dark Field Scanning Tunnelling Electron Microscopy (HAADF-STEM) with Energy Dispersive X-ray Spectroscopy (EDS) for samples subjected to reduction, re-oxidation, or reaction for differing time intervals. Powder X-ray

Diffractograms also capture the emergence and disappearance of metallic phases. We also discuss how extent of exsolution of Ni and Fe is reflected in the catalytic performance towards DRM.

5.2 Experimental Section

5.2.1 Catalyst Preparation

All chemicals and reagents were used as received. $La(NO_3)_3.6H_2O$, $Fe(NO_3)_3.9H_2O$, $Ni(NO_3)_2$, anhydrous citric acid and ethylene glycol were all purchased from Sigma Aldrich (Sigma Aldrich, Birmingham, Alabama).

The perovskite oxide, nominally $LaFe_{0.8}Ni_{0.2}O_{3-x}$ was prepared sol-gel Pechini method as described in literature[49]. 3.56 g of $La(NO_3)_3.6H_2O$, 2.66 g of $Fe(NO_3)_3.9H_2O$ and 0.48 g of $Ni(NO_3)_2$ were mixed in stoichiometric quantities and dissolved in 10 mL of DI water. The beaker was placed on a hot plate at 60 °C and stirred until fully dissolved. 4.74 g of anhydrous citric acid (3 mols./mol. perovskite) and 1.08 mL of ethylene glycol (1 mol./mol. perovskite) were mixed with 30 mL of DI water in a separate beaker. The citric acid/ ethylene glycol solution was subsequently added dropwise to the precursor solution. The mixture was evaporated in a drying oven at 110 °C overnight and the resulting xerogel was finely ground in a mortar and pestle and calcined at 800 °C for 2 h with a heating rate of 5 °C/min. The samples were then reduced in a Catlab (Hiden Analytical CATLAB, Warrington, United Kingdom) furnace in $5\%H_2$;95%He at 700 °C for varying times (10 min, 30 min, 60 min, 90 min, and 120 min) to observe the exsolution of the metals from the perovskite before performing catalyst testing. The perovskite was

regenerated in the CATLAB furnace by heating 100 mg of material to 700 °C for 2 hours in 20%O_2/He gas mixture.

5.2.2 Catalyst Characterization

Temperature Programmed Reduction: Temperature Programmed Reduction (TPR) was performed in a quartz tube microreactor (Hiden Analytical CATLAB, Warrington, United Kingdom) at 700 °C with a 15 °C/min ramp rate and held at varying times (10 min, 30 min, 60 min, 90 min, and 120 min).

Microscopy: Elemental analysis and morphological features were observed using TEM (Titan Thermi-300kC, FEI) EDS and STEM imaging. TEM samples were prepared by dispersing samples in DI water, sonicating for 10 min, and depositing them onto ultrathin carbon films on holy carbon supports with a 400-mesh copper grid (Ted Pella, Redding CA) using a 1 mL pipette.

X-ray Diffraction: X-ray Diffraction (XRD) spectra were collected on a PANalytical Empyrean Series 2 with a step-size of 0.026º and dwell time of 30 seconds. The diffractograms were collected in range of 2θ of 5 to 90 with a Cu K-α radiation source.

X-Ray Absorption Spectroscopy (XAS): In-situ XAS characterization experiments were conducted at beamline 9-3 at the Stanford Synchrotron Radiation Light source. Samples were loaded in a quartz tube mounted on a tube reactor. The catalyst sample was scanned in fluorescence mode with a Canberra 100 element Ge monolith detector. A liquid nitrogen cooled Si(220), monochromator was used to select photon energy. Fe and Ni foils were used as standards which were scanned, in transmission mode, prior to scanning the samples. Scans were collected around the Fe K-edge (E_0 = 7112 eV) and Ni K-edge (E_0 =

8333 eV). X-ray Absorption Near Edge Spectroscopy measurements were taken in-situ as the sample was subjected to a changing redox conditions: (1) A Temperature Programmed Reduction with temperature ramping up at 10 °C/min and dwelling at 700 °C in 5%H_2/He (2) A Temperature Programmed Oxidation in 20%O_2/He of a reduced sample cooled to room temperature before ramping temperature back to 700 °C and then dwelling and (3) DRM mixture of 5% CH_4+5% CO_2 + 90% introduced at 700 °C, following reduction and then a purge in He. Each XANES scan took 92s to complete, so the temperature difference between successive scans was about 15 °C. Extended X-Ray Absorption Fine Structure measurements were conducted at the end of each stage mentioned above after cooling down to room temperature to minimize distortions observed at high temperatures. Four scans were taken, aligned, and averaged for minimizing noise in the signal.

The data collected were calibrated, merged and normalized with the Athena interface of the Demeter package[50]. EXAFS data were extracted in k space and Fourier transformed in the k-range of 3-11.5 $Å^{-1}$. Passive electron reduction factor, S_O^2 was calculated to be 0.61 for Fe K edge and 0.81 for Ni, by fitting data collected for Fe foil and Ni foil. The EXAFS data was fit to theoretical models generated by FEFF6 code, in the R-range of 1-6 Å in the Artemis interface of the Demeter package.

Methane reforming catalyst testing

DRM was performed in a fixed-bed reactor at atmospheric pressure. Steady state conversion of CH_4 and CO_2 was carried out using 100 mg of catalyst supported on silica wool. Before catalytic testing, the material was reduced at 700 °C in 5%H_2;95%He, with 60 ml/min flow rate at varying times (for 0, 10, 30, 60 and 120 minutes) to promote

exsolution of the Ni and Fe. After reduction, the material was kept at 700 °C for catalytic testing and was performed for 15 minutes. The concentrations of CO and H_2 were analyzed by a Hiden Quantitative Gas Analyzer (QGA) mass spectrometer. The conversion values were quantified using the mass spectral response and measured gas flow rates.

5.3 Results and Discussion:

5.3.1 Microstructure analysis and dry methane reforming

XRD was done on the material to determine its crystal structure and how it changes with varying reduction time (Figure 5.1). The XRD peaks show the orthorhombic phase of $LaFeO_3$. The varying reduction time does not seem to change the overall perovskite structure. XRD shows full solubility of Ni and Fe as there are no visible XRD peaks of these phases present. However, upon closer look (Figure 5.1 B) of the 32.4° 2θ peak, there is a shift to a lower 2θ from 10 min to 60 min reduction. The shift to a larger 2θ can be indicative of the nickel diffusing out of the perovskite causing an increase in oxygen vacancies. . The shift to a higher 2θ at 90 min represents the Fe diffusing out of the support causing shrinkage in the unit cell lattice. Thus, the lattice expands initially and contracts thereafter during the passage of exsolution. This is likely because the reduction of the metals precedes their egress. The formation of O site vacancies has an expansionary effect on the lattice. Moreover, metallic Ni has a larger radius than ionic Ni^{+2} and Ni^{+3} and its presence in the lattice of the perovskite also leads to lattice expansion [21]. Gradually, exsolution drives the metallic nickel outward and the lattice contracts.

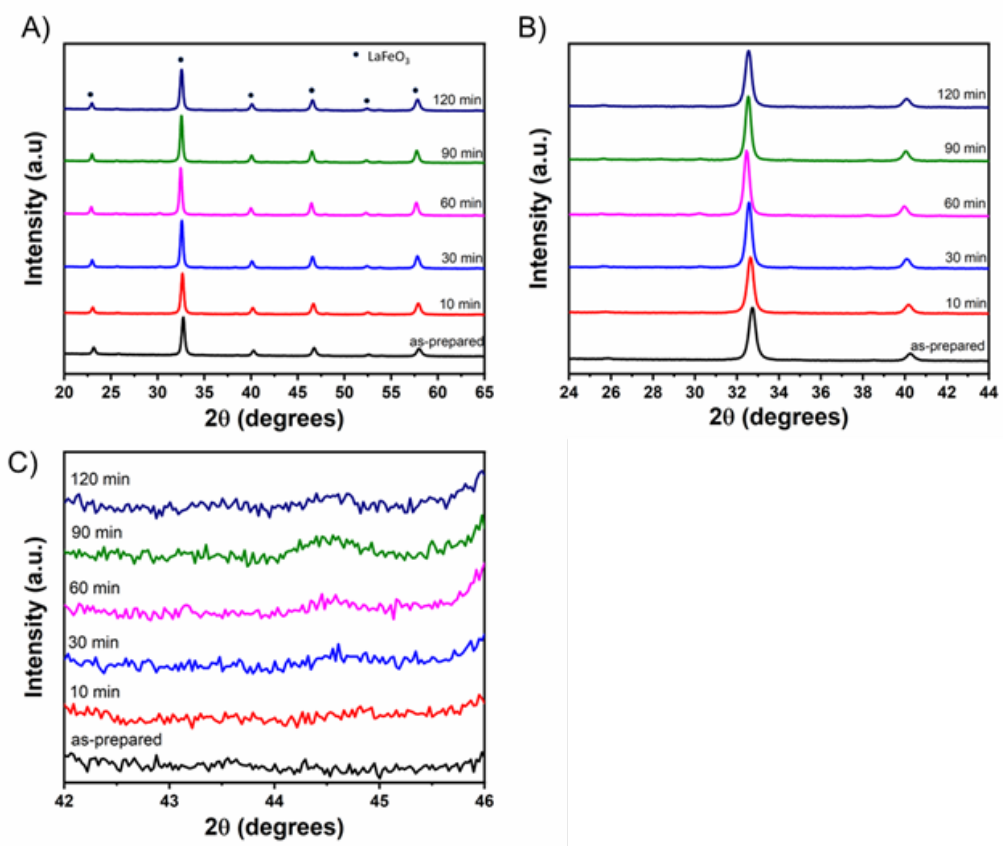

Figure 5.1 A) XRD $LaFe_{0.8}Ni_{0.2}O_3$ as-prepared and reduced (10 min, 30min, 60min, 90 min, 120 min) at 700 ºC B) XRD of $LaFe_{0.8}Ni_{0.2}O_3$ highlighting (121) peak C) XRD of $LaFe_{0.8}Ni_{0.2}O_3$ from 42-46 2θ.

Elemental and structural morphology was done using STEM-HAADF and EDX at each reduction step (as-prepared, 10 min, 30 min, 60 min, 90 min, and 120 min) at 700 °C in a reducing environment of 5%H_2;95%He. As-prepared sample (Figure 5.2) shows no visible nickel or iron nanoparticles. Both metals are within the LFNO bulk. At 10 minutes, small nickel nanoparticles are seen emerging from the LFNO onto the surface with an average size of 12 nm ± 5 nm. After 30 minutes of reduction, the nanoparticle density significantly increases with little change to the average particle size of 11 nm ± 5 nm. After 60 min of reduction, an increase in particle size is observed (20 nm ± 6 nm) and smaller

disbursement throughout the surface of the LFNO. At 90 min, the nanoparticle size increases, larger particles are seen along with small nanoparticles making the average particle size 16 nm ± 8. At 120 min, the nickel nanoparticles have formed larger particles and the smaller particles have reduced in quantity.

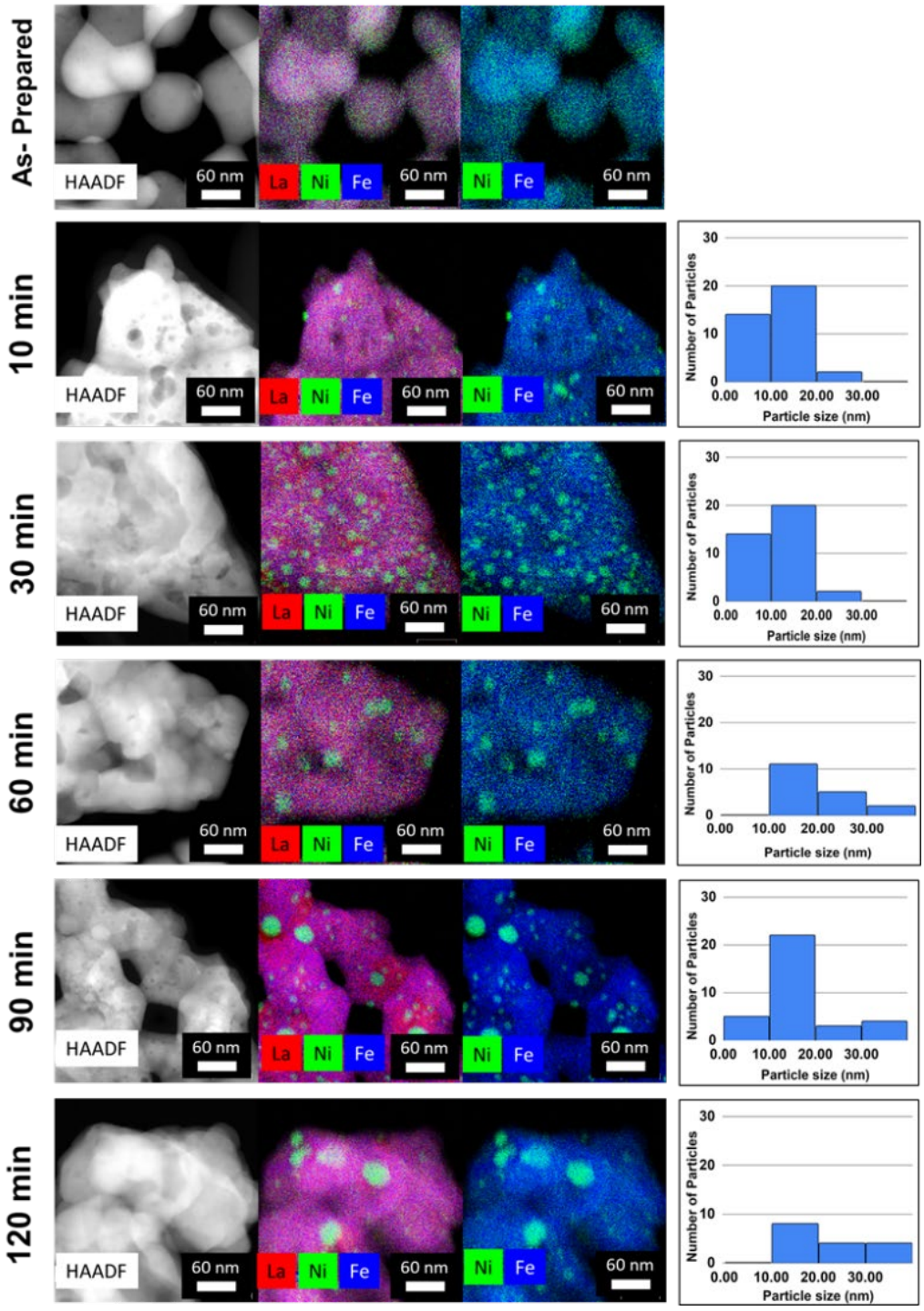

Figure 5.2 STEM Micrographs of $LaFe_{0.8}Ni_{0.2}O_{3-x}$ perovskite sample as prepared and after reduction in 5%H_2/He for a reduction time of 10 minutes, 30 minutes, 60 min, 90 min, 120 min. The adjacent histograms show the size distribution of the exsolved nanoparticles.

Lai and Manthiram suggested that particle growth during exsolution occurs through mechanisms involving coalescence or Ostwald ripening [22]. The authors describe that both mechanisms can occur. When the interaction is weak very spherical particles are observed, but strong metal-support interactions change that shape to a hemispherical or flat morphology. This strong interaction makes the nanoparticles less mobile and decrease the rate of coalescence. In Ostwald ripening, smaller particles can migrate on the surface of the support and merge into a larger particle like a dissolution-condensation mechanism [23]. They claim that Ostwald ripening is usually the dominant mechanism at elevated temperatures but both mechanisms are present. The authors described how temperature moderated particle growth and nucleation and we surmise that duration of reduction similarly pushes nanoparticles to agglomerate. This likely causes a decrease in the areal density of nanoparticles reduced for longer durations.

.

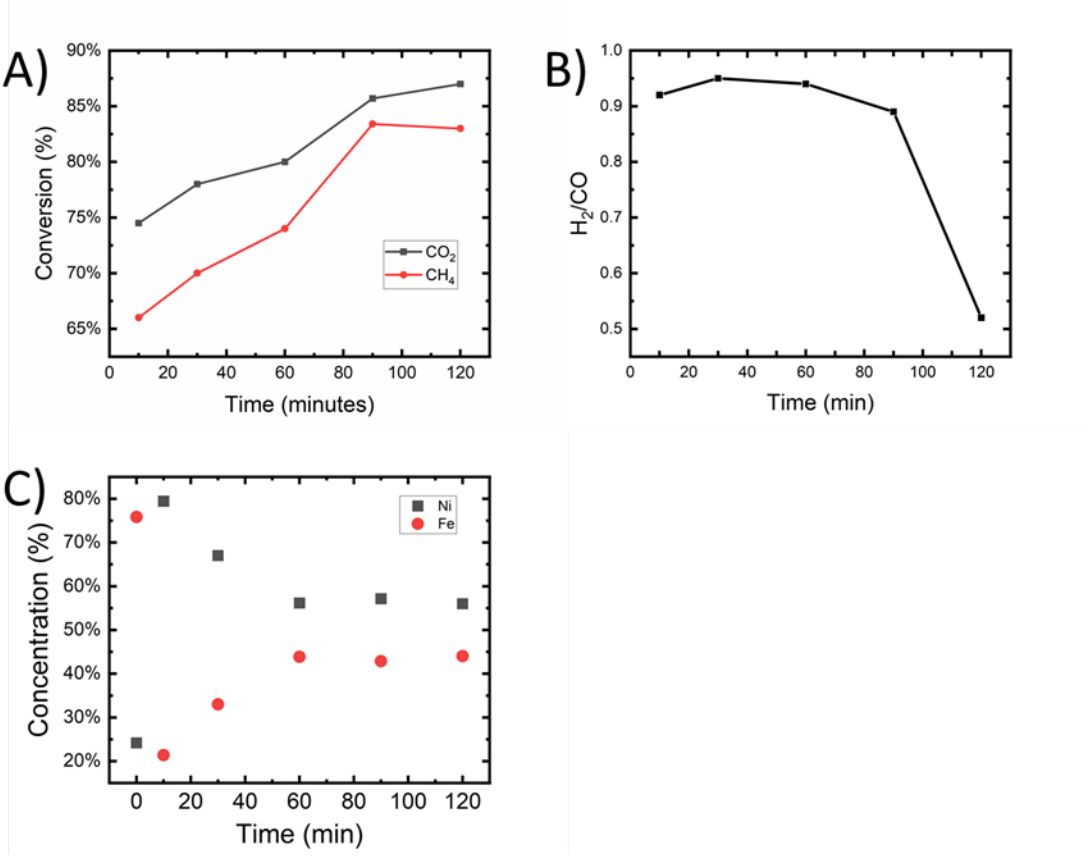

Figure 5.3 A) Catalytic activity of LFNO of CO_2 and CH_4 conversion B) H_2/CO ratio of LFNO C) Fe and Ni elemental concentration in Ni nanoparticles

The DRM catalytic activity was performed at 700 °C for LFNO to investigate the catalytic performance of varying reduction time of 10 min, 30 min, 60 min, 90 min and 120 min. The catalytic performance is shown in Figure 5.3. The catalysts were tested for their conversion yield at 700 °C for 15 min of CH_4 and CO_2 as well as the H_2:CO product ratio.

The catalytic activity starts at 66% for CH_4 and 75% for CO_2 conversion at 10 minutes. Both CH_4 and CO_2 conversion increases until 90 minutes where the conversion for CH_4 and CO_2 is 82% and 84% respectively. At 120 min, CO_2 conversion continues to increase to 87% and CH_4 conversion decreases slightly to 83%. The H_2/CO ratio starts at

0.9 at 10 minutes and increases to 0.95 at 30 minutes reduction. At 60 min and 90 min, the H_2/CO decreases slightly to 0.96 and 0.89 respectively. At 120 min, the H_2/CO falls significantly to 0.52 indicating an increase in production in CO and an increase of the RWGS reaction.

Figure 5.3 C. shows the concentration of Fe and Ni in the catalyst particle supported on LFNO. In the bulk, there is more Iron than Nickel which corresponds to 75% Fe and 25% Ni in the bulk at time zero. At 10 min reduction time, nucleation has occurred, and nickel nanoparticles begin to emerge at an average size of 11 nm ± 5 nm. The particle elemental composition is Nickel- 80% and Iron- 20%. At 30 min, the concentration is Ni-66% and Fe- 34%. At 60 min, 90 min and 120 min the concentration is Ni-55% and Fe-45%. The higher concentration of Ni compared to Fe in the initial time of reduction indicates that the rate of exsolution is higher in nickel than iron. As is discussed in the XAS section further, Nickel exsolves out of the LFNO bulk material before iron due to nickel metal reducing to metal at a lower temperature than iron. The iron increases in concentration as reduction time increases and plateaus at 45% reaching a maximum concentration inside the nanoparticle. It appears that the H_2/CO ratio is highest at 30 minutes with a Ni concentration of 65% and Fe concentration 35%. At higher concentrations of Fe, the relative activity of the catalyst to activate CH_4 decreases which could increase CO_2 consumption through side reactions such as reverse water gas shift. Moreover, CO_2 can itself oxidize the perovskite. A more reduced perovskite-based catalyst has a greater propensity to consume CO_2 to oxidize constituent metals, particularly Fe and fill its vacant O sites. This suggests that there is an optimized Ni to Fe concentration and

the particle size, as dictated by the extent of exsolution plays a more important role for the H_2/CO conversion efficiency. Thus, the lower H_2/CO ratio is due to increase in CO_2 consumption for the oxidation of the perovskite itself, rather than an increase in RWGS relative to DRM. Increasing the Fe concentration in the Ni nanoparticles decreases the catalytic activity towards methane activation when compared to pure Ni nanoparticles, while improving the overall stability. Thus, it is possible that the size and composition of the Ni-Fe nanoparticles also play a key role in the catalytic performance of the catalyst [24].

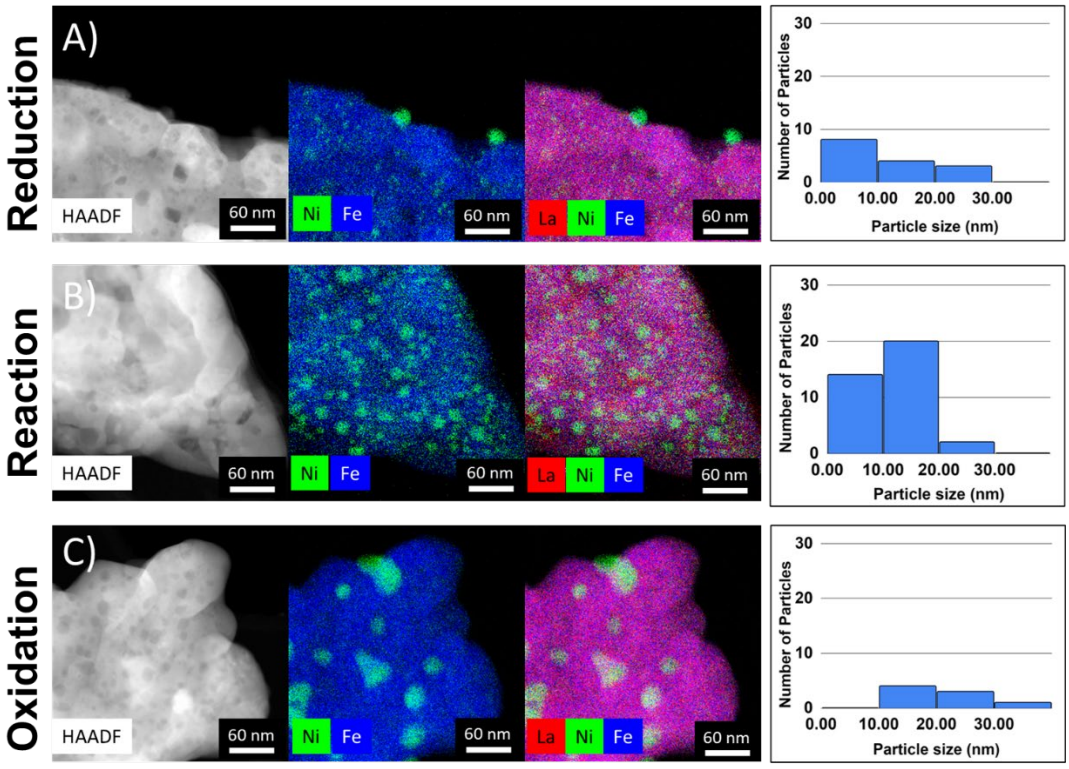

Figure 5.4 STEM of LaFe0.8 Ni0.2O3 perovskite a) reduced in 5%H_2/He for 30 min c) after DRM d) after oxidation in air for 120 min at 700 °C.

Figure 5.4 shows STEM/EDS of LFNO sample reduced at 30 min, reduced 30 min with performed DRM, and reduced 30 min and oxidized at 700 °C for 120 min. After

reduction in a 5%H_2;95%He environment for 30 min nickel has begun to exsolve out of the perovskite material. Average particle size is 12 nm ± 7 nm. After performing DRM on the same material, the average particle size is 12 nm ± 5nm. However, an increase in particle distribution is seen indicating exsolution is continuing during DRM. Regeneration can occur in this metal-perovskite system by performing an oxidation step. We oxidized the reduced material in air at 700 °C for 120 min. An increase in particle size is seen with less particle population. EDS shows the Ni nanoparticles oxidized forming NiO. After 30 min reduction, Ni concentration is 67.1% and Fe is 32.9%. After DRM is performed Ni particle concentration increases to 91.7% and Fe is 8.3% suggesting Fe diffuses back into the perovskite bulk. After oxidation, Ni particle concentration is 98.3% and Fe is 1.7%.

5.3.2 X-ray Absorption Spectroscopy

The magnitude white-line of Ni in the XANES follows as Oxidized ≈ As-Prepared > Post-reaction > Reduced which indicates descending order of the bulk average of oxidation state of Ni. The white-line for as prepared and oxidized states lies between NiO and $LaNiO_3$, with subsequent peaks following the $LaNiO_3$ suggesting that Ni in the perovskite exists in mostly as Ni^{+3} with some Ni^{+2} present as well (Figure 5.5 A). This is in agreement with Steiger et al. [4] who also inferred that Ni exists in $La(NiFe)O_3$ in an octahedral coordination environment similar to Fe with an oxidation state higher than +2. The spectra for Ni after reduction is comparable to that obtained for Ni foil which confirms that nickel has mostly been reduced to Ni^0 state.

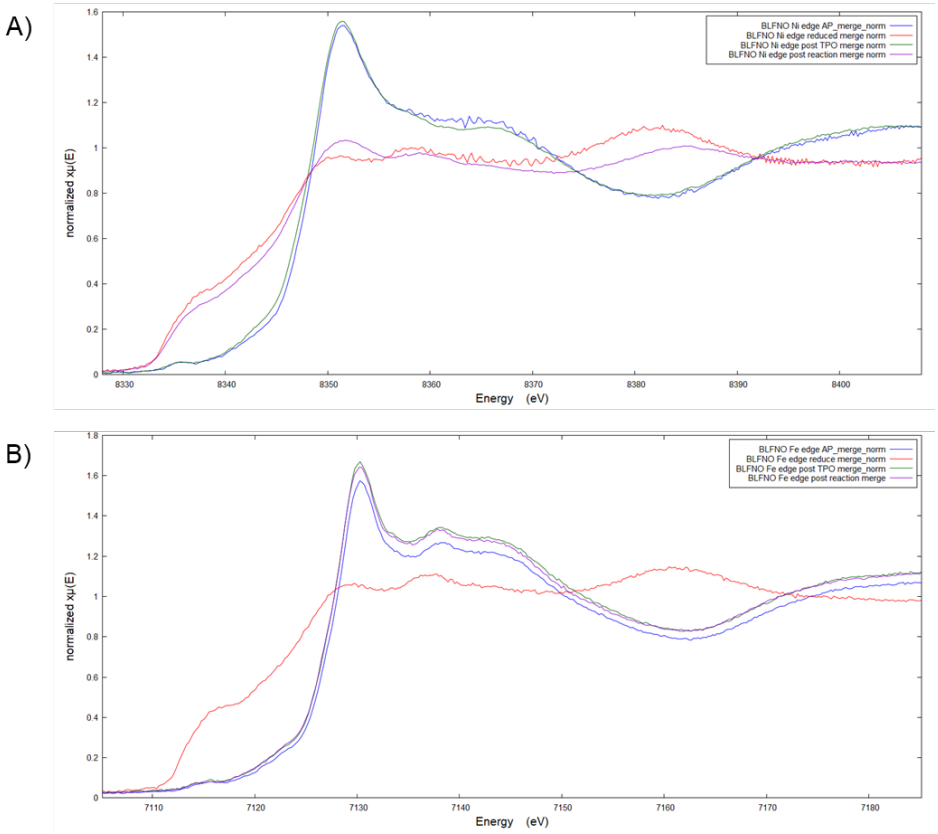

Figure 5.5 A) normalized XANES spectra of BLFNO Ni K-edge as-prepared, reduced, TPO, post reaction B) normalized XANES spectra of BLFNO Fe K-edge as-prepared, reduced, TPO, and post reaction.

The slightly higher white-line for the post-reaction spectra, indicates a small degree of oxidation of the Ni in the environment for methane dry reforming. For Fe, the order follows as Oxidized ≈ post-reaction > As-Prepared > Reduced (Figure 5.5 B). On Fe, our results diverge from Steiger et al. [4] who saw no significant change in Fe K-edge XAS upon reduction, although they only reduced their sample to 600°C. These macroscopic comparisons of Ni and Fe XANES patterns suggest that the bulk of Fe during reaction is in the perovskite phase in a state like the as-prepared or oxidized states while majority of Ni remains in the reduced state during reaction. These observations are consistent with results from the STEM HAADF and EDS images where Fe composition of the

nanoparticles was reduced upon subjecting the sample to reaction conditions, while upon oxidation most of the Fe had reincorporated into the perovskite and to a greater extent than Ni.

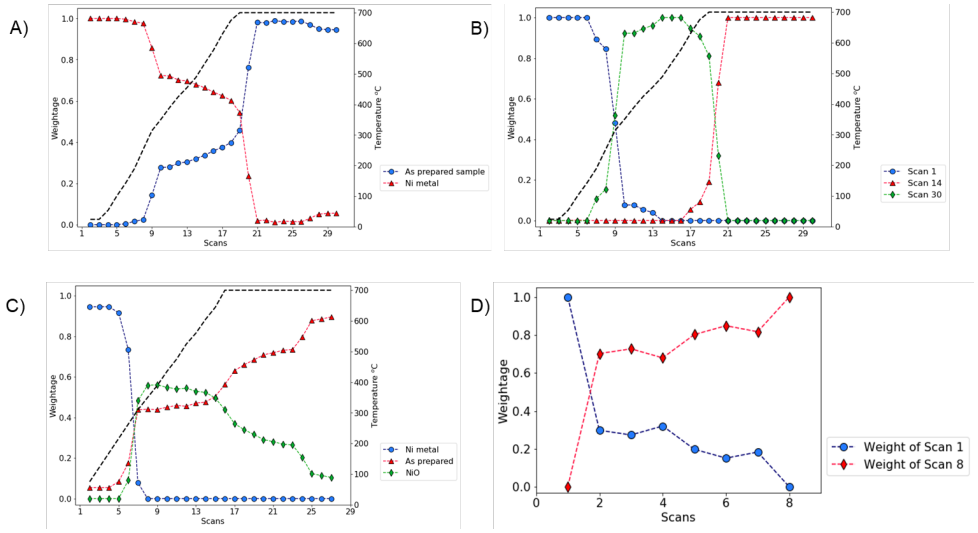

Figure 5.6 LCF of Ni K-edge XANES collected A) during reduction of perovskite sample B) with 1st, 14th and 30th scans as standards C) with Ni metal as-prepared sample D) during DRM reaction of perovskite sample.

Linear combination fitting of XANES spectra allows us to visualize the extent to which the sample has changed during reduction, oxidation, or reaction (Figure 5.6 and 5.7). Two and three component LCFs were carried out using the As-prepared sample along with Fe and Ni foil as well as metal oxides as standards. The weight of the component as seen in the LCF are not an exact measurement of the state in which the metal exists, but it is a reasonable indicator for the distribution of the metals in different oxidation states and phases.

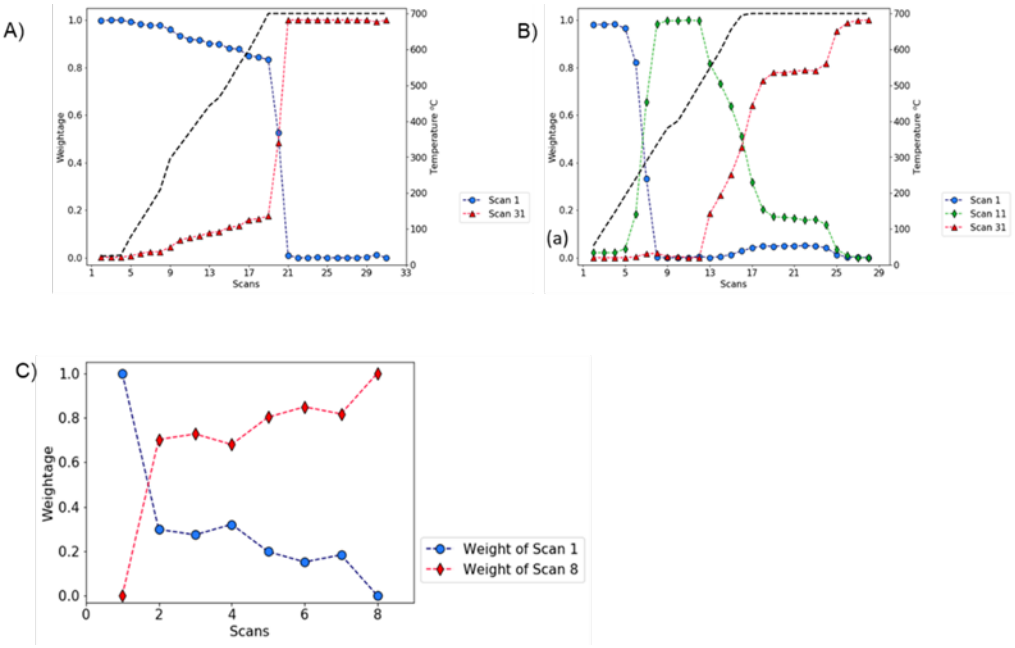

Figure 5.7 LCF of Fe K-edge XANES collected during A) reduction perovskite sample with 1st and 31st scans as components B) oxidation of perovskite samples with 1st and 31st scans as standards C) DRM reaction pr perovskite samples with Ni metal, as prepared samples.

During reduction, Ni reduction proceeds via the formation of an intermediate state around scan 10. The K-edge energy shifts towards a lower energy that is in between the initial state and moving towards the K-edge energy seen in NiO. That is until scan 20 at which point about 95% of the Ni is in the metallic state. For Fe, the reduction begins very slowly around scan 9. Until scan 19 (~610°C). There is little to none of an intermediate state and the Fe is goes from perovskite state to metallic state directly.

During oxidation, around scan 6, all the Ni is oxidized into NiO and perovskite phases. Beyond this point, the NiO gradually transitions into the perovskite phase and about 90% of the Ni is back into the perovskite phase by the end of the oxidation run. The trend visible from the LCFs seem to suggest that the return to the perovskite phase is more sudden with about 75% of Fe in the perovskite state by scan 8 (~270°C) with gradual reentry

continuing thereafter. Fe also goes through an intermediate state that resembles γ-Fe_2O3. Oxidation of Fe occurs faster than that of Ni which is the opposite of what occurs during reduction. That is expected given that nickel is more reducible than iron.

It follows from in-situ XANES during TPR and TPO, that the exsolution of Ni and Fe is reversible as is seen elsewhere. Moreover, given the predisposition of Ni to be reduced, Ni exsolves earlier than Fe during the TPR. As the perovskite-based sample is further subjected to reducing conditions, the exsolution of Fe follows that of Ni and the metallic phase formed changes composition and is gradually enriched in Fe. Furthermore, during oxidation Fe is preferentially oxidized before Ni and almost immediately re-enters the perovskite phase. The oxidation and re-entry of Ni is more gradual, and a significant portion of Ni goes through an intermediate NiO state.

More interestingly, during reaction of dry methane reforming, the Ni remains almost entirely in metallic state but ~90% of Fe almost immediately returns to the perovskite state. Theofanidis et al. [19] suggested that in the redox environment of dry methane reforming, Fe is oxidized partially to FeO_x while Ni retains its metallic state. The authors studied this in Fe-Ni bimetallic catalysts supported over $MgAl_2O_4$. In the case of dynamic supports such as perovskites, our observations with XAS and STEM-HAADF and EDS suggest that the partial oxidation of Fe is concomitant with its reentry in the parent perovskite.

Local coordination of the Ni and Fe in the changing environments were determined by Extended X-ray Absorption Fine Structure. For Ni edge-EXAFS, models were fit with $FeNi_3$ for the reduced and post-reaction samples. The strong overlap of Fe K-edge EXAFS

plots, in the as prepared, oxidized and post-reaction state can be seen both in k^3-weighted $\chi(k)$ as well as $\chi(R)$ plots, all of them resembling $LaFeO_3$ which was chosen as the model. The plots for reduced state Fe K-edge EXAFS stands but it bears a closer resemblance to Ni metal (shifted to overlap with Fe) rather than Fe metal. This suggests that the local coordination around Fe resembles the fcc structure similar to that of Ni metal. Thus, $FeNi_3$ was chosen as the model for fitting the Fe K-edge EXAFS of reduced state sample.

Comparing the Ni K-edge EXAFS plots, the as-prepared and oxidized states are very similar. There is however an additional feature visible around the 2.54Å of the oxidized state EXAFS, which we posit is from Ni-Ni scattering path of NiO, a likely remnant of the transition of Ni from reduced to oxidized state. Thus, upon oxidation, most of the Ni returned to a similar coordination environment that it existed in prior to reduction Comparing these with the standards, the strongest resemblance is with $LaFeO_3$, which was chosen as the model (with one Ni atom replacing one of the Fe atoms). We can also, qualitatively assess that Ni and Fe co-exist in similar coordination environments in the as-prepared and oxidized states based on the similarities of EXAFS profiles. The k3-weighted $\chi(k)$ plot of the post-reaction state appears to be slightly offset from the reduced state. In the R-space, the two plots look similar and the $FeNi_3$ model was chosen for both. Recall, the XANES profile of the post-reaction state had a white-line that was more pronounced than the reduced state. This implies that a small fraction Ni could be in a higher oxidation state during reaction conditions. The $FeNi_3$ model however still offers a reasonable fit to the post-reaction state Ni K-edge EXAFS.

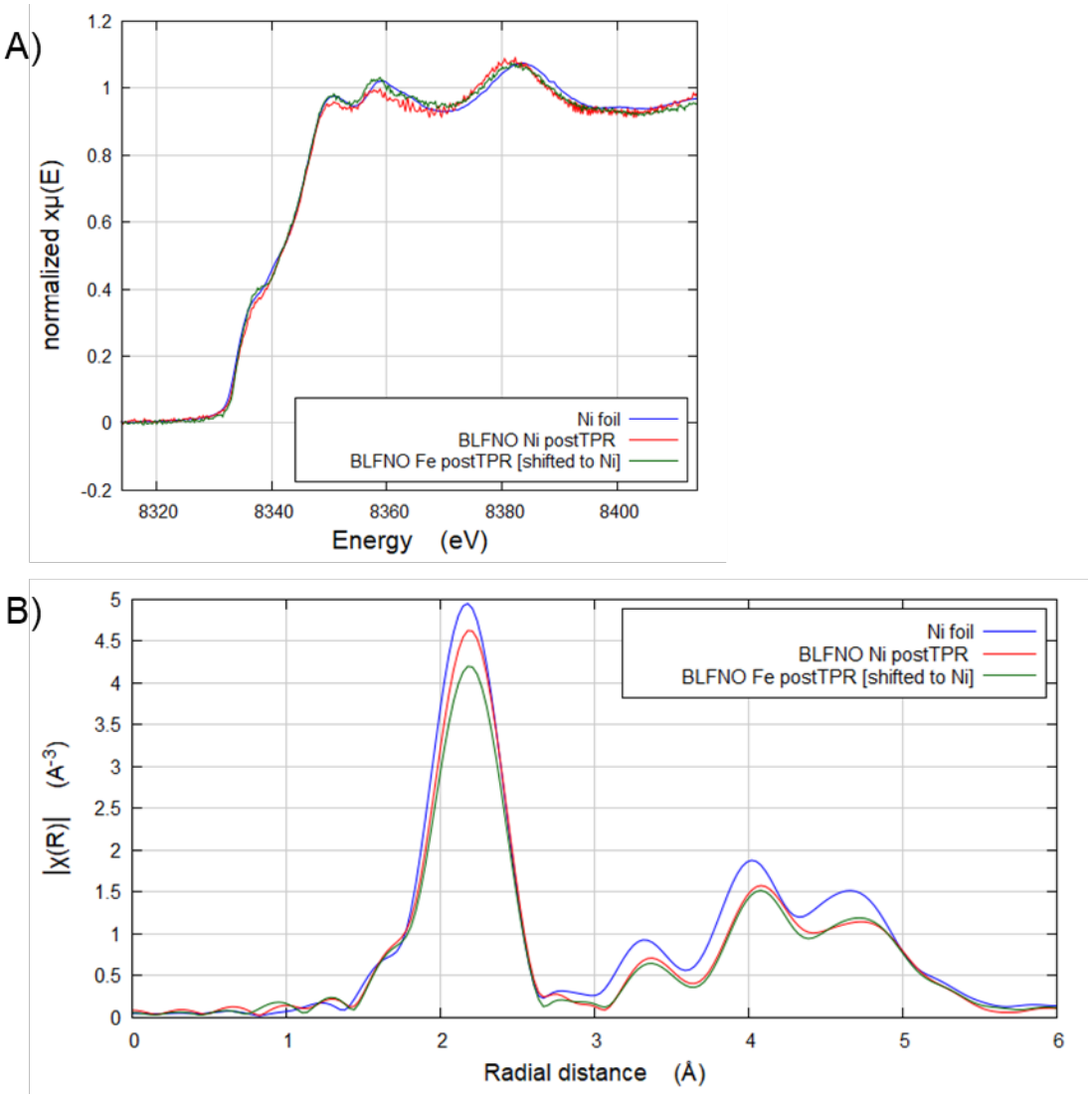

Figure 5.8 A) XANES spectra of Ni foil, Ni post TPR, and BLFNO Fe post TPR B) corresponding Fourier transform plot.

	Scattering path	N	S_0^2	σ^2	ΔE(eV)	ΔR (Å)	R
As prepared, Ni edge, $LaFeO_3$ model χ^2_{red} =211 R-factor = 0.017	O	6	0.81	4.86	0.85 ± 0.98	-0.092	1.95
	La	8		6.48		0.058	3.34
	Ni	6		4.86		0.299	4.28
	O-Ni	12		0.81		-0.096	3.94
Reduced, Ni edge, Ni metal model χ^2_{red} =1256 R-factor = 0.033	Ni	12	0.81	0.0067	-1.62 ±0.75	0.023	2.51
	Ni	6		0.0094		0.033	3.55
	Ni-Ni	48		0.0094		0.035	3.77
	Ni	24		0.0094		0.040	4.35
	Ni-Ni	48		0.0094		0.043	4.69
	Ni-Ni	96		0.0094		0.043	4.69
	Ni	12		0.0094		0.046	5.02
	Ni-Ni	24		0.0094		0.046	5.02
	Ni-Ni-Ni	12		0.0094		0.046	5.02
Oxidized, Ni edge, $LaFeO_3$ model χ^2_{red} =211 R-factor = 0.017	O	6	0.81	4.86	0.85 ± 0.98	-0.092	1.95
	La	8		6.48		0.058	3.34
	Ni	6		4.86		0.299	4.28
	O-Ni	12		0.81		-0.096	3.94
Post reaction, Ni edge, Ni metal model χ^2_{red} =1256 R-factor = 0.033	Ni	12	0.81	0.007	-1.62 ±0.75	-0.013	2.47
	Ni	6		0.009		-0.019	3.50
	Ni-Ni	48		0.009		-0.020	3.71
	Ni	24		0.009		-0.023	4.29
	Ni-Ni	48		0.009		-0.025	4.62
	Ni-Ni	96		0.009		-0.025	4.62
	Ni	12		0.009		-0.027	4.96
	Ni-Ni	24		0.009		-0.027	4.96
	Ni-Ni-Ni	12		0.009		-0.027	4.96

Figure 5.9 Table of fitting parameters obtained by best fitting of Ni-K edge EXAFS plot of as prepared, reduced, oxidized, and post reaction perovskite sample fit to LaFeO3 model.

	Scattering path	N	S_0^2	σ^2	ΔE(eV)	ΔR (Å)	R
As prepared, Fe edge, $LaFeO_3$ model χ^2_{red} =483 R-factor = 0.020	O	6	0.63	0.0014	4.08 ± 0.60	-0.053	1.99
	La	8		0.0109		0.092	3.37
	Fe	6		0.0120		0.067	4.05
Reduced, Ni edge, Ni metal model χ^2_{red} = 425 R-factor = 0.032	Ni	12	0.63	0.0058	-2.71 ± 1.12	0.020	2.51
	Ni	6		0.0126		0.028	3.55
	Ni-Ni	48		0.0126		0.030	3.76
	Ni	24		0.0083		0.034	4.35
	Ni-Ni	48		0.0083		0.037	4.68
	Ni-Ni	96		0.0083		0.037	4.68
	Ni	12		0.0080		0.040	5.02
	Ni-Ni	24		0.0080		0.040	5.02
	Ni	12		0.0080		0.040	5.02
	Ni-Ni-Ni	12		0.0080		0.040	5.02
Oxidized, Fe edge, $LaFeO_3$ model χ^2_{red} = 483 R-factor = 0.02	O	6	0.63	0.0014	4.08 ± 0.60	-0.053	1.99
	La	8		0.0109		0.092	3.37
	Fe	6		0.0120		0.067	4.05
Post-reaction, Fe edge, $LaFeO_3$ model χ^2_{red} = 483 R-factor = 0.02	O	6	0.63	0.0014	4.08 ± 0.60	-0.053	1.99
	La	8		0.0109		0.092	3.37
	Fe	6		0.0120		0.067	4.05

Figure 5.10 Table of fitting parameters obtained by best fitting of Fe-K edge EXAFS plot of as prepared, reduced perovskite sample fit to Ni metal model (with Fe core), oxidized, and post reaction perovskite sample fit to LaFeO3 model.

5.4 Conclusion

In summary the EXAFS sheds light on local coordination environments around Ni and Fe atoms in the perovskite-based catalyst. It confirms our observations from XANES and STEM-HAADF that most of the Fe returns to the perovskite-state in the reaction conditions

of DRM while Ni remains in metallic state. Furthermore, the reversibility of exsolution through redox cycling is also confirmed, while also shedding light on the dynamics of the process. Nickel being more reducible than iron, exsolves to a greater degree and leads to the formation of Ni-rich nanoparticles with a fcc structure. Fe is quick to be oxidized in both oxidizing and DRM environments and returns to the perovskite state. The implication of this for catalysis is that in DRM environments, the redox cycling of Fe stabilizes the metallic Ni which is key for activating C-H bonds. The presence of Fe also suppresses complete decomposition of the perovskite seen in La-Ni based perovskites [4] [25]. This allows the regeneration of the perovskite to happen at lower temperatures.

References

[1] Z. Bian, S. Das, M. H. Wai, P. Hongmanorom and S. Kawi, "A review on bimetallic Ni-based catalysts for CO2 reforming of methane," *ChemPhysChem,* vol. 18, no. 22, pp. 3117-3134, 2017.

[2] C. Liu, J. Ye, J. J. and Y. Pan, "Progresses in the preparation of coke resistant Ni-based catalyst for steam and CO2 reforming of methane," *ChemCatChem,* vol. 3, no. 3, pp. 529-541, 2011.

[3] J. Deng, M. Cai, W. Sun, X. Liao, W. Chu and X. S. Zhao, "Oxidative methane reforming with an intelligent catalyst: Sintering-tolerant supported nickel nanoparticles," *ChemSusChem,* vol. 6, no. 11, pp. 2061-2065, 2013.

[4] P. Steiger, R. Delmelle, D. Foppiano, L. Holzer and A. Heel, "Structural Reversibility and Nickel Particle stability in Lanthanum Iron Nickel Perovskite-Type Catalysts," *ChemSusChem,* vol. 10, no. 11, pp. 2505-2517, 2017.

[5] Y. Nishihata and J. Mizuki, "Self-regeneration of a Pd-perovskite catalyst for automotive emissions control," *Nature,* vol. 418, pp. 164-167, 2002.

[6] H. Tanaka, I. Tan, M. Uenishi, M. Taniguchi, M. Kimura and Y. Nishihata, "LaFePdO3 perovskite automotive catalyst having a self-regenerative function," *Journal of Alloys and Compounds,* Vols. 408-412, pp. 1071-1077, 2006.

[7] A. Cao, R. Lu and G. Veser, "Stabilizing metal nanoparticles for heterogeneous catalysis," *Physical Chemistry Chemical Physics,* vol. 12, pp. 13499-13510, 2010.

[8] D. Neagu, G. Tsekouras, D. N. Miller, H. Ménard and J. T. S. Irvine, "In situ growth of nanoparticles through control of non-stoichiometry," *Nature Chemistry,* vol. 5, pp. 916-923, 2013.

[9] T.-S. Oh, E. K. Rahani, D. Neagu, J. T. S. Irvine, V. B. Shenoy, R. J. Gorte and J. M. Vohs, "Evidence and Model for Strain-Driven Release of Metal Nanocatalysts from Perovskites during Exsolution," *The Journal of Physical Chemistry Letters,* vol. 6, no. 24, pp. 5106-5110, 2015.

[10] S. Shah, M. Xu, X. Pan and K. L. Gilliard-Abdulaziz, "Exsolution of Embedded Ni–Fe–Co Nanoparticles: Implications for Dry Reforming of Methane," *ACS Applied Nano Materials,* vol. 4, no. 8, pp. 8626-8636, 2021.

[11] S. Arora and R. Prasad, "An overview on dry reforming of methane: Strategies to reduce carbonaceous deactivation of catalysts," *RSC Advances,* vol. 6, pp. 108668-108688, 2016.

[12] Z. Wei, J. Sun, Y. Li, A. Datye and Y. Wang, "Bimetallic catalysts for hydrogen generation," *Chemical Society Reviews,* vol. 41, pp. 7994-8008, 2012.

[13] S. M. Kim, "Cooperativity and dynamics increase the performance of NiFe dry reforming catalysts," *Journal of the American Chemical Society,* vol. 139, no. 5, pp. 1937-1949, 2017.

[14] T. Margossian, K. Larmier, S. M. Kim, F. Krumeich, C. Müller and C. Copéret, "Supported Bimetallic NiFe Nanoparticles through Colloid Synthesis for Improved Dry Reforming Performance," *ACS Catalysis,* vol. 7, no. 10, pp. 6942-6948, 2017.

[15] J. Zhang, H. Wang and A. K. Dalai, "Development of stable bimetallic catalysts for carbon dioxide reforming of methane," *Journal of Catalysis,* vol. 249, no. 2, pp. 300-310, 2007.

[16] A. Tsoukalou, Q. Imtiaz, S. M.Kim, P. M. Abdala, S. Yoon and C. R. Müller, "Dry-reforming of methane over bimetallic Ni–M/La2O3 (M = Co, Fe): The effect of the rate of La2O2CO3 formation and phase stability on the catalytic activity and stability," *Journal of Catalysis,* vol. 343, pp. 208-214, 2016.

[17] B. Zhao, B. Yan, S. Yao, Z. Xie, Q. Wu, R. Ran, D. Weng, C. Zhang and J. G.Chen, "LaFe0.9Ni0.1O3 perovskite catalyst with enhanced activity and coke-resistance for dry reforming of ethane," *Journal of Catalysis,* vol. 358, pp. 168-178, 2018.

[18] L. Wang, D. Li, M. Koike, S. Koso, Y. Nakagawa, Y. Xu and K. Tomishige, "Catalytic performance and characterization of Ni-Fe catalysts for the steam reforming of tar from biomass pyrolysis to synthesis gas," *Applied Catalysis A: General,* vol. 392, no. 1-2, pp. 248-255, 2011.

[19] S. A. Theofanidis, V. V. Galvita, H. Poelman and G. B. Marin, "Enhanced Carbon-Resistant Dry Reforming Fe-Ni Catalyst: Role of Fe," *ACS Catalysis,* vol. 5, no. 5, pp. 3028-3039, 2015.

[20] S. A. Theofanidis, V. V. Galvita, M. Sabbe, H. Poelman, C. Detavernier and G. B. Marin, "Controlling the stability of a Fe–Ni reforming catalyst: Structural organization of the active components," *Applied Catalysis B: Environmental,* vol. 209, pp. 405-416, 2017.

[21] D. Marrocchelli, N. H. Perry and S. R. Bishop, "Understanding chemical expansion in perovskite-structured oxides," *Physical Chemistry Chemical Physics,* vol. 17, pp. 10028-10039, 2015.

[22] K. Y. Lai and A. Manthiram, "Evolution of Exsolved Nanoparticles on a Perovskite Oxide Surface during Redox Process," *Chemistry of Materials,* vol. 30, pp. 2838-2847, 2018.

[23] M. A. Asoro, P. Ferreira and D. Kovar, "In situ transmission electron microscopy and scanning transmission electron microscopy studies of sintering of Ag and Pt nanoparticles," *Acta Materialia,* vol. 81, pp. 173-183, 2014.

[24] D. Halliche, R. Bourab, O. Cherifi and M. M. Bettahar, "Carbon dioxide reforming of methane on modified Ni/α-Al2O3 catalysts," *Catalysis Today,* vol. 29, no. 1-4, pp. 373-377, 1996.

[25] M. F. Bekheet, "Steering the Methane Dry Reforming Reactivity of Ni/La2O3 Catalysts by Controlled In Situ Decomposition of Doped La2NiO4 Precursor Structures," *ACS Catalysis,* vol. 11, no. 1, pp. 43-59, 2021.

Chapter 6 Summary, Conclusions and Future Work

6.1 Summary and conclusions

The objective of this study was to understand the synthesis-structure relationships of nanomaterials of three different systems a Ni-carbon nanofibers system, a TiO_2-carbon nanofiber system and a bimetallic perovskite system and 1) identify Ni nanoparticle growth mechanisms in a changing polymer/carbon matrix 2) identify carbonization mechanisms of Ni-carbon nanofibers 3) study the synthesis-structure relationship between of TiO_2-carbon nanofibers and identify how polymer and processing parameters affect the phase transformation of TiO_2 polymorphs for water purification application and 4) perform dynamic studies on Ni and Fe exsolution in perovskite-based materials in redox environments for dry methane reforming.

Results revealed several particle growth mechanisms of nickel metal in a carbon nanofiber matrix. The physical confinement of the nickel metal within the polymer metal limits the metal diffusion and particle growth when compared with a no polymer system. TG-MS characterization revealed that initial nucleation and crystal growth of nickel metal was closely related to the decomposition of the PAN whereby HCN evolves suggesting a metal-polymer interaction via its nitrile group. Doing temperature studies and using the Arrhenius equation allowed for the calculation of the activation energy. It was revealed that two particle growth mechanism are occurring, surface diffusion at low temperature and coalescence at temperatures above 600 °C. Understanding the growth mechanisms of the metal within this polymer matrix can provide insight on how to control particle size for a controlled synthesis for the desired application. The graphitization mechanism in this

system was also determined to be a catalyzed graphitization process using the metal nanoparticles as catalysts. The proposed mechanism are methane species adsorb and dissociate onto the surface of the metal, and diffuses into the nanoparticle until supersaturation ejecting an ordered carbon as early as 600 °C. It is not until 800 °C where we begin to see a graphitized structure.

In the TiO_2-carbon nanofiber system, two polymorphs were observed: anatase and rutile. Temperature studies revealed anatase as the dominant phase at temperature below 600 °C. As temperature increases particles diffuse and grow on the surface of the nanofibers. The morphology of these nanoparticles is dependent on the atmospheric environment that they are heat treated in. In addition, different ratios of anatase: rutile were identified in different processing conditions. Polymer effects were also studied where PVP and PAN mixtures were annealed. This was identified that there was an inhibition of rutile phase transformation when a 1:1 PVP:PAN ratio was present due to the disruption of the crystalline structure of the polymer. The PVP;PAN mixture slows down the diffusion of TiO_2 species due to the steric hindrance preventing the growth of anatase and thus phase transformation of anatase to rutile. This study revealed how processing parameters affects the crystal growth and phase transformation of TiO_2 in a carbon nanofiber matrix. The insights obtained in this study can help in controlling the phase ratio of this system to fabricated efficient target-selective materials for photodegradation applications.

In the Ni-Fe perovskite system, our studies revealed coordination environments during reducing, and oxidation treatment. It was shown that nickel metal reduces at lower temperatures than Fe which influences the H_2/CO ratio. This faster reduction of the nickel

metal allows for the exsolution, nucleation and growth of nanoparticles on the surface of the perovskite. The presence of Fe not only reduces coke formation, but also stabilizes the perovskite. In chapter 2, the mechanism of Ni particle growth within a carbon matrix was identified as surface diffusion at lower temperature and particle coalescence at temperatures above 600 °C. In the bimetallic system of Ni-Fe nanoparticles, there was no visual evidence of particle coalescence. Due to a strong interaction between the Ni-Fe nanoparticles with the perovskite support, makes the nanoparticles less mobile and thus slow down and impede coalescence and allows for another mechanism to dominate like Ostwald ripening.

Ultimately this work presents an encompassing study of the synthesis-structure relationships of three different nanostructured system. These studies revealed synthesis strategies that control crystal size, particle size, and phase transformation of nanoparticles and provide insight on how to better fabricate nanomaterials for desired applications of gas-sensing, water purification and dry-methane reforming.

6.2 Future Work

Based on the results presented in this work, the next step would be to take the temperature studied samples and perform performance studies. In the TiO_2-carbon nanofiber system, photodegradation studies need to be performed and identify the ideal anatase: rutile phase ratio for photodegradation of organic pollutants. Band gap measurements should also be identified to see the effect carbon has on TiO_2 nanoparticles if any.

In the Nickel-carbon nanofiber system, post oxidation can be performed to make NiO-carbon nanofibers for gas-sensing applications. Performance should be studied and particle size effects on gas sensing efficiency should be identified. Different graphitic content should be synthesized to identify the optimized graphitic content for gas sensing applications without reducing overall performance.

Different studies can still be performed in the Ni-Fe bimetallic perovskite system for dry methane reforming. Particle size studies can be more deeply studied to observe the effects it has on dry methane reforming.